FREE UNIVERSITY BERLIN

MASTER OF SCIENCE (M.Sc.)

Magnetotelluric Investigation of Stratovolcanoes in the Central Andes

Author: Maximilian Buchner

Fachbereich Geowissenschaften

Institut für Geologische Wissenschaften

Fachrichtung Geophysik

February 2017

Supervisors:

Prof. Dr. Serge Shapiro

Freie Universität Berlin, Malteserstr. 74-100

12249 Berlin

Prof. Dr. Georg Kaufmann

Freie Universität Berlin, Malteserstr. 74-100

12249 Berlin

Abstract

The Andes are the longest continental mountain belt in the world. Subduction of the oceanic Nazca Plate beneath the continental South American Plate is the reason of volcanic activity in the region of the Central Andes. Since more than two decades the magnetotellurics group at Free University of Berlin has worked in the volcanic arc, fore- and backarc of the Central Andes. This thesis aimed at re-evaluation of MT data with a 3-D inversion scheme which recently became available.

Two campaigns were carried out in the 2000's to gather long-period and audio magnetotelluric data in the Central Volcanic Zone at 18°S in Chile and Bolivia. A profile line with a total length of 340 km extends from the Coastal Cordillera in northernmost Chile, along the volcanic arc and Altiplano high plateau and ends in the Eastern Cordillera in Bolivia. Additional measurements - including higher frequencies - were conducted in a circular shape around two volcanoes (Taapaca and Parinacota) to gain information about their structure. Geochemical studies assumed a magma chamber at shallow depths for both volcanoes.

Previous 2-D inversions revealed a well conductive feature at upper mantle depths in the asthenospheric wedge, but laterally offset from the volcanic arc by almost 100 km. Nevertheless, the data indicated strong 3-D effects along the transect and a good conductor, such as a magma chamber, beneath the volcanoes.

Recent progress in computer power, numerical algorithms and inversion programs allows inversion of complex data with 3-D effects in acceptable time. The main goal of this study was the 3-D inversion of the transect with its good conductor in the mantle. Furthermore, a 3-D study was carried out on both volcanoes.

In this thesis, the new 3-D models confirm the deep conductor in the Altiplano. For the first time, the existence of a well-conducting, magmatic layer beneath volcanoes is resolved in a 3-D inversion study.

Contents

Chapter 1

Introduction

Magnetotellurics (MT) is an electromagnetic geophysical method developed and introduced by Andrey Tikhonov and Louis Cagniard in the 1950's. Due to constant development and improvement in computer science, instruments, and modeling the MT method has become a valuable discipline of geophysics. Its ability to display conductive and resistive features in the underground, even in depths up to 500 km made it a perfect practice beside other geophysical methods. In addition to seismology information about the earth's crust and upper mantle can be derived by MT measurements. The use of the natural magnetic field fluctuation makes this method unique. The measurement of variations of the natural electric and magnetic fields in orthogonal directions can be easily performed on Earth's surface. However the data quality suffers from disturbances like in city areas or regions close to the equator or very high latitudes.

South America with its trench parallel geological features is a perfect target for geophysical campaigns. In the 2000's a transect of MT sites was conducted in two survey campaigns in the Bolivian Orocline, also known as Arica-Band after the city Arica. These long-period magnetotelluric (LMT) measurements should bring insight into the geological features of the Central Volcanic Zone. The main goal was to display the electrical distribution in the underground on the transect and a further approach was done on two stratovolcanoes in the Central Andes at 18°S.

In general, the profile showed a predominant 2-D distribution which was already discovered in previous work. The remaining questionable 3-D effect and topography problems were the main target of the research. For the reinterpretation of the data the software ModEM by Egbert and Kelbert (2012) was used.

The thesis starts with a short overview of the tectonic setting and the geological development of South America. The subduction zone will be treated in a separate chapter here as it had influence on the whole transect. In chapter 3, the theoretical concepts and physics behind the magnetotelluric method is enlightened. In the following chapter

4, the concept of geophysical forward and inverse modeling is briefly illustrated.
The following two chapter investigate the transect in the Bolivian Orocline and the two
volcanoes Taapaca and Parinacota in the Central Andes. Based on previous 2-D studies
and geochemical reveals, a new 3-D reinterpretation is done. Hydrothermal systems are
located above upper magma chambers of volcanoes and should be resolved by the MT
method, as well as the the lower magma reservoir system in the MASH Zone. A typical
constitution of a magmatic system is illustrated in Figure 1.1. Concluding remarks on
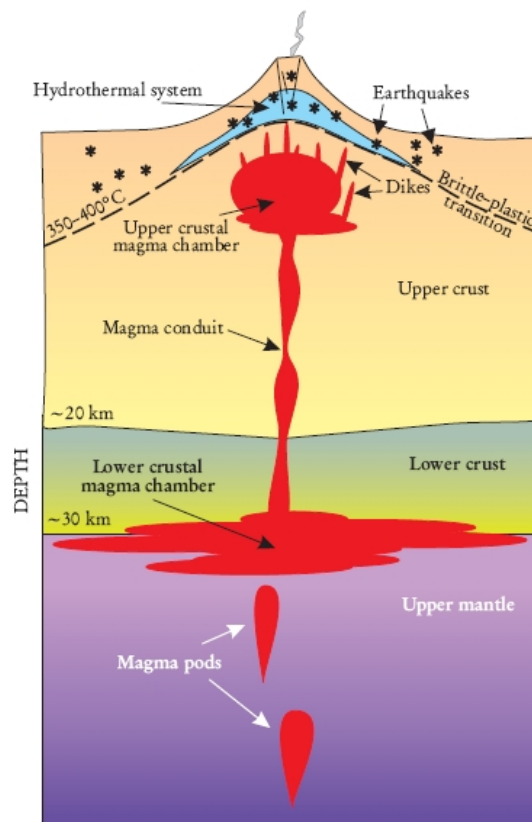every study will be added in the end of every chapter.

FIGURE 1.1: **Conceptional model of a volcano.** Hydrothermal system in the cone
above a upper crustal magma chamber that is fed by a magma conduit from a lower
crustal magma chamber between the lower crust and the upper mantle. In the Central
Andes the MASH zone lies at 70 km depth. Image taken from Hill (2002).

Chapter 2

Geology

2.1 Geological setting in the Central Andes

This chapter introduces the geological and tectonic setting of South American Continental margin and emphasizes main features of the western coast. Along more than $50°$ latitude the Nazca plate, with an average density of 2.8 - 2.9 $\frac{g}{cm^3}$ (Werner Zeil, 1986) subducts beneath the continental South American plate. The subduction angle is usually around $25°$ to $30°$ (Klotz et al., 2006) and the plate moves with an average speed of 6.5 $\frac{cm}{yr}$. It is known as one of worlds largest non interrupted subduction zones in the world. The Nazca Plate expands from different ridges: the Chile Rise in the south which is next to the antarctic plate and in the north it originates from the Galapagos Ridge or also known Carnegie Ridge where the Nazca Plate interacts with the Cocos Plate and the East Pacific Ridge in the east (Bahlburg et al., 1988). The subduction process has formed a more than 7,500 km long Orogen from the Caribbean coast to Cape Horn with trench-parallel changes of the subduction conditions. The whole subduction system seems to be of a coherent entity, however volcanically active and inactive zones alternate along the coast. Thus the South American Coast is divided into four volcanic active regions, the North-, Central-, South- and Austral-Volcanic Zone (NVZ, CVZ, SVZ and AVZ). In volcanically inactive regions the oceanic plate flattens in about 100 km (Cahill et al., 1992) depth and subducts in the so-called Flat Subduction process horizontal with a maximum length of 300 km (Gutscher et al., 2000). Figure 2.1 illustrates the described setting of the Central Andes, where the colours are an indicator of the plates age.
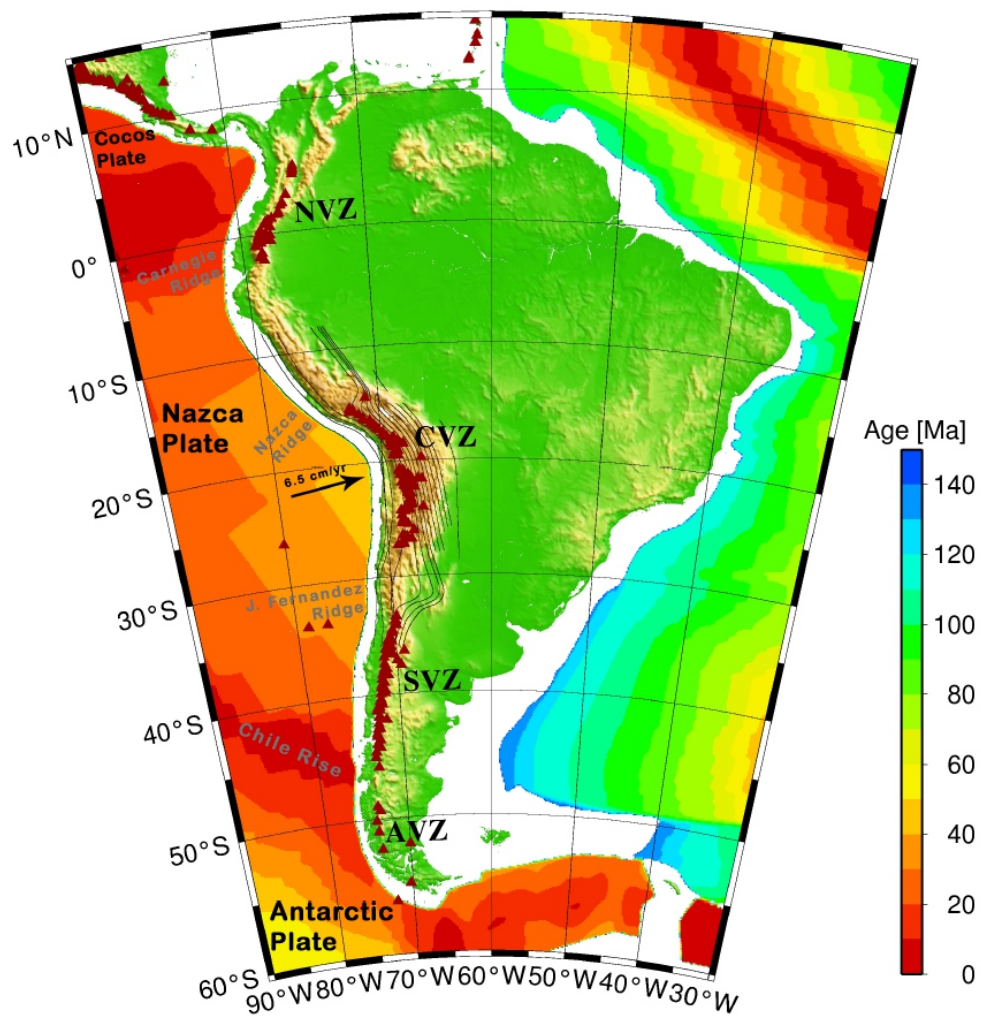
FIGURE 2.1: **Topographic map as described in the text. Coulours display the age of the plates after Müller et al. (1997).** Average subduction movement rate of 6.5 $\frac{cm}{yr}$. Red triangles indicate recent active volcanoes. Lines contour the Wadati-Benioff-Zone around the Altiplano-Puna-Complex after Cahill and Isacks (1992). Image taken from Brasse in pers. com.

2.1.1 Brief glimpse into the geologic setting of the CVZ

The study is located around 19° to 17°S. The area is mainly categorized into three areas like any other classic subduction zone into forearc, volcanic arc and backarc; each of them divided into sections by their geological feature and history. The forearc is described as the magmatic front between the subduction zone and the volcanic chain with its sections Coastal Cordillera (CC), Longitudinal Valley (LV) and Precordillera (PC). It is characterized by E-W running faults. This area is followed by the Altiplano-Plateau separated into the geological units Western Cordillera Escarpment (WCE), Western Cordillera (WC) and the Altiplano (Figure 2.2). The Wadati-Benioff-Zone is indicated with dotted lines, using 25 km steps. Two volcanoes of the Central Andes are drawn on the map as they are a substantial part of this study.
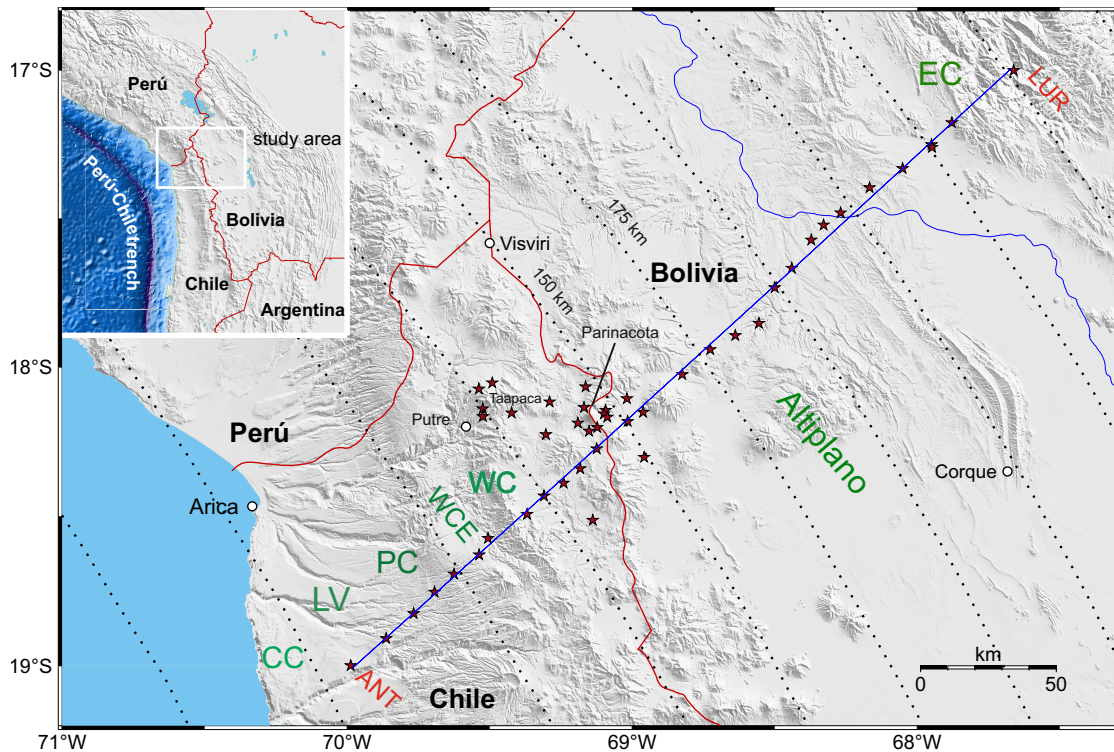

FIGURE 2.2: **Area of investigation.** Inlet top left: study area with Peru-Chile-Trench in South America. Image shows the location of the measured stations in the CVZ. Red stars indicate stations. Beginning with ANT to LUR. In the center of profile line are more stars located around stratovolcanoes. Geological Features from coast to Bolivia are Coastal Cordillera (CC), Longitudinal Valley (LV), Pre-Cordillera (PC), Western Cordillera Escarpment (WCE), Western Cordillera (WC) and the Altiplano. Station LUR is already located in the Eastern Cordillera.

In central Bolivia the Eastern Cordillera reaches almost 7,000 m height (Bahlburg et al., 1988), due to relatively young vertical movements in the crust (Werner Zeil, 1986) that caused this height differences in a very short range. In front of the forearc runs the Peru-Chile trench or Atacama trench with a maximum depth of 8,066 meters as a result

of the subduction zone and the lack of sediment supply from the continent. Since at least 12 Ma this area is highly arid with low rainfall of less than 50 mm / year, unable to provide sufficient material from the mainland. The coastal and trenchline are bended the same way in the CVZ and moreover the oceanic and continental topography have the same symmetry (Gephart et al., 1994). The crustal thickness is estimated with about 75 km by seismic measurements by Yuan (Yuan et al., 2000). New seismic studies indicate a thickening of the crust westward (Ryan et al., 2011).
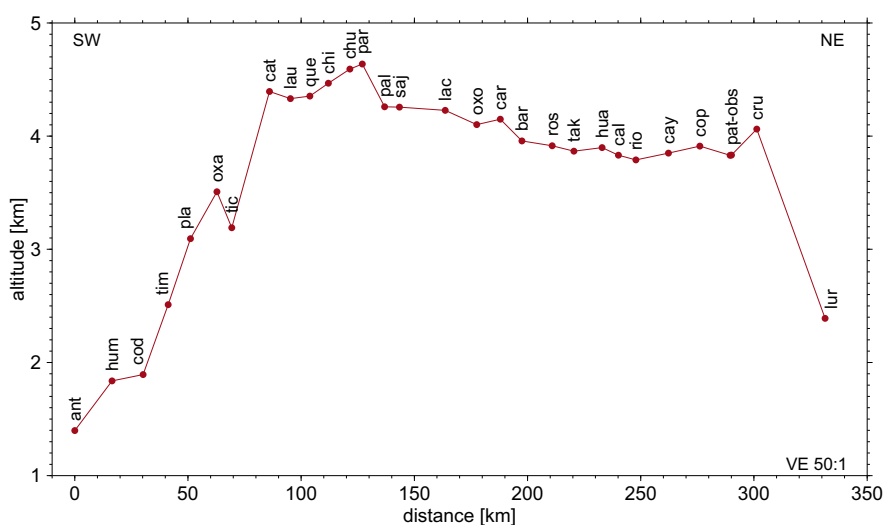

FIGURE 2.3: **Altitude profile along profile line with stations from ANT to LUR.** Around 100 km distance from ANT to CAT make 4,000 m height difference. CAT is located in the Western Cordillera. Most of the stations are located in the Western Cordillera and Altiplano with changes of altitude at a maximum of 1,000 m. LUR in the North East is located in the Eastern Cordillera as part of the backarc at a height of 2,300 m.

2.1.2 Tectonic and geological development

The **Coastal Cordillera** is located in the west of the Andes as the slope part. It is developed by young tectonic movement that is located between the Pacific in the west and the Longitudinal Valley in the East. Its cliff coasts range up to 1,200 m with an average altitude of 1,000 m. Precambrian series as a part of it consists of gneiss and granulites with a basement of about 2,000 Ma old intermediate and alkaline material. Tholeitic basalts (La Negra Formation) and batholiths (in ten km depth) dominate here as they have developed in the upper Paleozoic (305 Ma ago), very likely in the Jurassic (200 Ma) and Early Cretaceous (90 Ma). This is an indicator that the magmatic arc was located here at this time (Scheuber et al., 1994) and shifted eastwards over the time. The overlaying rocks of the Coastal Cordillera are divided into chess patterned parts
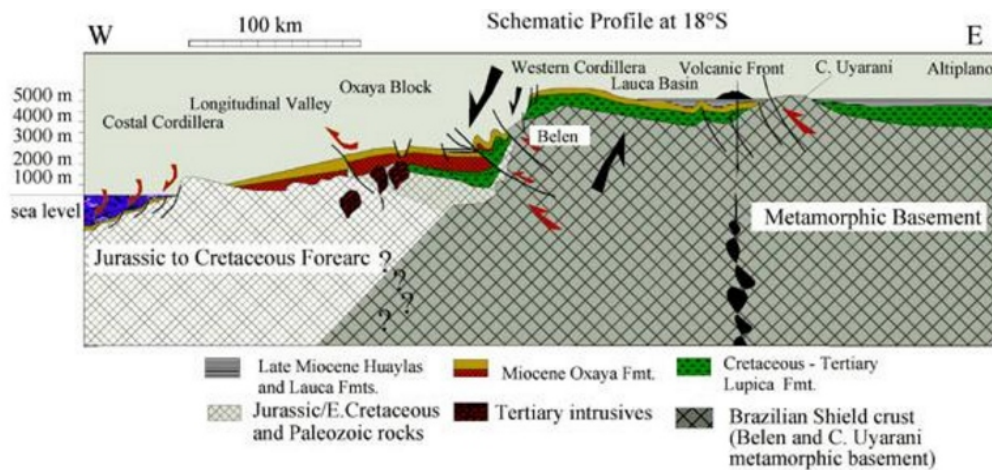
FIGURE 2.4: **Schematic east-west profile slightly modified after Wörner et al. (2000), from the coast to the Altiplano (at about** 18°**).** Jurassic/Early Cretaceous and Palepzoic rocks in the CC, Longitudinal Valley overlain by Miocene Oxaya Formation, Volcanic Front has tertiary intrusives piercing through the metamorphic basement and Cretaceous-Tertrary Lucica Formation. The Altiplano is permeated by the Late Miocene Huayalas and Lauca Formations.

due to drainage and cracks (Allmendinger et al., 2005). The Atacama Desert is about 500 km long with coast parallel running faults.

The **Longitudinal Valley** is also known as the Pampa del Tamarugal and located between 23° to 18°S with a maximum width of 70 km. Between latitude 33° to 27°S it disappears as Precordillera and Coastal Cordillera are directly set to each other. In the Cretaceous (110 Ma), the valley was probably part of the volcanic front. Now it consists of a 2,000 m thick sequence of andesitic lava covered by clastic sediments as the forearc depression of the subduction system. After Scheuber et al. (1994) it was formed offshore by volcanic alterations in the Oligocene (25 Ma) and Miocene (15 Ma).

The eastern part of the Chilean Longitudinal Valley migrates to the **Precordillera** at Sierra de Domeyko which raises to heights of about 4,000 meters. Due to a long lasting constant volcanism around 75-35 Ma ago this area was shortened (Scheuber et al., 1994) and resulted in trench-parallel faults. Famous active fault systems are the Precordillera-Fault System at 19° to 21°S or the West-Fissure 20° to 23°S. The Preandean Depression clearly seperates from the Western Cordillera as there are Paleozoic (250 Ma) sediments and plutonic rocks of different ages overlain by Late Carboniferous (300 Ma) to Triassic (200 Ma) volcanics and sediments. The northern part of the Precordillera includes intrusions (Damm et al., 1986) with an age of 43.7 $\pm$ 3.8 Ma. The volcanic activity possibly ended 35 Ma ago (Wörner et al., 2000) but became active again in the Inner-Arc Region in Bolivia at the Early or Middle Eocene. A possible explanation could be a new subduction process of the Nazca plate after a long time flat subduction (James et al., 1999).

The **Western Cordillera** has been deformed during the Miocene to Holocene by arc-normal shortening. Underlying rocks from the Paleozoic to Oligocene are covered by lava and ignimbrite layers of the Miocene to Holocene arc system and are exposed from the Altiplano to Precordillera (Scheuber et al., 1994). These part of the volcanic arc reaches an average altitude of 4,000 m above the sea level and stratovolcanoes with peaks up to 7,000 km, such as Sajama with 6,542 m height as Bolivias highest volcano, which developed in the Plio-Pleistocene (four Ma) (Wörner et al., 2000). The middle section or Central Cordillera is characterized by the intrusion of Mesozoic rocks into a Precambrian basement and Cenozoic volcanic activity (Moores et al., 1995).

At 16° to 25°S, the **Altiplano-Puna** high-plateau is set with a length of about 2,000 km and a width of 400 km between southern Peru and northern Argentina. It runs through Chile and Bolivia as the highest plateau in the world formed in the absence of continental collision with average elevations of 3,500 m in its northern part as Altiplano. The southern part is named Puna (Isaacks et al., 1988). The formation of the Altiplano-Puna plateau was caused by crustal thickening as a result of the horizontal shortening of a thermally softened lithosphere in the late Oligocene (Allmendinger et al., 1997). The area is dominated by sedimentary basins and salt flats, like the Salar de Uyuni in Bolivia. It is the largest salt flat on Earth exhibiting less than 1 m of vertical relief over an area of 9,000 km^2 (Borsa et al., 2008). The sedimentary basins are filled with Late Oligocen and recent silicic volcano material covered by Late Miocene/Pleocene ignimbrite layers (Allmendinger et al., 1997). The Altiplano-Puna Volcanic Complex (APVC) between 21° to 24°S covers an area of 50,000 km^2 between the Atacama basin and the Altiplano (de Silva, 1989).

The southern Bolivian backarc of the Central Andes is composed (from west to east) of the **Altiplano**, the **Eastern Cordillera**, the **Subandean Belts**, and the **Chaco** foreland basin. The Eastern Cordillera forms with a maximum height of 6,500 m the eastern border of the Late Oligocene to Late Miocene volcanic arc of the Altiplano. It is mainly developed by Precambrian to Ordovician basement (Kley, 1996). The Subandean Belt forms a classical, east-vergent foreland fold-thrust belt, which grades eastward in the active retoarc foreland basin. This deformation merges into the the Chaco lowland, a semi-arid low altitude area (Dunn et al., 1995).

2.2   Impact of the flat subduction

The development of the Bolivian Orocline volcanic activity is mainly dominated by the effects of the flat subduction process in the Central Andes. The Altiplano of northern Chile and Peru forms one of the world's greatest plateaus (Isaacks et al., 1988). An average elevation of four km in an area of approximately 400 km width and 2,000 km length was probably created by the long-term process of flat subduction. The Nazca Plate subducts beneath western South America with a low angle and there are theories that Andean topography is a result of uplift due to thermal thinning of the lithosphere (Isaacks et al., 1988). In Figure 2.5 the tectonic plate subduction development of a flat subduction process is illustrated (James et al., 1999).

The first frame shows the normal subduction about 50 Ma ago, which was the beginning of the flat subduction process in the Central Volcanic Zone according to geochronological data (Tosdal et al., 1981), (Clark et al., 1990). Constant broadening of the subduction zone along the arc into northern Chile has ended the volcanism in the Central Andes about 38 Ma ago (Hammerschmidt et al., 1992). This indicated a change from normal to flat subduction which happened at least 35 Ma ago. In the Miocene about 25-15 Ma ago the subduction process returned back to normal subduction with a renewed volcanism (Kennan et al., 1995). The slab flattening and slab rollback was apparently initiated in southern Peru and migrated S-S-W. In the first frame of Figure 2.5 the slab subducts at a normal angle beneath northern Chile and Bolivia at 50 Ma. This condition apparently represents a phase which is currently on-going in the Central Volcanic Zone, too. It consists of main-arc magmatism, young minor back-arc deformation and normal subduction (James et al., 1999).

The second frame shows the typical slab rotation of the normal subduction to the flat subduction which took probably place about 45 - 35 Ma ago. It is similar to the Incaic deformation that strongly affected the eastern Altiplano and Eastern Cordillera which
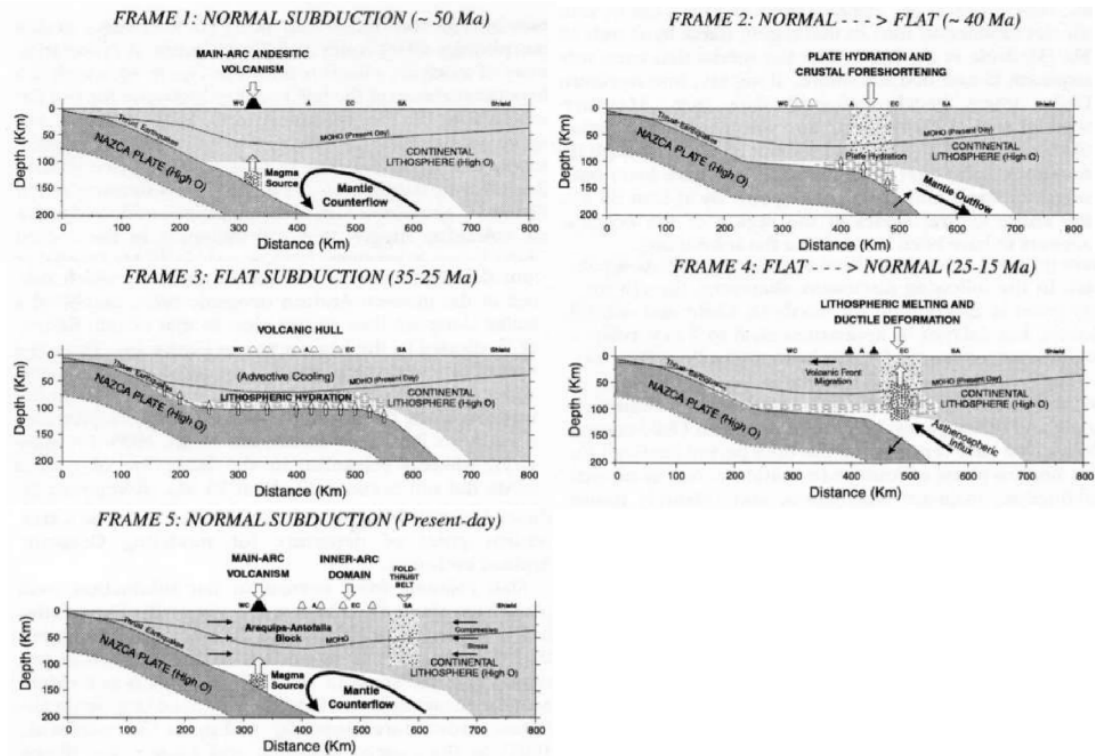
FIGURE 2.5: **Schematic sequence of a cross section in the Central Volcanic Zone illustrates the model for the formation of the Central Andes from 50 Ma to present after James et al. (1999)** The regional units Western Cordillera (WC), Altiplano (A), Eastern Cordillera (EC), sub-Andean zone (SA) are labeled. Moho and and the shield added for reference.

resulted in a crustal foreshortening, thickening and uplift (Sandeman et al., 1995). This might be caused by the Zongo-San Gabán tectonic event at around 40 Ma in northern Bolivia as the collision of the flat slab with the Brazilian shield occured. However, more recent studies studies explained the Incaic tectonic events in the eastern Altiplano and Eastern Cordillera as a result of hydration and weakening of continental lithosphere during the late stages of the transition to flat subduction (Snoke et al., 1997). In the Oligocene (Frame 3) was a time of the volcanic null. The flat subduction caused a general absence of intense deformation, as the overlying continental lithosphere was hydrated by dewatering of the flat slab and cooled through advection. In the inner arc an extensive hydration is assumed which caused a breakdown of amphiboles. This released water from the slab. The heat flow was possibly only about 25 mWm^{-2} (Isaacks et al., 1988). After this period in Frame 4 a normal subduction in the early Miocene occured. A major thermal shock as a sheet of hot astenospheric mantle flowed into the expanding mantle wedge and got into contact with the hydrated mantle of the inner arc in the eastern Altiplano and Easter Cordillera. It created a lot of alkalic mafic to felsic volcanic products (Kennan et al., 1995). Through this event, it thinned and weakened

the mechanic of the lithosphere along the inner arc and resulted in ductile deformation, uplift and collapse to the formation of the Bolivian Orocline. As a result of the hot asthenospheric material flowing into the mantle wedge the volcanic zone broadened. The ultimate result was the forming of the volcanic front along the main active volcanic arc (James et al., 1999). Frame 5 illustrates the present-day Andes. The main volcanic arc is defined by andesitic volcanism.

Model calculation of the current temperatures in the forearc suggest low shear stresses in the order of 15 MPa along the plate contact. The angle of the subduction mainly influences the surface heat-flow density. Additionally, the crustal radiogenic heat-production rate has a major influence on the surface heat-flow. Its influence on crustal temperature remains unimportant. Temperatures at the maximum depth of the seismic coupling between the oceanic Nazca plate and the overriding South American continental plate are in the order of 250 to 300° C, whereas at the maximum depth it reaches an order of 300 to 350° C. at shallow depths (approx. 70 km), the lithospheric temperature structure in the active magmatic arc region is strongly sensitive to temperature changes caused by an assumed asthenospheric mantle wedge (Springer, 1997). The thermally thinned lithosphere results in a surface heat-flow density on the order of 60 to 70 mWm^{-2}. On the plateau the heat flow is widely enhanced in the order of 100 - 120 mWm^{-2} (Springer, 1998).

Chapter 3

Magnetotellurics

3.1 Basic theoretical idea of magnetotellurics

In the 1950's the idea of the technique magnetotellurics (short MT) was introduced by the French geophysicist Louis Cagniard and the Russian geophysicist Andrey Nikolayevich Tikhonov. Advances in computer science, numerical approaches, instruments, the invention of remote referencing and 3D data acquisition (just to name a few) have made MT a valuable and important tool in the research of earth's interior. As a passive geophysical method, MT uses the natural variations of the electric and the magnetic field that get induced in the earth's magnetosphere and ionosphere by solar wind and the magnetic field (Constable et al., 2007). This chapter introduces the method MT and its physics. It is based on the lecture notes of Brasse (2011) and Ritter (2016), as well as the books of Simpson and Bahr (2005) and Vozoff (1987).

3.2 Resistivity or its reciprocal conductivity

The resistivity [Ωm] or its reciprocal conductivity [S / m] is a material property that quantifies how strongly a given material opposes or supports the flow of electric current. Most rock and mineral properties vary by temperature and pressure in the Earth's interior. In the deeper mantle they start melting and are able to carry more electrons which leads to a better conduction of the material. The dependence on temperature and salinity is reduced by fluids in the pore space (Schön, 1997). In Figure 3.1 the conductivity of certain different typical materials is displayed.
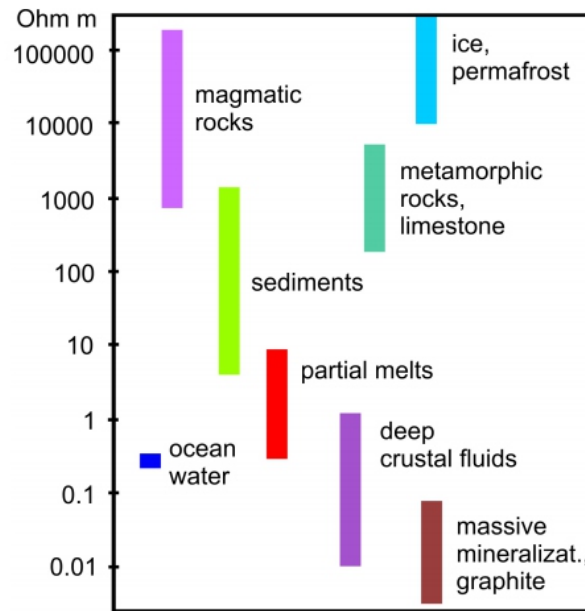
FIGURE 3.1: **Typical resistivity of some rocks and minerals.** Resistivity of freshwater at around 10-100 Ωm while dry ice has over 10^6 Ωm. This study mainly deals with the conductivity of partial melts, ocean water and magmatic rocks. Image taken from Brasse (2011).

3.2.1 Origin and spectrum of MT signals

The magnetic field of the earth is generated in the liquid outer core with its fluid flow being influenced by the earths rotation and the geometry of the inner core. Through secular variations of the fluid flows, the magnetic field propagates through the electrically insulating mantle and crust. The ionosphere of the Earth is located straight above the Earth's atmosphere and very conductive. This supports the Solar quiet or Sq-Current as a result of the dayside solar heating (L-current on the nightside).

Magnetotellurics mainly works with two signal types. The electrical discharge such as lightning spreads laterally into the cavity in the Schumann resonances (see Figure 3.1) and generates electromagnetic impulses with high frequencies between 1 kHz and 30 Hertz (Hz). The energy travels around the earth in a wave guide between the Earth's surface and the ionosphere and its energy penetrates into the Earth (Constable et al., 2004). On the outside of the solid Earth the solar winds interact by deformation and modulation of the magnetosphere. The incoming plasma cloud interacts with the earth's magnetic field and produces low-frequency signals with less than one second. The solar wind doesn't penetrate the Earth's dipolar magnetic field in this process, except in polar

regions, but it slows down and deflects around it (Baumjohann and Nakamura, 2007). The Electrojet is not relevant in this study as the frequencies worked with are too short.
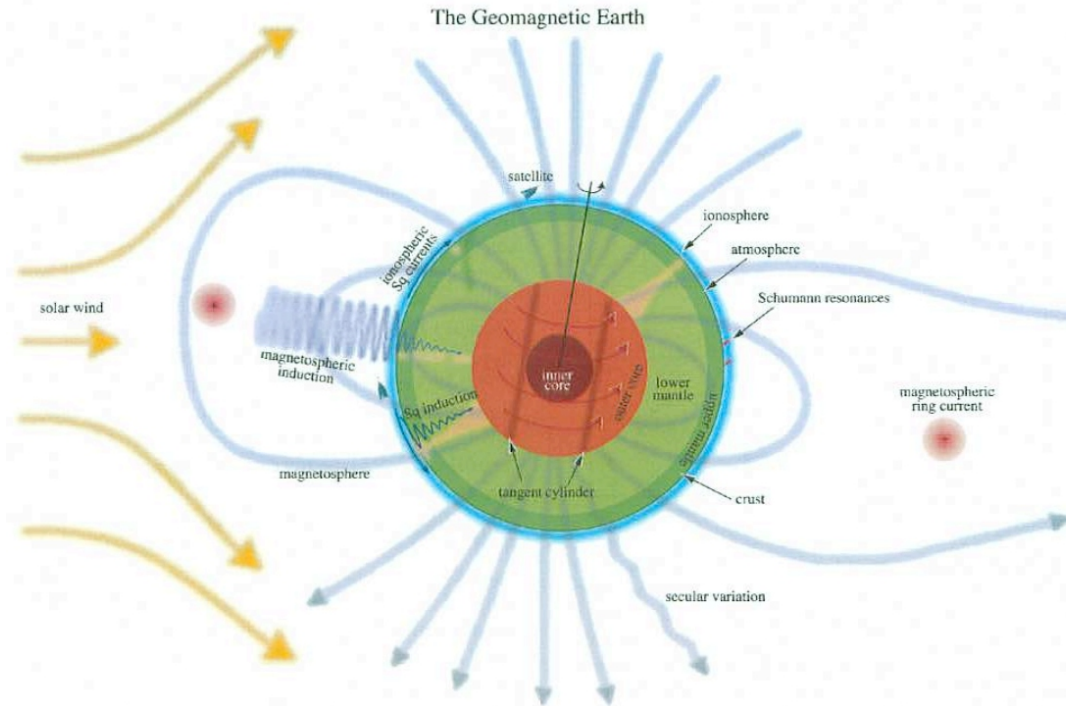
FIGURE 3.2: **Earth's geomagnetic field.** Magnetic field is generated by the liquid outer core. It propagates upward through the relatively electrically mantle and crust. Above atmosphere is the electrically conductive ionosphere located. Lightnings generate high frequencies in the Schumann resonances, in the Earth/ionosphere cavity. The magnetosphere on the outside of the solid Earth is the manifestation of the core dynamo where it gets deformed and modulated by the solar wind. It compresses on the sunside and elongates on the nightside. Image by Constable and Constable (2004).

While the Earth's magnetic field approximately has a spectrum of 10^{-4} to several 1,000 Hz the magnetotelluric systems generally only work with frequency ranges from 10^{-3} to 10^5 seconds (s). Usually MT field measurements get divided into AMT (Audio-MT) for short-period data and LMT (Long-period MT) below 1 Hz. A special role has the so-called dead band at 1 s (see Figure 3.2), as a lack of energy the MT responses become often unreliable which could lead to poor model results at certain depths. This can be explained by the non-sufficient sensitivity of the flux gate magnetometers (Booker et al., 2002) used in long period systems. An active electromagnetic method can be added to complement the data quality around 10 Hz to 10 s, like CSEM (Controlled-source electromagnetic). This method only works for a very short period range and is usually used for imaging the subsurface at very low depths, for example to detect conductive features such as gas hydrates.

Before the start of a sounding, one chooses the range of the frequency and distance of

stations, which depends on the assumed depth penetration and propagation. In the past only 2D-cases could be processed so field campaigns tried to measure perpendicular to the strike direction. However new algorithms and computer techniques allow the study of 3D-cases so the outlay to observe the electrical conductivity as it exists naturally in x,y,z-direction is no longer important to discuss.
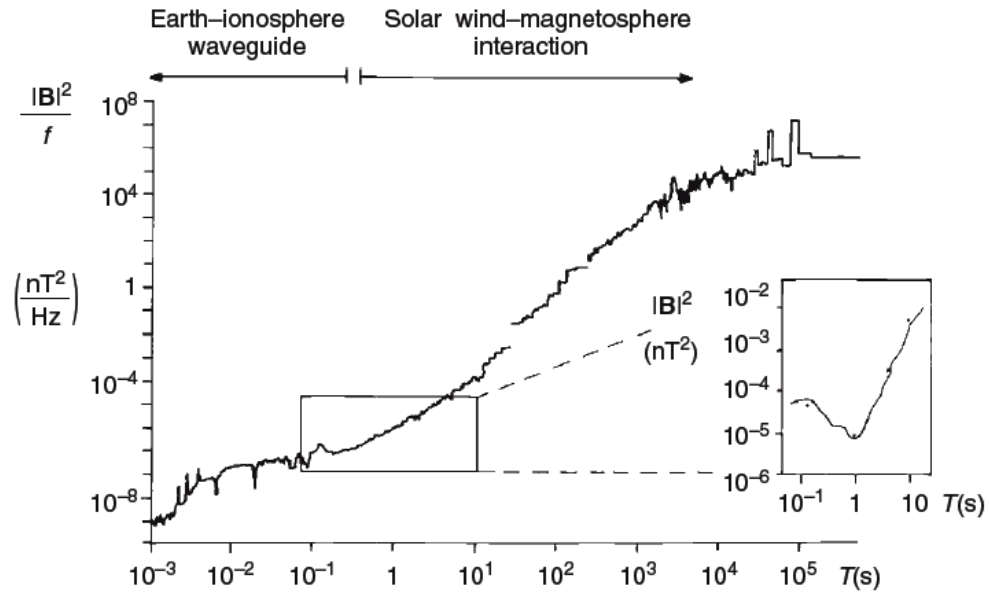
FIGURE 3.3: **Power spectrum of MT sources by 1 / f.** One can see the magnetic varations. Short period signals are generated by the interaction of the Earth-ionosphere waveguide, whereas longperiod signals are generated by solar wind-magnetosphere interaction. Image taken from Simpson and Bahr (2005).

3.2.2 Maxwell's equations

James C. Maxwell proposed four fundamental equations in 1873 which describe the propagation of electromagnetic fields. They have become known as **Maxwell's equations** and apply in a polarizable, magnetizable, homogeneous and isotropic medium:

$$\nabla \cdot \vec{B} = 0 \tag{3.1}$$

$$\nabla \cdot \vec{D} = q \tag{3.2}$$

$$\nabla \times \vec{E} = -\frac{\partial \vec{B}}{\partial t} \quad (Faraday's\ law) \tag{3.3}$$

$$\nabla \times \vec{H} = \vec{j} + \frac{\partial \vec{D}}{\partial t} \quad (Ampere's\ law) \tag{3.4}$$

The magnetic flux density and the electric field are the measured magnitudes as they contain free and bound electrical and charge density of the material. Equation 3.1 defines the magnetic field by the magnetic induction $\vec{B}$ as source-free and therefore, no magnetic monopole is existent.

- $\vec{B}$ - magnetic flux density or induction [T]

- $\vec{D}$ - electric displacement current [C / m^2]

- q - electric current density [C / m^3]

- $\vec{E}$ - electric field [V / m]

- $\vec{H}$ - magnetic intensity [A / m]

- $\vec{j}$ - electric current density [A / m^2]

In Figure 3.4 Ampere's and Faraday's law are illustrated. The magnetic intensity $\vec{H}$ has curls developed by the electric current density $\vec{j}$ and time-varying displacements. Faraday's law as stated in equation 3.3 says that the electric field $\vec{E}$ couples in a closed loop with the $\vec{B}$-field running parallel to the axis of the induced electric field. Maxwell's equations can be associated with the material equations (3.5) and Ohm's law (3.6) in the following section.

$$\vec{B} = \mu \vec{H} \quad \mu = \mu_0 \mu_r; \quad \vec{D} = \epsilon \vec{E} \quad \epsilon = \epsilon_0 \epsilon_r \tag{3.5}$$

$$\vec{j} = \sigma \vec{E} \tag{3.6}$$

The flow of an electric field is controlled by the conductivity σ in $[S/m]$ and its reciprocal σ is the resistivity ρ in $[\Omega m]$.

- μ - magnetic permeability

- μ_0 - magnetic permeability in vacuum [$\mu_0 = 4\pi \cdot 10^{-7}$ Vs / Am]

- μ_r - relative magnetic permeability

- ϵ - electrical permittivity

- ϵ_0 - electrical permittivity in vacuum [$\epsilon_0 = 8.85 \cdot 10^{-12}$ F / m]

- ϵ_r - relative electrical permittivity
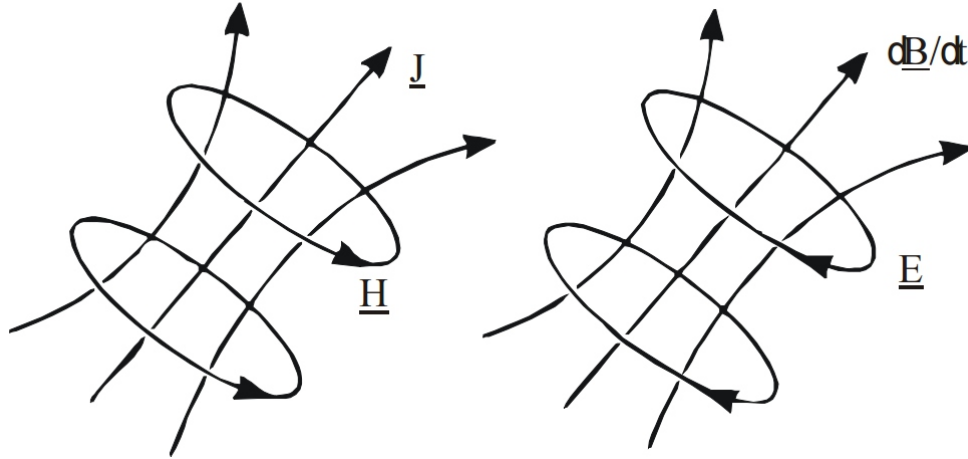
FIGURE 3.4: **Illustration of Maxwell's equations.** Amperes's law on the left shows
an electric current causing a magnetic eddy current. Faraday's law on the right side
shows a time varying magnetic field that causes an electric eddy field. Image taken
from Brasse (2011)

Magnetotellurics uses a very low frequency range from 0.0001 < f < 1,000 Hz in the
the geomagnetic deep sounding process, so the assumption of a quasi-stationary field is
legit. Because of this assumption the partial time derivative of the electric displacement
vector $\vec{D}$ becomes zero and is disregarded. This also means there is and will be no
electric charge density so Q becomes zero aswell. Variations of relative permeability and
relative permittivity are negligible compared to the variations of bulk conductivity of
rocks ($\mu_r = 1$).

At this point, one can connect Equation 3.5 and 3.6 with Maxwell's equations rewritten
in the form:

$$\nabla \times \vec{E} = -i\omega\vec{B} \tag{3.7}$$

$$\nabla \times \vec{B} = \mu_0\sigma\vec{E} \tag{3.8}$$

$$\nabla \cdot \vec{B} = 0 \tag{3.9}$$

$$\nabla \cdot \vec{E} = q \tag{3.10}$$

These Equations 3.8 and 3.7 develop into a new Equation 3.11 when there is no current source within the Earth in a homogeneous half-space as 3.10 turns zero ($\nabla \cdot E = 0$). It is known as the Telegrapher's equation. F stands for any vector and can be replaced by E or B, which is described in 3.12 and 3.13. This happens under the assumption that an harmonic time surface amplitude E_0 depends on the form $e^{-i\omega t}$. These equations explain the propagation of the electric and magnetic field depending on their source. So in general, the Telegrapher's equation describes the propagation of electromagnetic waves through a homogeneous medium as mathematically formulated in Equation 3.14.

$$\nabla \times (\nabla \times \vec{F}) = (\nabla \cdot \nabla \cdot \vec{F}) - \nabla^2 \vec{F} \tag{3.11}$$

$$\nabla^2 \vec{E} = i\omega\mu_0\sigma\vec{E} \tag{3.12}$$

$$\nabla^2 \vec{B} = i\omega\mu_0\sigma\vec{B} \tag{3.13}$$

$$\nabla^2 F = \mu_0\sigma\frac{\partial \vec{F}}{\partial t} + \mu\epsilon\frac{\partial^2 \vec{F}}{\partial t^2} \tag{3.14}$$

3.2.3 Skin depth

The wave is described by $Amplitude \cdot e^{i\omega t}$ so the displacement current becomes unimportant compared to the conductive current which leads to Equation 3.15. The angular frequency is defined as $\omega = \frac{2\pi}{T}$ with T in [s]. The introduction of κ as a complex wave number with $\kappa = i\omega\mu\sigma$ leads to the Helmholtz Equation (Schmucker et al., 1973).

$$\nabla \times (\nabla\vec{F}) = i\omega\mu\sigma\vec{F} = \kappa^2\vec{F} \tag{3.15}$$

The real part of this number is used to calculate the skin depth. Inserting the magnetic permeability $\mu_0 = 4\pi \times 10^{-7}$, as mentioned before, and the replacement of the conductivity with resistivity leads to Equation 3.17. It describes the skin depth δ in dependence of the parameters resistivity ρ and period T.

$$\delta = \frac{1}{\kappa} = \sqrt{\frac{2}{|\kappa^2|}} = \sqrt{\frac{2}{\omega\mu_0\sigma}} \tag{3.16}$$

$$\delta \approx 0.5\sqrt{\rho T} \quad [km] \tag{3.17}$$

This is the simplified equation to assume the penetration depth of a wave signal. A short period signal decays quicker than a long period one. Likewise, the resistivity of

the conductive material in the subsurface is important since the electromagnetic wave will decay faster in a resistive environment. This is illustrated in Figure 3.5.
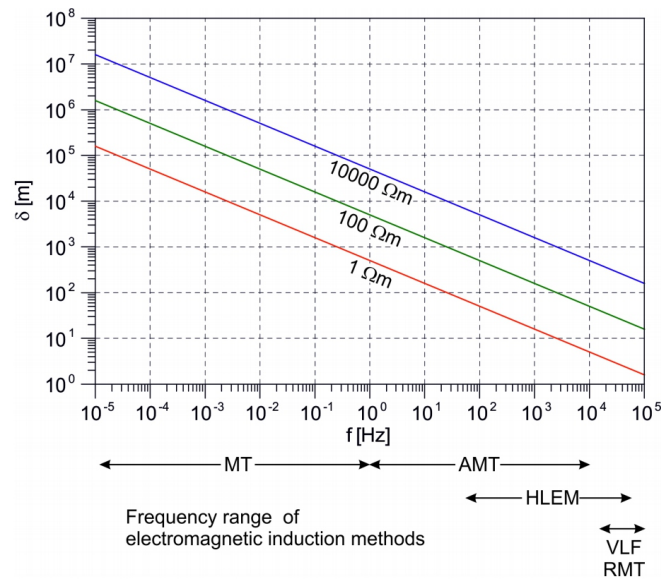
FIGURE 3.5: **Penetration depth or skin depth in a homogeneous half-space.** Red line shows the commonly given resistivity for sedimentary rocks, the green one for metamorphic rocks and the purple line stands for igneous rocks. The frequency ranges under the graph show different periodic ranges of MT techniques. Active methods like the HLEM (Slingram) have a lower effective penetration depth due to the geometric damping in the near field. Image taken from Brasse (2011).

3.2.4 Transfer functions of MT

This chapter deals with the different structure case analysis that are necessary to observe when working with MT data sets. As a passive technique, MT uses the fluctuations in the natural electric and magnetic field in orthogonal direction at the surface of the Earth as it was explained earlier. The recording of data is time-dependent analyzed in the frequency domain. MT data are recorded in five directions: two in the E-field and three in the B-field as there is a vertical field also. North is defined as x-direction and East as y-direction. To define the correlation of the measured data and the conductive features in the subsurface, MT defines the Impedance Tensor Z as a complex, frequency-depending transfer function between the horizontal fields. So the impedance tensor Z_{xy} is the ratio of the electric field in x-direction (E_x) and the magnetic field in y-direction (B_y). Cantwell and Madden stated in 1960, that a linear relation of $\underline{Z}$ between the components of the electric field $\vec{E}$ and the magnetic field $\vec{B}$. This Equation 3.18 expresses the basis for a 3-D case and allows the analysis of 2-D and 1-D cases, too.

$$\vec{E} = \underline{Z}\vec{B} = \begin{bmatrix} E_x \\ E_y \end{bmatrix} = \begin{bmatrix} Z_{xx} & Z_{xy} \\ Z_{yx} & Z_{yy} \end{bmatrix} \begin{bmatrix} B_x \\ B_y \end{bmatrix} \tag{3.18}$$

This can also be written in a complex form:

$$Z_{xy}(\omega) = \frac{E_x(\omega)}{B_y(\omega)} = |Z_{xy}| \cdot e^{i\phi} \tag{3.19}$$

Every field component is depending on the location and the frequency. This means the tensor $\underline{Z}$ contains a real and an imaginary part and therefore is complex as it involves magnitude and phase (Z_{ij}; $i = x, y$ $j = x, y$). This means an apparent resistivity ρ_a and a phase ϕ measured in [°] can be obtained.

$$\rho_{a_{ij}} = 0.2T \left| \underline{Z}_{ij} \right|^2 \tag{3.20}$$

$$\phi_{ij} = arctan \frac{Im\underline{Z}_{ij}}{Re\underline{Z}_{ij}} \tag{3.21}$$

The impedance phase is the difference between the electric and the magnetic field. In a uniform half-space, the impedance phase is 45°. When conductivity increases, the phase grows too and vice versa. There is no observable static shift on the impedance phase in comparison to the impedance. Additionally, the impedance holds important information about the dimensionality and direction of a medium. Presentations are usually made via single logarithmic scales.

3.3 Dimensionality of MT data

The distribution of Earth's interior conductance can be described in 1-D, 2-D or 3-D case.

3.3.1 1-D case

The conductivity depends only on depth z so ($\sigma = \sigma(z)$). In a homogeneous subsurface, the horizontal electric field independently runs ahead from the magnetic field with ϕ_{xy} = 45° and ϕ_{yx} = 225°. The most simple way to describe the Earth is a layered half-space. The phase is located in the first quadrant and increases over 45° when the electromagnetic response penetrates into a higher conductive medium and vice versa. This results in Equation 3.22 and leads to Equation 3.23.

$$\begin{bmatrix} E_x \\ E_y \end{bmatrix} = \begin{bmatrix} 0 & Z_{xy} \\ -Z_{yx} & 0 \end{bmatrix} \begin{bmatrix} B_x \\ B_y \end{bmatrix} \tag{3.22}$$

The main diagonal elements (Z_{xx} and Z_{yy}) of the impedance tensor have become zero. The off-diagonal components are equal in magnitude but different in signs.

$$Z_{xx} = Z_{yy} = 0; \qquad Z_{xy} = -Z_{yx} \tag{3.23}$$

3.3.2   2-D case

In case of a 2-D structure, the conductivity feature constantly is aligned along the electromagnetic strike. This means Z_{xx} and Z_{yy} are equal in magnitude but differ in their signs with the off-diagonal being different aswell. The ideal 2-D case would be a conductivity change along one horizontal direction as one of the diagonal elements of the impedance tensor. This would lead to an equal magnitude but different in signs. The distribution of the conductivity depends now on depth and one of the two horizontal components ($\sigma = \sigma(y,z)$).

$$Z_{xx} = -Z_{yy}; \qquad Z_{xy} \neq -Z_{yx} \tag{3.24}$$

$$\begin{bmatrix} E_x \\ E_y \end{bmatrix} = \begin{bmatrix} 0 & Z_{xy} \\ Z_{yx} & 0 \end{bmatrix} \begin{bmatrix} B_x \\ B_y \end{bmatrix} \tag{3.25}$$

Here, Maxwell equations decouple into two separate systems of equations called E-Polarization (TE-mode for transverse electric) and B-Polarization (TM-mode for transverse magnetic). This is a result of the electric and magnetic field being perpendicular to each other and electromagnetic fields being treated as plane waves.

TE-mode	TM-mode
$\dfrac{\partial B_x}{\partial y} = \mu_0 \sigma E_z$	$\dfrac{\partial B_z}{\partial y} = \dfrac{\partial B_y}{\partial z} = \mu \sigma E_x$
$\dfrac{\partial E_x}{\partial z} = \dfrac{\partial B_y}{\partial t} = -i\omega B_y$	$\dfrac{-\partial B_x}{\partial z} = \mu_0 \sigma E_y$
$\dfrac{\partial B_z}{\partial y} = \dfrac{\partial B_y}{\partial z} = \mu \sigma E_x$	$\dfrac{\partial E_z}{\partial y} - \dfrac{\partial E_y}{\partial z} = i\omega B_x$

The E-Polarization describes currents flowing parallel to x-direction in terms of the electromagnetic field components E_x, E_y and B_z. The B-Polarization describes currents flowing perpendicular to y-direction in terms of the electromagnetic field components B_x, E_y and E_z. This is illustrated in Figure 3.6 to clarify the split of Maxwell's equations in a 2-D case with two different conductivity bodies next to each other. In case of a small anomaly close to the station small charges on boundaries will not be recorded. This results in a frequency-independent **static shift** of the apparent resistivity. The transfer functions phase is not affected by this effect.
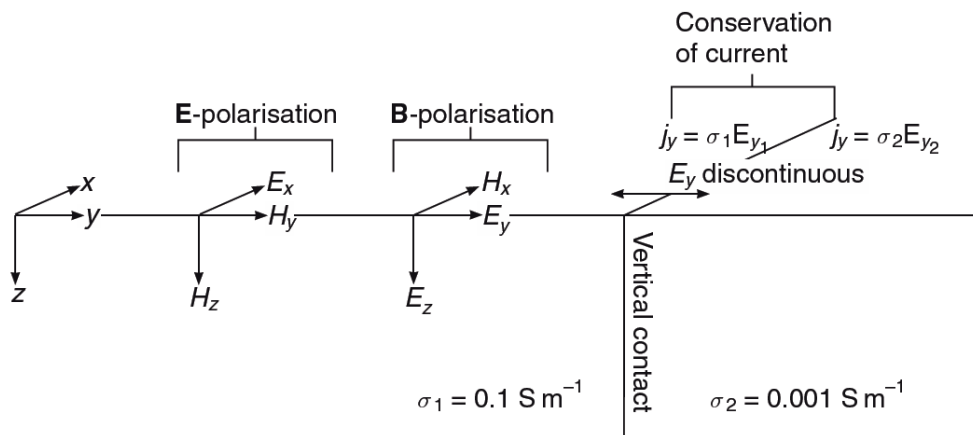
FIGURE 3.6: **Conductivity model with distribution of fields for a 2-D case**
Conductivity in $\sigma_1 > \sigma_2$. Image taken from Simpson and Bahr (2005).

3.3.3 3-D case

In a real world, the distribution of conductivity is described as the 3-D case with varieties in x-,y- and z-direction ($\sigma = \sigma(x, y, z)$). Maxwell's equations have to be solved completely since all elements of the impedance tensor are unequal zero.

$$\underline{Z} = \begin{pmatrix} Z_{xx} & Z_{xy} \\ Z_{yx} & Z_{yy} \end{pmatrix} \tag{3.26}$$

3.4 The phase tensor

Caldwell et al. introduced a new method in 2004 to determinate the dimensionality and strike of a magnetotelluric data set. Compared to earlier methods, the phase tensor does not need a preassumption of the subsurface structure. Furthermore, it is not affected by 3-D inhomogeneities (Caldwell et al., 2004) as a result of the phase tensor being a distortion-free 3-D response. It has become an accepted and valuable tool for magnetotelluric interpretation in the last year with advances by and critical argumentation for example by Berdichevsky and Dmitriev (2008), Weidelt and Chave (2012) or Booker (2013).

The phase tensor is described as the relationship between the horizontal magnetic H and electric E field vectors at an MT site by Equation 3.27 or in Cartesian coordinates 3.28 (x, y and z).

$$E = Z \cdot B \tag{3.27}$$

$$\begin{bmatrix} E_x \\ E_y \end{bmatrix} = \begin{bmatrix} Z_{xx} & Z_{xy} \\ Z_{yx} & Z_{yy} \end{bmatrix} \begin{bmatrix} B_x \\ B_y \end{bmatrix} \tag{3.28}$$

E and H are driven by quasi-stationary physical phenomena outside Earth, while Z is assumed to be a stable property of the subsurface electrical conductivity structure (Booker et al., 2013). Those Z distortions are always an issue for MT surveys since small-scale structure can not be resolved completely. Its phase stays unaffected and is defined by the ratio of the real and imaginary part of Z Equation 3.29 and its phase tensor as in Equation 3.30.

$$\phi = \frac{Re(Z)}{Im(Z)} = \begin{bmatrix} \phi_{11} & \phi_{12} \\ \phi_{21} & \phi_{22} \end{bmatrix} \tag{3.29}$$

$$\phi = X^{-1} \cdot Y \tag{3.30}$$

The real and imaginary part of the conventional complex MT is described in X and Y. For a 2-D matrix, the following applies (Booker et al., 2013):

- It is free of distortion from near-surface inhomogeneities after the galvanic response is frequency independent and produces "static offsets" in MT soundings.

- It has diagonal only elements which are equal for 1-D and unequal for 2-D geo-electric structures.

- It is asymmetric (it has a nonzero skew angle , see Figure 3.7) for 3-D structures.

- The dimensionality and directionality of background geoelectric structures can be determined.

The magnetotelluric phase tensor can be represented graphically for a better understanding as it is in Figure 3.7. It is described by three values: the magnitudes ϕ_{min} and ϕ_{max} and the skew angle β.
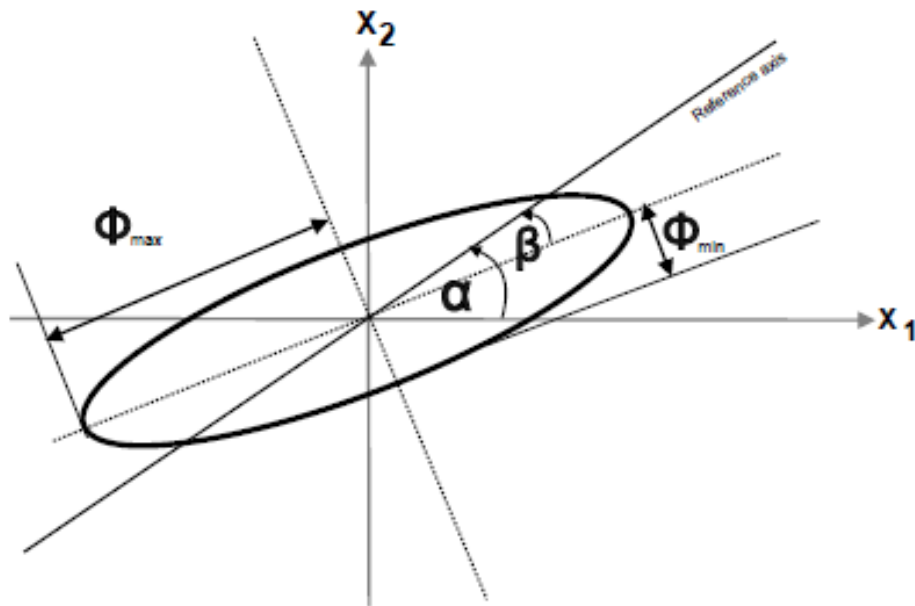
FIGURE 3.7: **Graphical presentation of a 3-D phase tensor after Caldwell et al. (2004).** Angle minimum ϕ_{min} and maximum ϕ_{max} of the ellipse describe the axes values. Angle α presents the dependence on the coordinate and β displays the skew. The result of the subtraction of $\alpha - \beta$ describes the direction of the phase tensor ellipse.

The algebraic presentation for the phase tensor can be simplified in the trace 3.31, the skew 3.32 and the determinant 3.33.

$$tr(\phi) = \phi_{11} + \phi_{22} \tag{3.31}$$

$$sk(\phi) = \phi_{12} - \phi_{21} \tag{3.32}$$

$$det(\phi) = \phi_{11}\phi_{22} - \phi_{12}\phi_{21} \tag{3.33}$$

First order functions are obtained from this one $\phi_1 = \frac{tr(\phi)}{2}$, $\phi_2 = [det(\phi)]^{\frac{1}{2}}$ and $\phi_3 = \frac{sk(\phi)}{2}$.

The minimum and maximum angle of ϕ can be derived from the information of the phase tensor (Equation 3.29) with the determinant of X: $det(X) = X_{11}Y_{22} - X_{21}Y_{12}$

$$\phi_r = \begin{bmatrix} \phi_{11} & \phi_{12} \\ \phi_{21} & \phi_{22} \end{bmatrix} = \frac{1}{det(X)} \begin{bmatrix} X_{22}Y_{11} - X_{12}Y_{21} & X_{22}Y_{12} - X_{12}Y_{22} \\ X_{11}Y_{21} - X_{21}Y_{11} & X_{11}Y_{22} - X_{21}Y_{12} \end{bmatrix} \tag{3.34}$$

$$\phi_{min} = \Phi_2 - \Phi_1; \qquad \phi_{max} = \Phi_1 + \Phi_2 \tag{3.35}$$

The skew angle β is the measure of the asymmetry of the phase tensor and is mathematically defined in Equation 3.36 while Alpha is a term depending on the coordinate system Equation 3.37. It can not be expressed as a function of the coordinate invariants (Caldwell et al., 2004).

$$\beta = \frac{1}{2} \ tan^{-1}\frac{\phi_3}{\phi_1} = \frac{1}{2} \ tan^{-1}(\frac{\phi_{12} - \phi_{21}}{\phi_{11} + \phi_{22}}) \tag{3.36}$$

$$\alpha = \frac{1}{2} \ tan^{-1}(\frac{\phi_{12} + \phi_{21}}{\phi_{11} - \phi_{22}}) \tag{3.37}$$

The conclusion is that for 1-D regional conductivity structure the phase tensor is characterized by a single coordinate invariant phase equal to the 1-D impedance tensor phase. This means the ellipse is a circle. In a 2-D structure the phase tensor is symmetric with one of its principal axes aligned parallel to the strike axis of the regional structure. The values of the phase tensor are the transverse electric and magnetic polarization phases. In the 3-D case, the phase tensor is nonsymmetric and has a third coordinate invariant which is a distortion-free measure of the asymmetry of the regional MT response. If the skew angle values higher than $\pm 5°$ a 3-D feature can be assumed.

3.5 Induction Arrows

A full representation of the 3-D structure is not given only by the impedance function. The vertical electric and magnetic field are not part of this function. However E_z is not present as the air is assumed to be an insulator. Only in the E-Polarization exists an occurence of a vertical magnetic field B_z which is known as the magnetic transfer function. The relationship between the vertical B_z and the horizontal components B_x and B_y is described in Equation 3.38:

$$B_z = T_{zx}B_x + T_{zy}B_y \tag{3.38}$$

$\underline{T} = (T_{zx}, T_{zy})$ describes the geomagnetic transfer function (it is also called tipper, from *to tip* as the magnetic field vector *tips* out of the horizontal). Like the impedance Z, it is a complex function depending on the frequency or period. This results in the real and imaginary arrow represented as **induction arrows**. The In-Phase and Out-of-Phase are described by the following two Equations 3.39 for the real arrow and 3.40 for the imaginary arrow (Schmucker et al., 1970). e_x and e_y describe unit vectors in this equations.

$$\underline{P} = ReT_x\underline{e}_x + ReT_y\underline{e}_y \tag{3.39}$$

$$\underline{Q} = ImT_x\underline{e}_x + ImT_y\underline{e}_y \tag{3.40}$$

There are two known conventions to represent the induction arrow: the Parkinson convention (Parkinson et al., 1959) with the arrows pointing towards a good conductor (in comparison to his surrounding environment) and the Wiese convention (Wiese, 1962) in which they point away. The induction arrow holds information by its length (Equation 3.41) and direction (Equation 3.42). As stated before, a complex function the equation applies for the real and imaginary part.

$$T_{Re/Im} = \sqrt{Re/Im(T_{zx})^2 + Re/Im(T_{zy})^2} \tag{3.41}$$

$$\alpha_{Re/Im} = arctan\frac{Re/ImT_{zy}}{Re/ImT_{zx}} \tag{3.42}$$

Like the impedance tensor, the tipper differs in the 1-D, 2-D and 3-D case. In a 1-D case, T_{zx} is equal to T_{zy} and therefore 0. In a 2-D only $T_{zx} = 0$, but T_{zy} becomes the

result of the fraction of the vertical magnetic field B_z and the horizontal B_y. A 3-D case covers every direction of x and y and different directions of the real and imaginary part.

Chapter 4

Forward and inverse problems in MT

This chapter will introduce the concept behind data modeling in geophysical approaches. It starts from the scratch with simple forward problems and inverse problems and how they get solved. In this work, the 3-D MT software ModEM written by Egbert and Kelbert will be used. The algorithm was developed in Fortran 90/95 which does support different inversion algorithms (NLCG, alias non-linear conjugate gradient method was used in this thesis), forward modeling codes, data functionals, model parametrization and regularizations and so on. The non-commercial software ModEM is capable of solving the inversion of impedances and related transfer functions (vertical and interstation). It was possible to build an internal LAN network at the Freie Universität (FU) Berlin to use several processors of different computers by using Message Passing Interface (MPI). Usually, four to five computers with Windows Core-i7 PCs were calculating in a network for some days per model. In general, four periods per decade were used to achieve a reasonable calculation time, the rest was discarded. Additionally, the software Grid3D by N. Meqbel (pers. comm.) was used to create the initial model.

4.1 General inverse problem

The aim of a geophysical data set is to calculate a model which is a perfect and exact copy of the real world in an ideal case. An initial model is given certain parameters to find a certain model. The relation and solution of data and modeling introduced in this chapter is described by Aster et al. (2005). Supplementary literature by Ritter (2016), Egbert et al. (2012) and Kelbert et al. (2014) was used.

The general statement of the inverse problem can be described by the operator $\underline{G}$, as

a matrix, being a linear or non-linear operator depending on the problem. The vector $\underline{d}$ is the data vector and $\underline{m}$ the best fitting model vector. This is written as a linear problem here, however in geophysics it is a non-linear problem and can only be solved by an iterative method.

$$G\underline{m} = \underline{d} \quad or \quad d_i = \sum Gm \quad i = 1, ..., n \; j = 1, ..., p \tag{4.1}$$

The modeling can be divided into two parts: the forward and inverse modeling. A. N. Tikhonov proposed the most common regularization method for MT:

$$Ax = b \qquad d = A(m) \tag{4.2}$$

The forward problem can be conceptually formulated as the following:

$$Model - - - - - - - - - > Data$$
$$\underline{d} = \text{G } \underline{m}$$

The inverse problem is considered the "inverse" to the forward problem which relates the model parameters to the data that one observes:

$$Data < - - - - - - - - - Model$$
$$\underline{m} = G^{-1}\underline{d}$$

A main problem of the inversion result is the difference between the real model $\widehat{m}$ and the calculated inverse model m. The difference between these two models is called residuum. It is required to minimize the difference as much as possible for a realistic resulting model. The calculated data Gm also have a residual e compared to d.

$$\underline{d} = \text{G } \underline{m} + \underline{e}$$

The reasonable approach is now to find the best approximate solution to minimize the actual misfit. The common widely used strategy is to find the model that minimizes the L2-norm length (Euclidean length) of the residual vector. Reforming and inserting it in the Taylor series leads to the common least square solution (Equation 4.3):

$$\|d - Gm\|_2 = \sqrt{\sum_{i=1}^{m}(d_i - G(m)_i)^2} \tag{4.3}$$

The remaining misfit can be expressed by Equation 4.4, usually known as Root Mean Square (RMS). It depends on the number of data points n and the data error Δd_t. It is important to correctly deal with data sets since the RMS value can be influenced in a poor way. Large data errors result in a decreasing RMS. In a nutshell, the RMS is only a number to check the convergence of the calculated data and model. This means the observer has to compare and check several other aspects of his survey to control the misfit.

$$RMS = \sqrt{\frac{1}{n} \sum_{i=1}^{n} (\frac{d_i - G_i(m)}{\Delta d_i})^2} \qquad (4.4)$$

General inverse problems are depending on the amount of parameters in comparison to the data set. The following classification is divided into three cases (Aster et al., 2005):

- **1) Over-determined** there are more data points than model parameters in the equation. It is a non-linear problem and may be solved, e.g., by the method of least squares. The over-determined system usually has no solution, but the equation system has many or one solution (m << d).

- **2) Under-determined** there is less equations than variables. Usually there are infinitely solutions but sometimes there is none (m >> d).

- **3) Homogeneous** system of equations with all zeroes on the right-hand side is homogeneous. There is at least one solution with all variables being zero (m≈d).

4.2 Inverse problems of MT

MT commonly faces the under-determined problem (m >> d) in inversion. This is a result of the limited number of measurements done in geophysical surveys. To minimize the misfit between the data and model response an iterative technique is used. In multi-dimensional, 2-D or 3-D inverse models, problems are non-unique to be solved as they are numerically unstable. This is named by the term ill-posed. Well-posed problems have to fulfill at least one argument such as: *Existence*, with at least one theoretical fitting model for the data, *Uniqueness*, where one model fits the data or *Stability*, as small changes in the model parameters will change the model response, hence do not affect the data though.

As noted, the inverse problem of MT is the amount of free model parameters compared to the data. One can achieve several fitting models for the same data and the final aim is to eliminate the ambiguity of the problem. Regularization is the key for this matter as it is stated for MT by Tikhonov.

$$\phi(m) = (d - f(m))^T C^{-1}{}_d (d - f(m)) + \lambda(m - m_0)^T C^{-1}{}_m (m - m_0) \qquad (4.5)$$

The penalty function ϕ is defined by Equation 4.5 with $f(m)$ as forward mapping, m_0 as the prior or initial guessed model, λ as the regularization or trade-off parameter and C_m as the model covariance also known as the regularization term. $C_d^{-1} = D^T D$ and C_d is the data covariance matrix. C_m^{-1} is described by $R^T R$, where R is a discrete representation of a gradient or higher order derivative operator (Tarantola, 1978). The reader is refered to Tikhonov et al. (1977) if he is interested in more detail.

4.3 ModEM and Grid3D

The software ModEM is a prototype modular system of parallel computer codes for inversion of electromagnetic (EM) geophysical data. It was developed by Egbert, Kelbert and Meqbel at the Oregon State University and GFZ Potsdam over the last decade (Egbert and Kelbert, 2012). The numerical approach is structured as a flexible system to create a system for several EM geophysical data types with different inverse problem solution strategies and regularization models. The organization is illustrated in Figure 4.1.
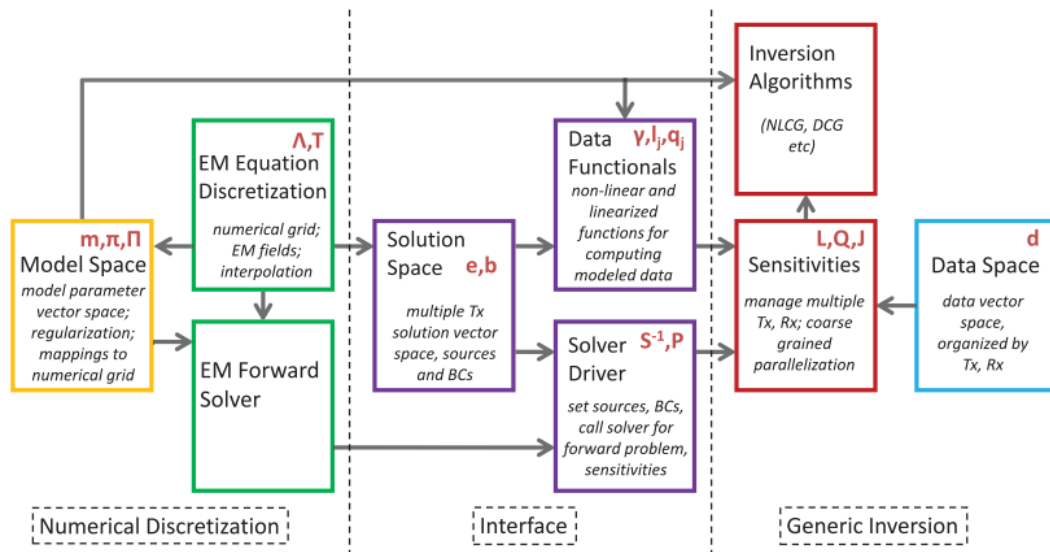
FIGURE 4.1: **Schematic overview of the Modular Electromagnetic Inversion (ModEM) system after Egbert et al. (2012).** Groups or Modules are divided into boxes that represent certain modules. The dependence of modules to each other is represented by arrows. with dependencies defined by arrows. Tx and Rx stand for the Transmitter and Receiver, respectively.

As a free academic software, ModEM is applied to 3-D MT data, using a NLCG algorithm for the parameter search. Further additions in frequency domain controlled source EM (CSEM) have been made lately. Its memory-efficient nonlinear conjugate gradient method (NLCG) code is made to run with big data sets, including full impedance and vertical transfer functions. The error floor used was set at 5% by default. The initial model was created in Grid3D, a mesh generation software by N. Meqbel. It allows to discretize the grid of the cells easily. Also, bathymetry and topography can be added from several sources and modified. The background resistivity is chosen by local prevailing standards and can be modified in size and value as the user wishes. An important feature is the smoothing by the covariance matrix. Data sets (typical for MT: .edi files) can be modified in Grid3D, so scattered data can be removed and edited for example.

Chapter 5

3-D Conductivity Model along a transect in the Volcanic Zone

In the end of year 2002, an MT survey campaign was carried out along a transect in the Bolivian high plateau at 18°S. The field trip contained stations LUR to PAL (compare Figure 5.1) from the Eastern Cordillera to the Central Altiplano. Two years later, in 2004, the profile was augmented by stations PAR to ANT to achieve a complete network to the Chilean coast. The station SAJ, close to the volcano Sajama, was used as a reference station. The entire profile line, with a total length of 340 km, is presented in Figure 5.1.

The transect is running perpendicular to the strike of the geological structures of the Bolivian Orocline, also known as 'Arica Bend' named after the town Arica. Additionally, the contour-lines of the Wadati-Benioff-Zone run parallel to the geological units. Here, the structural trends change from N-S to NW-SE due to an eastward magmatic arc shift during the Jurassic (Scheuber et al., 1994). It was tried to keep a distance of 10 km between each station, but could not alawys be obtained due to local topography.

Previous studies were already carried out on this transect, however lacking computing power and progress of inversion codes in MT only offered 2-D solutions. The motivation behind the study is the imaging of the 3-D case along a profile line in the Bolivian Orocline and its conductive features in the underground.
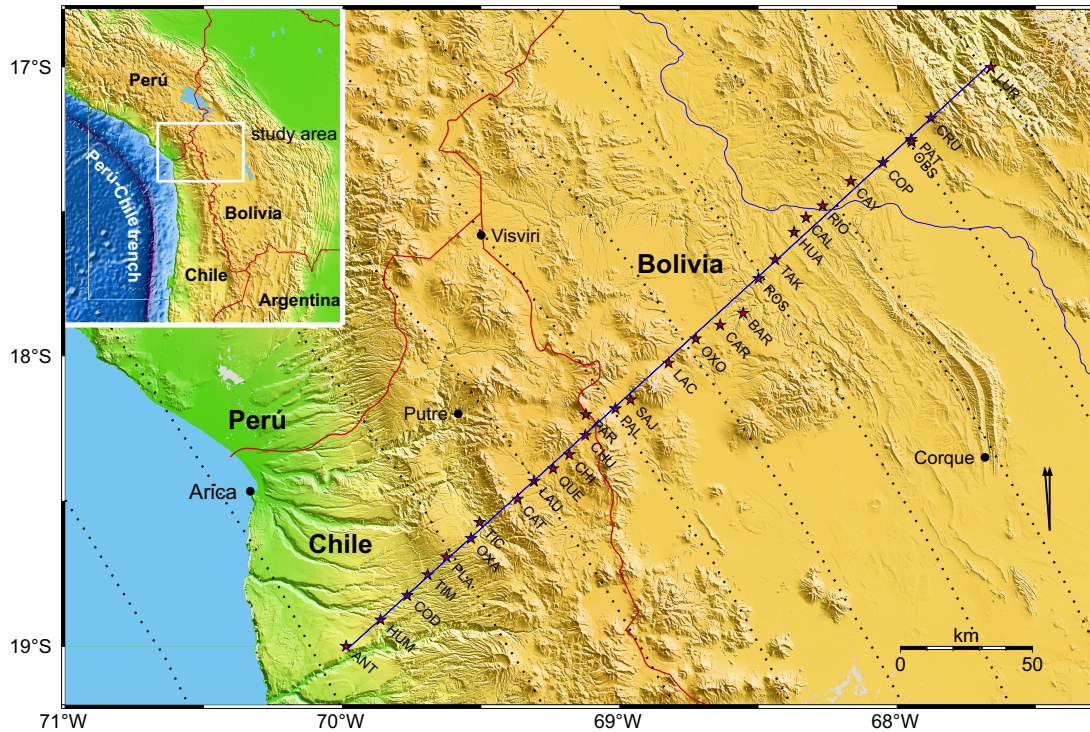
FIGURE 5.1: **Profile line at 18S in the CVZ.** Both campaigns contain 30 stations overall. The profile line runs perpendicular to the NW-SE running strike of the geological environment and the indicated contour lines of the Wadati-Benioff-Zone (dotted lines after Cahill & Isacks (1992)). Image taken and modified after Brasse & Eydam (2008).

5.1 Previous work

A first MT study was carried out in by Ritz et al. (1991) on a similar profile line. However, this study only included impedance data for periods up to 3,000 s and led to a limited insight of the upper and mid-crustal structures. Diane Eydam, a former FU student, observed important features of the subsurface by including the vertical transfer functions. The profile used extends from the Coastal Cordillera in the northernmost Chile, crossed the volcanic arc and the Altiplano high plateau in central Bolivia and ends in the Eastern Cordillera.

This chapter describes the main observations of the previous work by Brasse & Eydam (2008). Based on their findings a 3-D study will be described in the following chapter. In Figure 5.1 real part arrows corresponding to a shallow (186 s) and a deep penetration depth (1311 s) of the study are represented. Real arrows should point away from a single good conductor in a two-dimensional setting (Wiese, 1962). The highly conductive Pacific Ocean with a conductance of up to 25,000 Siemens should work as a perfect example for this, however the direction of the arrows is coast-parallel. This indicates

a possible anisotropy or faults in the Coastal Cordillera (Galindo, 2010). Furthermore, the west-vergent thrust system and perpendicular striking fault influences the arrows as one can see on two sites (tic and oxa) near the Western Cordillera Escarpment. This deflection was observed before in other publications, as for example in Brasse et al. (2006).
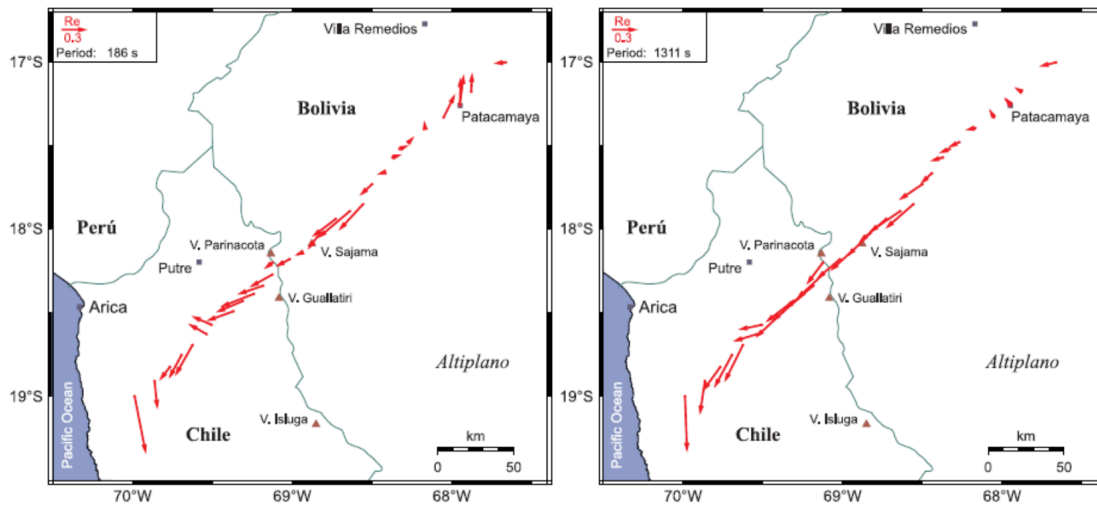
FIGURE 5.2: **Unrotated real part induction arrows at period range 186 s and 1311 s after Wiese Convention.** Deflection of the arrows near the Pacific Ocean where the coast effect is overprinted by the influence of other conductive feature with different strike. Station OBS and neighboring stations are influenced by a conductive feature near the Patacamaya observatory. Here the yx phases leave the third quadrant. Image taken from Brasse & Eydam (2008).

In the volcanic arc, the coast effect becomes less important and the induction arrows increase in length. In the Altiplano, especially in the Corque basin, the resistivities are in general very small and indicate a typical three-layer case with a conductive feature at large depths. In the Eastern Cordillera the resistivity in the subsurface increases again with the arrows at short periods pointing away from the northward. This could be caused by another conductive structure at shallow depths. Due to the questionable behavior of arrows in the forearc a study on the skewness of the impedance tensor hinted a three-dimensional feature there. In Figure 5.3, the skew of the impedance tensors has been calculated after Swift (Swift, 1986) and Bahr (Bahr, 1988). The colors indicate the skewness. Usually, a skew below 0.3 is used as a quantity for two-dimensionality, so white and light colors are important here. In the Coastal Cordillera a higher skew is observable with skewness higher than 0.6. The significant difference in the skew after Swift and Bahr leads to the assumption of a strong static shift. In the volcanic arc and Altiplano the 'shorter' periods up to 1,000 s indicate a two-dimensional structure. At longer periods a three-dimensional structure interpretation seems to be unavoidable.
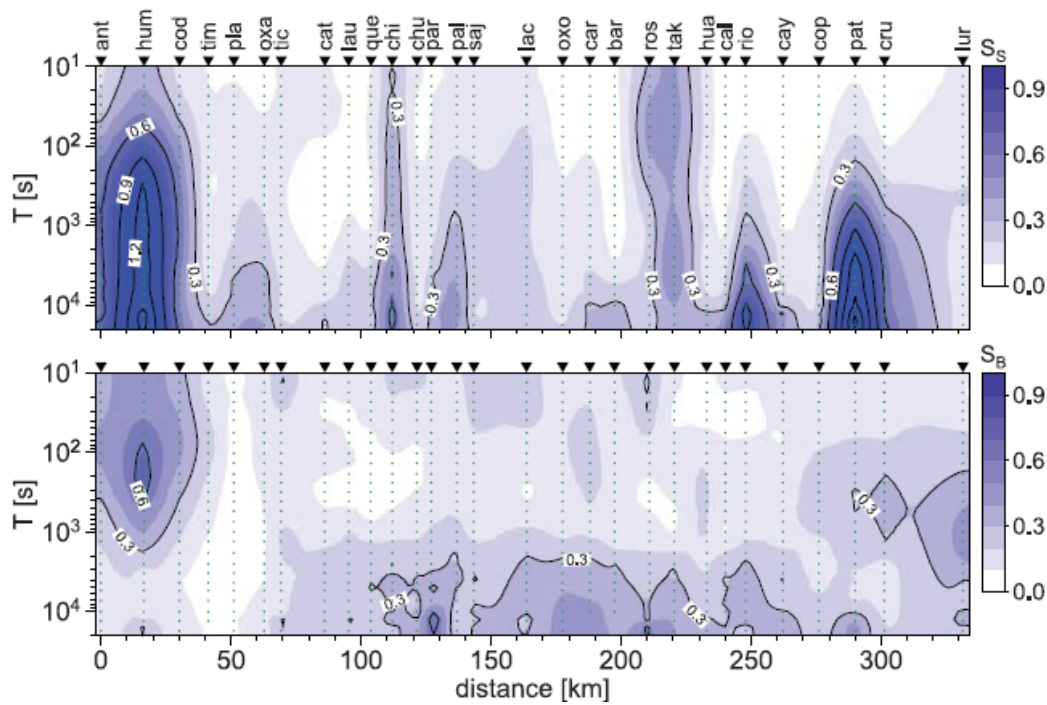
FIGURE 5.3: **Skew after Swift and Bahr (Bahr, 1988).** Near-coastal stations
indicate a three-dimensional feature with a strong static-shift. Periods shorter than
2,000 s usually show a skewness below 0.3. At larger depths skewness increases.

The two-dimensional inversion by Eydam (2008) was carried out with a NLCG algorithm
of Rodi and Mackie (2001). Several model experiments have been tried out to achieve a
good-fitting final model. This included typical attempts like different starting models,
exploration of the model space by varying the regularization parameter, specific error
floors on certain components and modes (like TE/TM and Tipper), sensitivity tests and
discretization, as well as convergence of the model. Another problem was the change
of altitude in the Central Volcanic Zone. The topography changes had at least to be
discussed and tested. As a final result, Figure 5.4 was presented. The homogeneous
half-space of the model was set at 150 Ωm and the bathymetry was included with
the ETOPO2 model. The convincing inversion model was finally calculated after 214
iterations with an RMS = 1.80. Several features were recurring in Eydams models,
however only feature D will be relevant in this thesis:

- **A) Sediments:** Probably Tertiary sedimentary layers of the central plateau with
  a thickness of 10 km. A1 can be explained by the historic geological reconstruction
  as the Corque Syncline (Sempere et al., 1990). A2 is a less deep sedimentary basin
  to the east as the northern extension of the Poopó Basin.
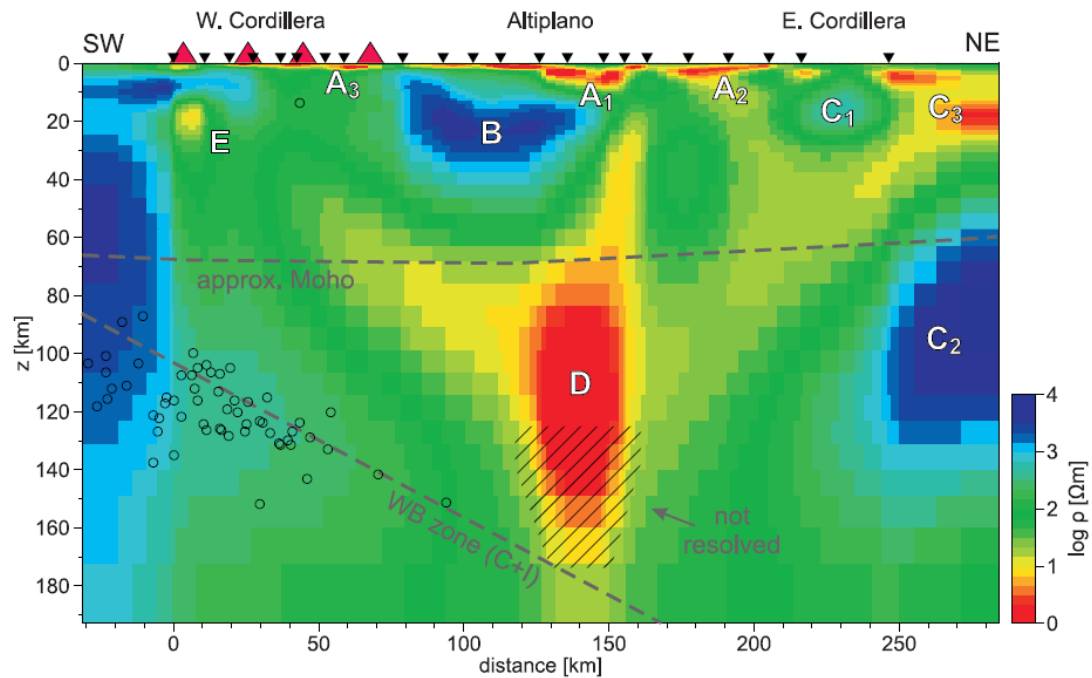
FIGURE 5.4: **Final 2-D inversion model after Brasse et al. (2008).** A1, A2 and A3 are Corque and minor basins; Feature B is an impermeable upper crust below the western Altipano; C1, C2 and C3 are resistive and conductive structures beneath the EC, C3 seems to be the EC block; Conductive feature D is a mantle wedge by the rise of fluids/melts; E is a deep crustal magma chamber below the WC. Circles display the earthquake locations (Engdahl et al., 2002). The Moho is estimated after Allmendinger et al. (1997) and the Wadati-Benioff-Zone after Cahill and Isacks (1992).

- **B) Arequipa-Block** This structure is a middle crustal zone of high resistivity that extends between the arc and the Corque Basin. This feature can probably be related to an old cratonic crust of the Arequipa bloc.

- **C) Conductive and resistive feature:** C1 contains high resistivity and should be a transition to the Paleozoic crystalline basement in the EC. Beneath, at larger depths in the EC, one can find a second poor conductor C2 which is also imaged by seismic velocity measurements in this area (Dorbath et al., 1996). C3 is a good conductive feature in mid-crustal depths which is also proposed by Schmucker et al. (1996). Yet this feature has to be viewed critically due to location at the end of the profile in the Eastern Cordillera.

- **D) Good conductor beneath the Altiplano basin:** This structure may be the most obvious anomaly but also the most interesting feature as it is located in the upper mantle and reaches into the lower crust below the Central Altiplano. The apparent resistivity is probably around 1 Ωm. It is most likely a partially molten astenospheric wedge as part of the subduction zone. Although its location

is about 100 km northeast offset from the estimated location in the backarc. This might be explainable as a result of the flat subduction process.

- **E) Conductive feature beneath the Western Cordillera:** Structure E is located at the Western Cordillera as a feature in mid-crustal depth. It could be a magma chamber, however, no recent volcanic activity was observed and near volcanoes like Taapaca are located 50 km away.

5.2   Data acquisition and processing

The measurements were made with a data logger of the FU Berlin. The data were obtained by geomagnetic coordinates and time synchronized by GPS clocks to support the remote reference processing in the field (Egbert et al., 1997). This was done to recognize possible disturbances in the transfer functions immediately. Technically this means a prewhitening- and highpass filter is used to remove distortions and bugged data, especially from the long-periodic data by instrumental drift. The data frequencies obtained were around 0.00005-0.1 Hz or 10-20000 s.

The noise is affected by serial correlation in the magnetic field and this causes a wrong estimation of the spectral component and the impedances. This effect was reduced by a method from Egbert and can be read in Simpson and Bahr (2005).

The data used in this study contained 18 frequency logs between the range 1 s and 10,000 s. It was required to remove every second measured point, so four frequencies per decade were used for the inversion. This step was based on experience and to be found as a good way between data quality and calculation time. More frequencies in the decade did not really improve the model quality but prolonged the time of every iteration between the model finding steps redundantly. This led to 9 frequencies of impedances and the vertical transfer functions. Those nine frequencies have been checked carefully for wrong or non-physical measured sets with them being removed.

Nonetheless, a check on the induction arrows has been performed, but due to its accordance to the study results of Eydam (2008) there will be no reopened discussion on that case. The extract from the the 18 frequencies has been added to the Appendix A.1.

5.3   3-D re-evaluation of the Andean transect

The more important study on the 3-D case was carried out via the phase tensor ellipses analysis. In Figure 5.5 the phase tensor ellipses are illustrated between 10 s and 10,000 s in alphabetic order; except station BAR as it could not calculate a phase tensor ellipse.
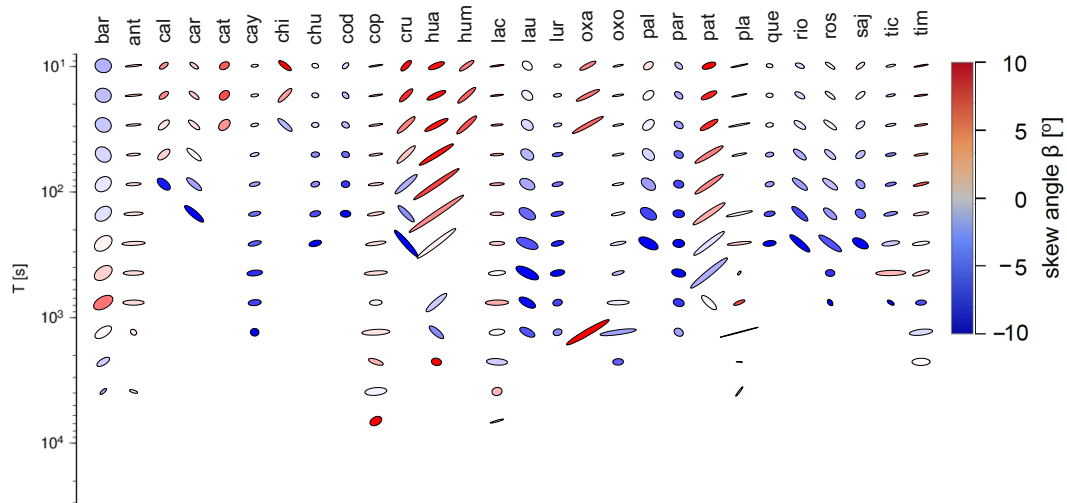
FIGURE 5.5: **Phase tensor ellipses presentation of the stations along the transect between 10s and 10,000s.** Ellipses with a skew angle of more than 10° are not colored. Please note that the stations have been presented alphabetically.

- **Coastal Cordillera and Longitudinal Valley.** Stations ANT, HUM and COD show higher skew angles or are not represented at all and got masked. These stations are influenced by the Pacific Ocean and the coastal effect on the data. Their α is in higher periods and depths close to 90°. This is explained by the split of the apparent resistivity and phase curves at near-coastal stations which will be explained in the next chapter in detail.

- **Precordillera and Western Cordillera Escarpment.** TIM, PLA, OXA and TIC are still influenced by the coast effect and show a similar behavior like the stations located in the Coastal Cordillera. Furthermore faults in the LV influence the orientation of the ellipses. A possible 3-D setting can be assumed here.

- **Western Cordillera** CAT, LAU, CHI, CHU, PAR do not show a behavior of a 3-D environment in the subsurface. Typically the Western Cordillera is dominated by 2-D structures.

- **Altiplano.** PAL, SAJ, LAC, OXO, CAR, BAR, ROS, HUA and CAL show high angles or could be masked due to a skew angle out of the allowed calculation range. Here Brasse et al. (2008) assumed a deep conductor which probably causes distortions. The following stations CAY, COP, and PAT show a less complex

structure in the underground as their phase ellipses become more circle shaped again. PAT seems to be distorted by the local observatory.

- **Eastern Cordillera.** The remaining stations CRU and LUR, ranging more north-eastward in Bolivia into the Eastern Cordillera, may indicate another structure based on the information from CRU. However, studies in this area are omissible due to the lack of information by a station network.

It was not possible to illustrate phase ellipses for sites TAK and OBS, as they were influenced by a strong 3-D conductive environment. Complimentary, the extract from 3-D Grid of the ellipses has been added to the Appendix A.4. Those extracts include extra stations from another campaign to receive more information about a possible influence in the area of stratovolcanoes Sajama, Parinacota and Taapaca.

5.4   Modeling and Results

The re-evaluation of the data offered enough indications to justify a 3-D structure study in the subsurface. To find a prior starting model it was required to test out certain parameters in the beginning. A first model was chosen with a total length of 1,600 km in x and y-direction and 800 km depth. However early inversions showed that the influence of the ocean has become astonishingly strong so it was decided to enlarge the model size in several new approaches until a total length of about 5,000 km in N-S south direction, 4,000 km in E-W and a depth of 1,200 km led to satisfying results. The ocean was added by the software Grid3D from ETOPO1. Please note that the discretization of the cells influences the authenticity of the real world. Usually in the area around the stations a single cell is sized very small (several kilometers) and increases the further away it is located. This is regulated by the increasing factor of 1.3 here. Every cell in a direction straight away from the middle of the model increases in size by the factor 1.3. For the depth usually a factor of 1.5 is used. In the Appendix A.7 an example of the cells has been added. Every station needs its own cell and should optimally be located in the middle of a cell to avoid numerical errors. A fine grid was added manually to achieve a better understanding of the local underground. The automatic centering of stations in a cell did not work satisfactorily in Grid3D, so the inversion results were rather poor and discarded. The starting model was given a background resistivity of 100 Ωm for the homogeneous half-space and 0.3 Ωm for the Pacific Ocean. Those values have been chosen from long experience in this field. The ocean was set fixed so it does not get inverted, because its high contrast would corrupt the inversion model. This has to be learned from a full study without a fixed set ocean. Figure 5.6 shows the starting

model with Nx = 34 (cells in x-direction), Ny = 61 and Nz = 47. The distance from the origin point in the x-slice to the model boundary is 2,564 km and for the y-slice 1,570 km.
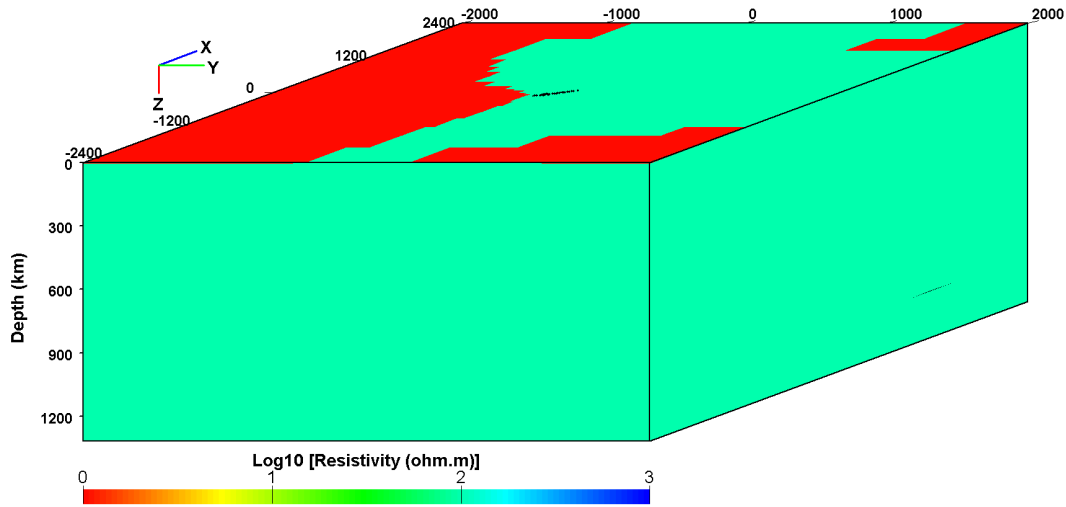
FIGURE 5.6: **Starting model of the transect in the Central Volcanic Zone.** Background resistivity is set at 100 Ωm and 0.3 Ωm for the oceans. The profile length is more than 5,000 km in N-S and about 4,000 km in E-W direction. One may recognize the crude shape of South America. Black points show the stations. Topography is not included.

5.4.1   3-D Model

With the ocean being included, primary attempts on the inversion were made with the ocean being inverted too. Its strong coastal effect influenced the calculation and the Altiplano conductor could not be resolved. To verify the existence of a good conductor in the mantle a sensitivity study was performed. A cuboid body, with a background resistivity of 1 Ωm, was inserted perpendicular to the station line in the initial model in a depth of 70 km - 120 km. There was no observable change of the features at shallow depths. The conductive feature did not change its main structure by recalculation of the resistivity and by that its existence is confirmed. It is running parallel to the local geological features such as the trench, Wadati-Benioff-Zone and the Andes. Structurewise, it seems to be more complex than a simple cuboid form. It follows a more crescent shape that runs with the geological features as the trending changes from S-N to E-W. A plan view has been added to the Appendix for the depth 70 - 120 km with an example site CAL to compare the fit for two different starting models in Appendix A.8 and Appendix A.9. Notations of features are comprehensive with other models and Eydam.

A final starting model resulted from the experience of previous work and a lot of attempts with different parameters. Taking only the impedance or the tipper to calculate changed the outcome of the model but did not sweep away significant structures that were recurring in every test performed. The final model was inverted with the full impedance with a set error floor of 5 % for every component. The vertical magnetic component included T_{zx} and T_{zy} and took the conjugate with an error floor of 5 %. Several parameters for the forward and inverse calculation were tried out to force the program ModEM to run more inversion after 200 iterations. However the calculation exited always with an RMS of 2.37. Stations ANT and HUM were excluded in the final model calculation, since they showed signs of anisotropy and coastal effects in the model and data. To find a solution for this problem a more complicated and time consuming approach would be necessary and this will be not part of this study.

In Figure 5.7 the subsurface in a depth of about 70 km to 120 km, i.e., the upper mantle is displayed. A good conductor beneath the Altiplano (D) is visible. Beneath 120 km depth it is fading, as it probably ends here. A deep resisitive feature (F) is located below the Pacific Ocean and ranges into the Western Cordillera (Plane 32) in lower depths.
Figure 5.8 displays local conductive features in the underground at lower depths. On all images the Pacific Ocean (F) is included but not inverted for. That led to a weak adjustment of boundary cells of the ocean as they did not change their given resistivity of 100 Ωm. On the coast one can see high resistive features that run along the coast towards south. In depths of 15 - 24 km a lower conductive feature (E) is found in the Western Cordillera Escarpment. (A1) is a good conductor in a depth of 16 km in the Altiplano. At station LUR (C3) a good conductor is found, too. This feature remains to be uncertain since the lack of stations in this area does not allow further studies and (C1) divides the Eastern Cordillera from the Altiplano with its high resistive structure. (A2) and (A3) are close to the surface conductive layers which probably consist of sediments. In the Western Cordillera and Precordillera a resistive feature (B) is found to be existent.
Around the transect very resistive and conductive feature can be found but they are beside the feature along the coast side questionable. With different tests like allowing the ocean to be included in the calculation most of them disappear or become weak. This happened especially when calculating only the vertical transfer function data. The main structures remained but artifacts of the inversion were almost non present.
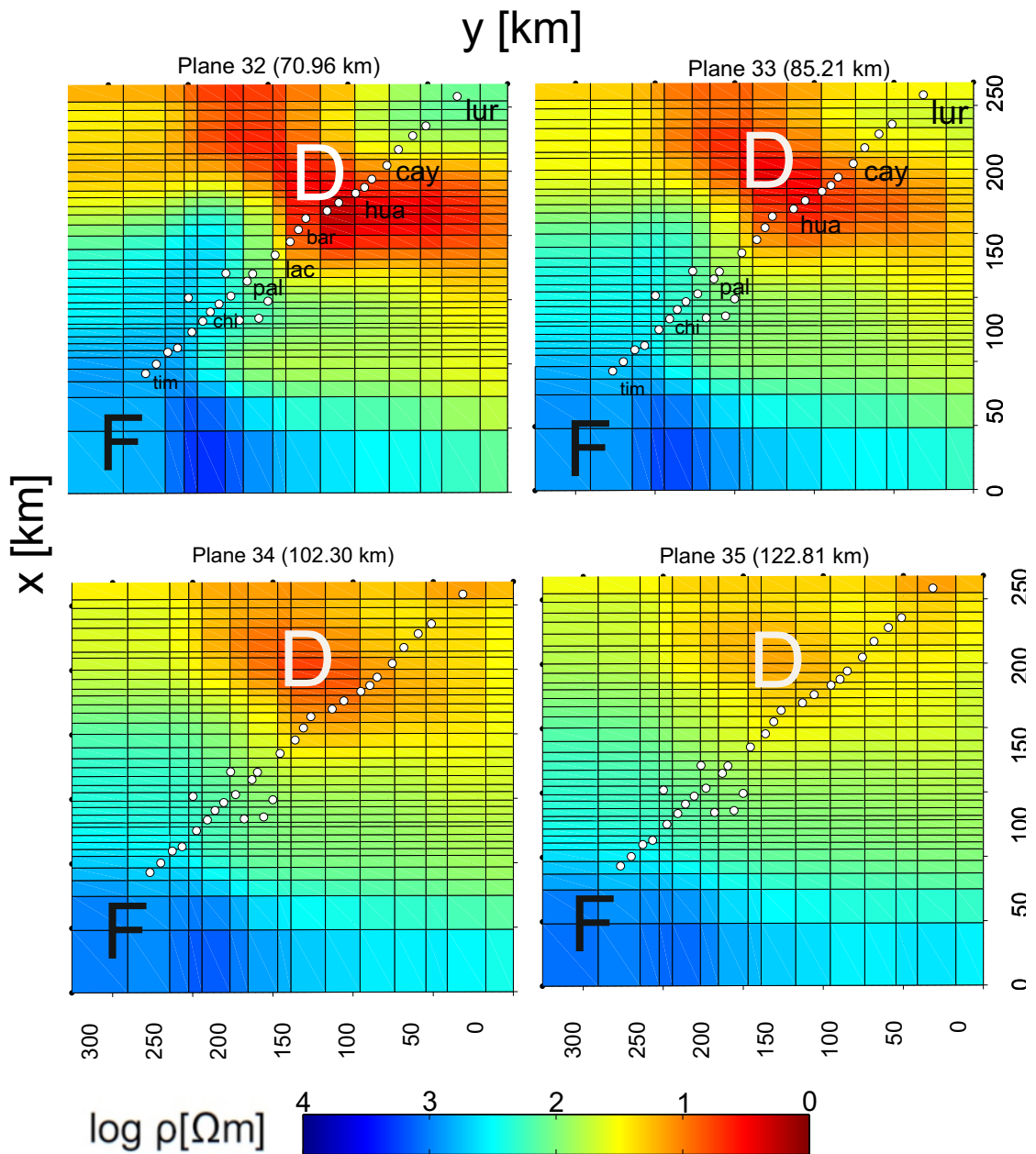
FIGURE 5.7: **Plan view of the inverse model result of the transect in depth range of 70 km - 120 km.** RMS= 2.37 with a background resistivity for the homogeneous half-space of 100 Ωm and the bathymetry 0.3 Ωm. A good conductor is found in the Altiplano (D). In 102 km the conductor fades, probably as an affect of poor resolution of the penetration depth. Beneath the Pacific Ocean (F) a resistive feature in the beneath the Moho is found. This conductor is also present in the Coastal Cordillera.
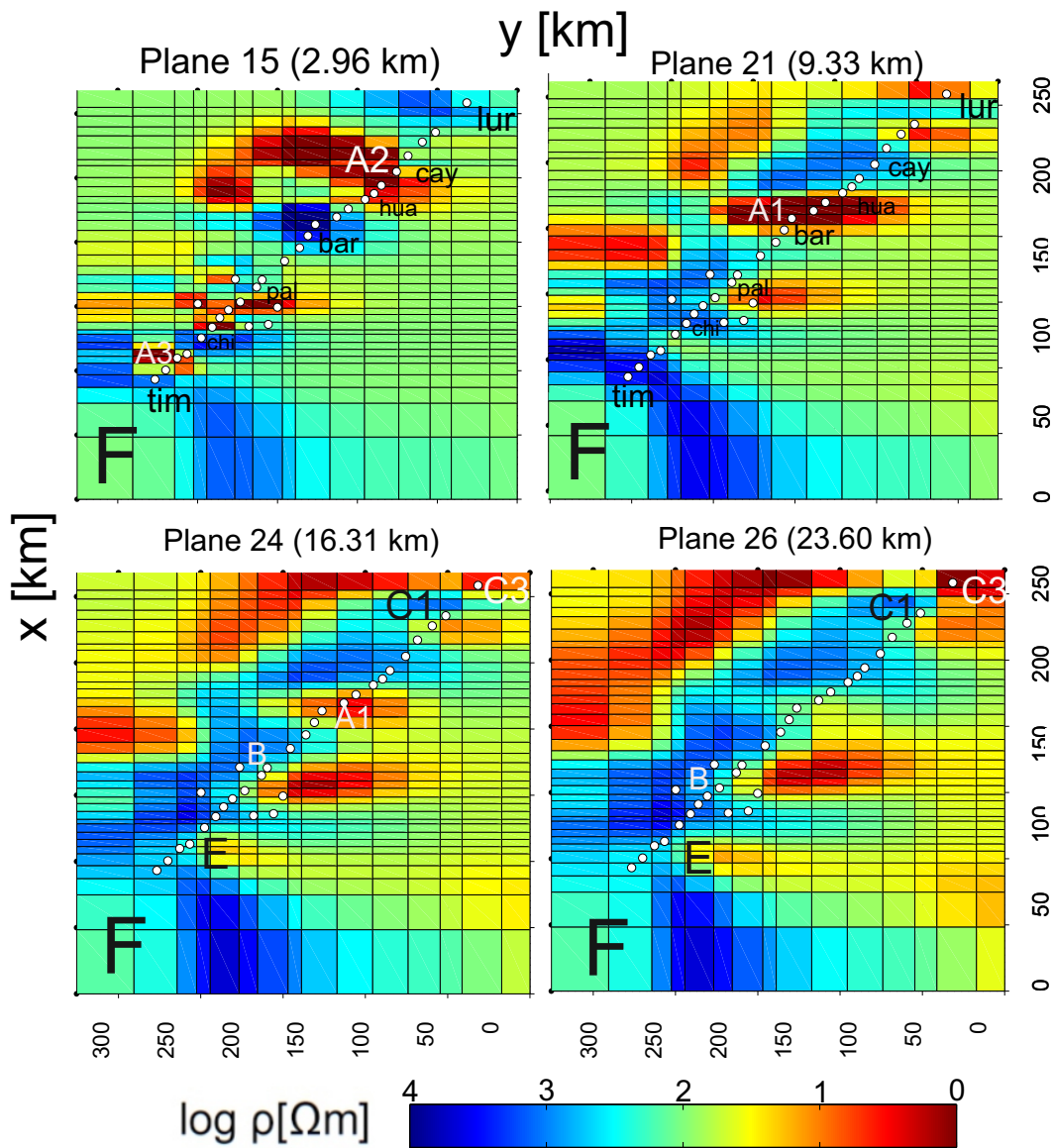
FIGURE 5.8: **Plan view of the inverse model result of the transect in depth range of 70 km - 120 km.** An RMS= 2.37 with a background resistivity for the homogeneous half-space of 100 Ωm and the sea water 0.3 Ωm. A1, A2, A3 are probably sediment layers at smaller depths with a good conductivity. B is a resistive feature in the Precordillera to Western Cordillera. C are not well resolved features in the Eastern Cordillera. Since there is almost no station the feature remains non trustworthy. Feature E is a small conductive area in the Western Cordillera Escarpment. F is the area below the Pacific Ocean.

The impedance of the main and off diagonal fits very well for most stations (poor fitting of added LMT stations from the campaign of Chapter 6), however the tipper had more problems to find a good fit. This is probably the result of the distortion by the ocean and the faults for station TIM (Figure 5.9). The typical split of apparent resistivity and phase curves for forearc stations is observable. This is a result of the coast effect and is backed up by the behavior of the induction vectors which run coast parallel with an angle $\neq 180°$ (compare 5.10). Additionally, a second exemplary site CHI is illustrated to show the better fit for the transfer function. Being part of the Western Cordillera to Altiplano and therefore the central part of the profile line, it is no longer influenced by a coastal effect.
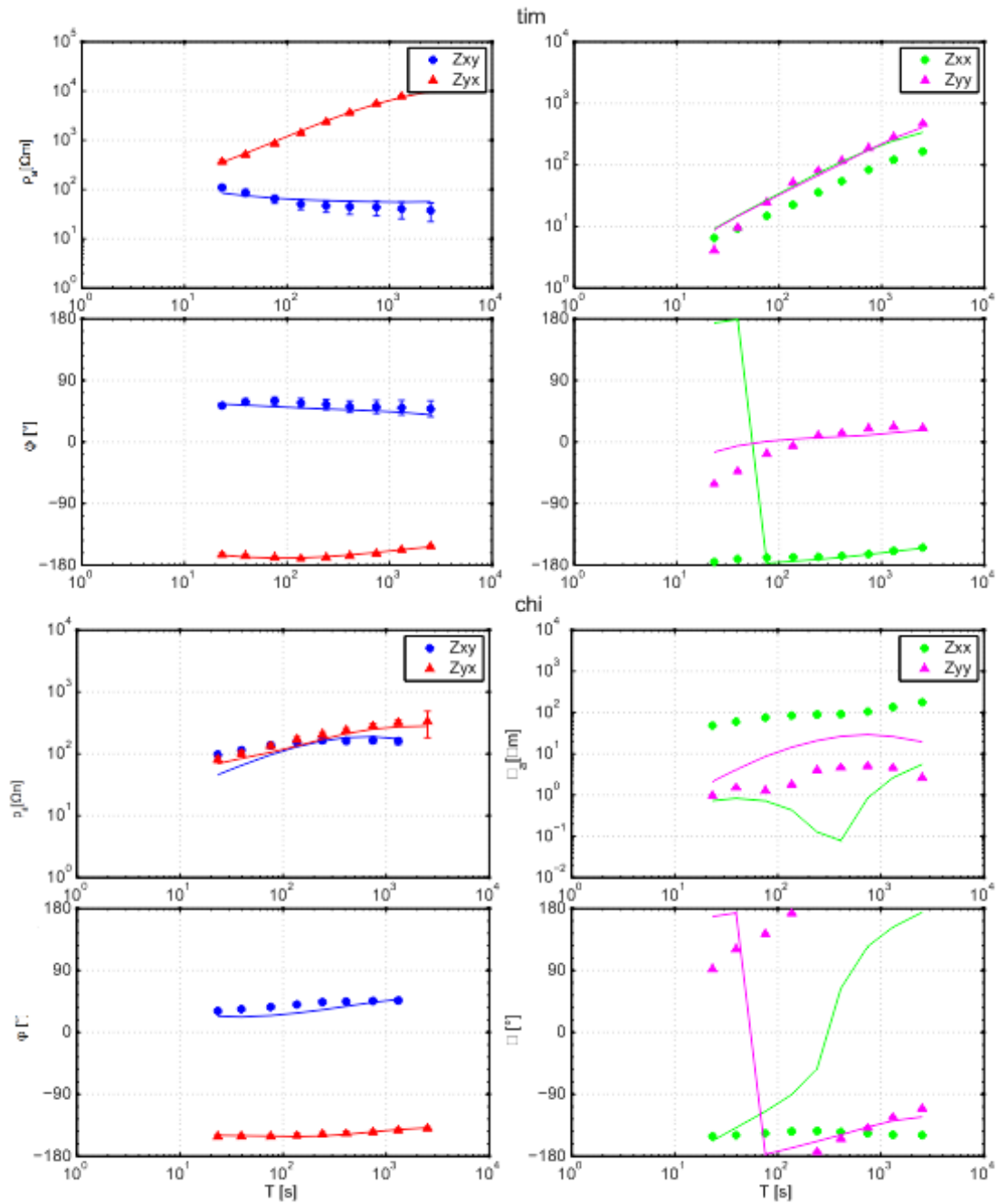
FIGURE 5.9: **Apparent resistivity and phase curve of the site TIM at the Coastal Cordillera and CHI in the Central Andes with error bars.** Blue and red curves are the off-diagonal and the main diagonal is presented in pink and green from the impedance tensor Z.
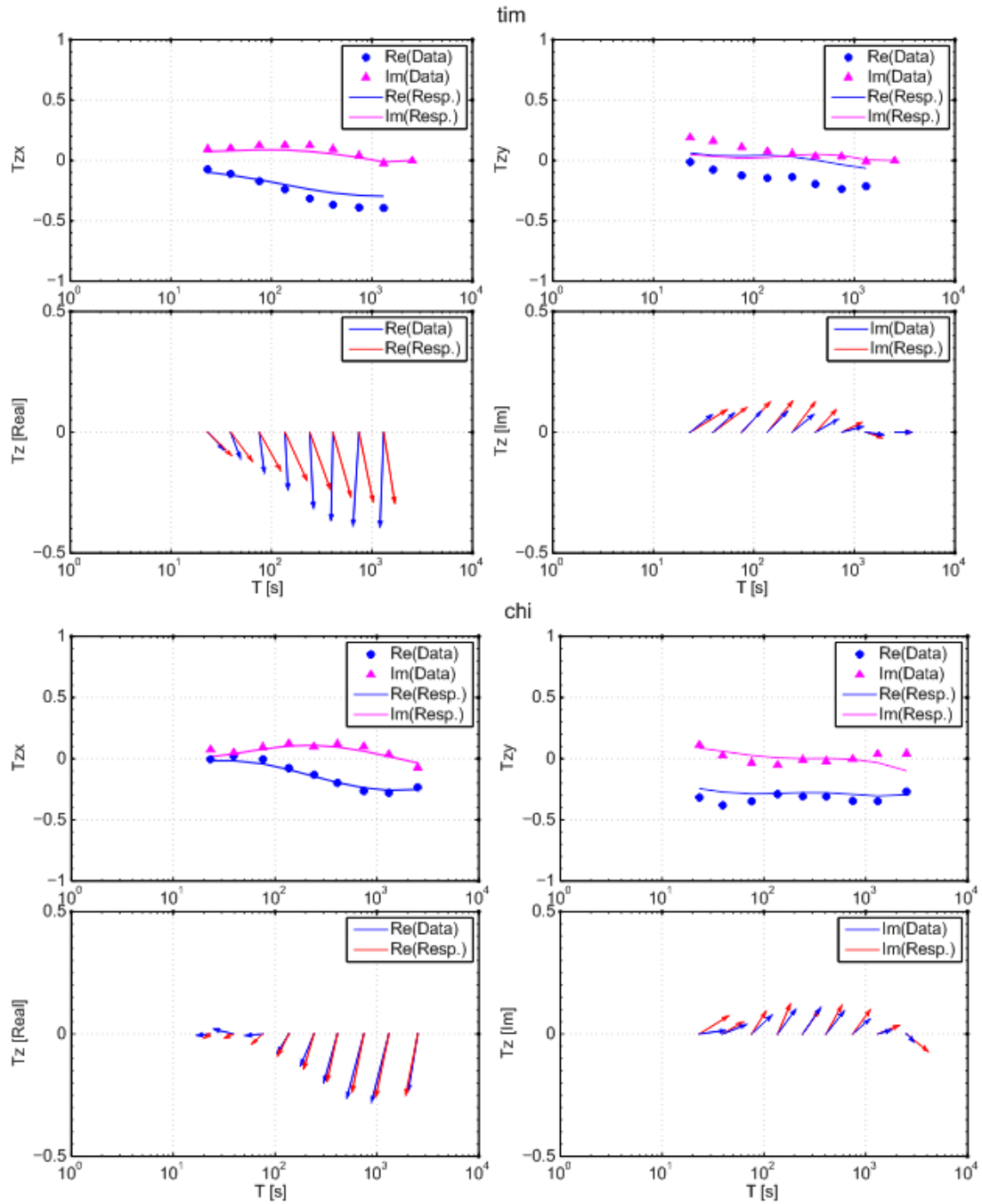
FIGURE 5.10: **Vertical transfer functions and behavior of real/imaginary arrows after Wiese.** The fit is qualitatively okay as the main characteristics of the arrows are reproduced. But it is not as good as in the impedance. The real and imaginary arrows run anti-parallel but not yet in an angle of $\neq 180°$. The fit for site CHI is noticeable better as the coastal effect remains negligible.

5.5   Comparison of the 2-D and 3-D models

The recent results of the 3-D model generally confirm the main features of the 2-D model of Brasse and Eydam (2008). The 2-D model of Eydam (2008) holds a lot of features that could be explained in a 2-D environment, however some had required a 3-D environment approach. One of the main advantages of a 3-D study is the insight in complex structures. In a 2-D study one only obtains a simple cut along the profile line which works well as long as the geological trends run parallel to each other. However, in the Bolivian Orocline the trends start to bend into E-W direction (Allmendinger et al., 2005).

The Pacific Ocean is a problem, even for a 3-D study as it influences near-coastal stations badly due to the low resistivity of salt water. Furthermore anisotropy of the crust in the Coastal Cordillera complicates simple underground analysis (Galindo, 2010). This was already shown by the induction vectors analysis in the 2-D study. Phase tensors of this study confirm the complexity of the underground in the Coastal Cordillera and Longitudinal Valley. However both studies found highly resistive material below the ocean ranging deep in the Moho. They even exist in the CC and LV and maybe in the Western Cordillera Escarpment.

The most prominent feature is the good conductor beneath the Altiplano (see Figure 5.11). In a depth of 70 km - 120 km it is resolved by the MT measurements. At larger depths only assumptions can be made since the penetrations depth is not sufficient enough. This was observed in the 2-D and 3-D model. A sensitivity study of the body lead to an assumption of a complex 3-D shaped body in the Altiplano that follows the geological trend of the Andes. Obviously this is something a 2-D model can not display. At shallower depths, the 2-D model found sedimentary layers of the Tertiary with thickness up to 10 km. The 3-D model showed several layers in the Western Cordillera and Altiplano. Even in the Eastern Cordillera such features were observable. Thus, they remain uncertain since the calculation runs on two - three sites and is therefore not convincing enough. Beneath larger volcanoes there was no conductive feature observed, such as a magma chamber, that could be related to them.
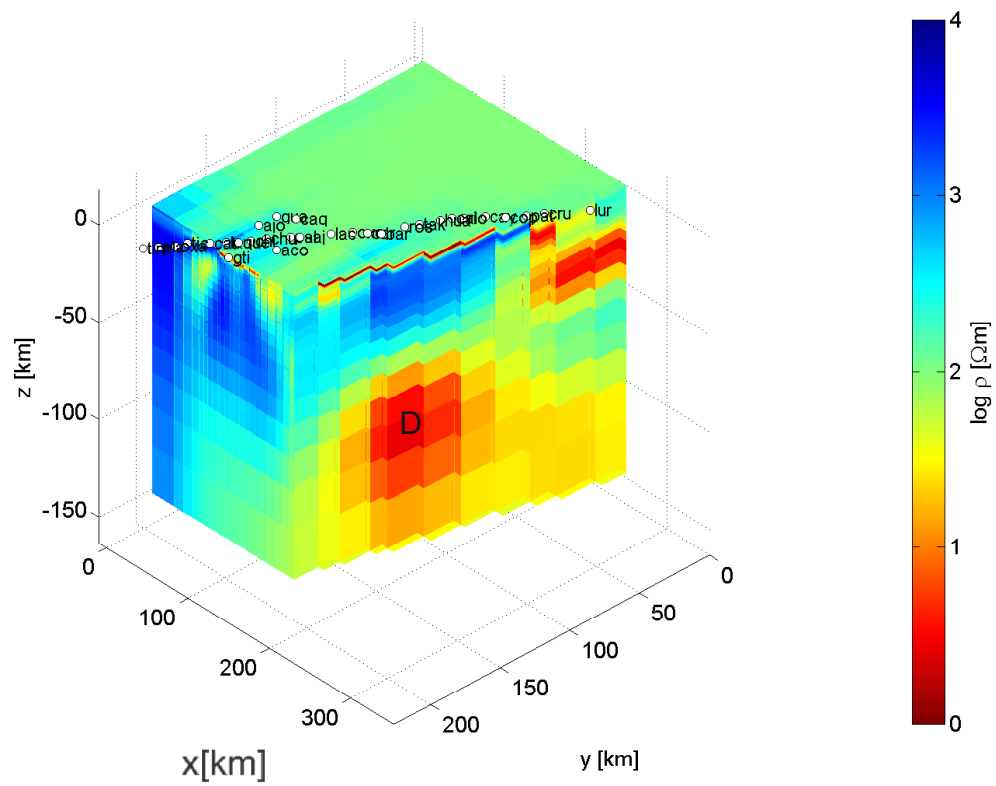
FIGURE 5.11: **3-D inverse model along the profile line in the Bolivian Oro-cline.** The most prominent feature (D) is located at a depth of 70 - 120 km beneath the Central Altiplano.

Chapter 6

Magnetotellurics at Parinacota and Taapaca volcanoes

In autumn 2007, an MT survey was carried out around the two stratovolcanoes Taapaca (5,860 m) and Parinacota (6,348 m) in the Central Andes at 18°S. Both stratovolcanoes, a synonym for a layered volcano, are located in the Atacama desert between the Chile and Bolivia border. The campaign was a collective venture of the research project 'Investigation of Magma Reservoirs under Stratovolcanoes of the Central Andes' of the FU Berlin Institute Geophysics, the Leibniz University Hannover Institute Mineralogy and the Georg-August University Göttingen Institute for Geochemistry. The measurements were made in a circle-shaped layer around both volcanoes to observe complex 3-D structured behavior in the subsurface.

The Taapaca volcanic complex consists of an initial andesitic stratovolcano and a long-term dacitic lava-dome complex. It has a volume of approximately 35 km^3 (Wörner et al., 2000). Its last known eruption was about 350 BCE (Clavero et al., 2004). It is overlain by Pleistocene ignimbrite deposits from the last 1.5 Ma years which form the typical volcanic cone with an E-W trend. In general it migrated to S-W in the past which is divided into four principal stages of time:

1) Due to missing analysis of isotopes it is not completely certain when the history of Taapaca volcano began. About 1.5 Ma ago two silistic-andesitic lava flows erupted in N-S direction at an expansion of about six km.

2) That stage of the volcano partially overlays the main events of stage one and is probably located at a time around 1.5 - 0.5 Ma ago. Dacitic lava flows cover an area of about $150 km^2$ and consist of lava, cones, ash flows and lahars.

3) 0.5 - 0.47 Ma ago similar streams and flows like in phase three create the central part of the volcano complex and parts of the southern and western wing. The current trend is in N-S direction.

4) From 0.45 Ma till today the complex has been formed as it is known nowadays. Typical debris and ash flows, landslides, eruptions and pyroclastic flows have been produced in the area around the dacitic cone. They are mainly orientated on the southern and southwest side.

The definition of volcano Parinacota is difficult as there are several studies about its historic development. As a part of a longer lasting process, an almost perfect cone shaped summit crater with about 300 m diameter (Francis, 1988) has been dated back to the late Quaternary. This study is mainly based on Wörner et al. (1988). Parinacota is divided into six historical geologic phases:

- **1)** About 163 - 116 ka years ago andesitic, rhyolithic and dacitic cones, debris and ashflows have been produced in the area. They build the basis of the current volcano complex, which consists mainly of andesit material. It can be found on the northwestern front of the complex as deposition of bygone times (Clavero et al., 2004).

- **2)** In a time about 47 - 40 ka years ago rhydacitic and ryholitic material starts to create a plateau.

- **3)** Until finally about 52 - 20 ka years ago the old cone was created by older uplifted material from depth.

- **4)** Suddenly between 20 - 10 ka the old cone is destroyed by a collapse of the whole construction. The material starts to slip off on the western front.

- **5)** At about 10 to 3 ka, so called Ajata-Flows were created, consisting of basaltic-andesitic material on the southern front .

- **6)** From 8 ka to nowadays a new cone was formed on Parinacota by new eruptions. This is the top of the current volcano edifice

Stratovolcanoes are a result of the long lasting subduction process of the Nazca plate in the Central Volcanic Zone. Subducted material from the mantle, melts in the subsurface and is transported as loose earth and lava flows to the top of the volcanoes where it creates new layers. The pointed shape cone structure is typical for volcanoes in this area (Siebert et al., 1981). The actual approach was to find magma chambers beneath

the volcanoes and their orientation in the underground. Magma chambers consist of partial melts and are known as very good conductors compared to their surrounding environment. They are assumed to be in close-to-surface depths and can be resoluted by the AMT procedure. This method uses short periods and takes less time to measure two electrical and three magnetic field components compared to other MT methods.

The network of sites was placed in 3-D circle around both volcanoes as shown in Figure
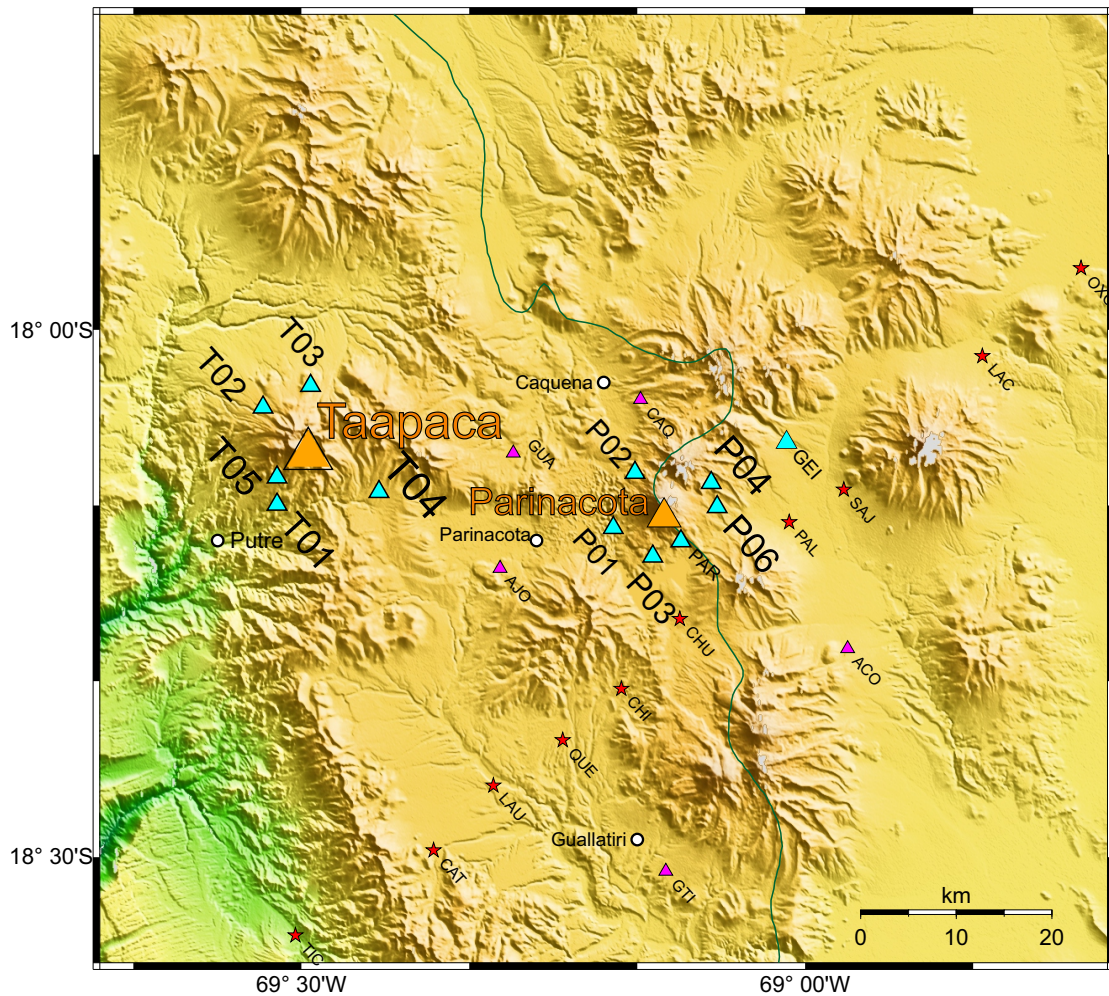
FIGURE 6.1: **Overview at** $18°$**S of the study area.** Cyan markers indicate AMT sites around the volcanoes. LMT stations are colored pink. For orientation red stars show the sites of the transect from Chapter 5.

6.1, with five AMT stations for Taapaca (T01 - T05) and seven for Parinacota (P01 - P06 and PAR + GEI). It has to be said that the local geography and infrastructure does not allow a more complicated network, since the volcanoes are raising in height rapidly and there are no accessible paths, such as streets. Additionally, a network of extra LMT stations (AJO, GUA, CAQ, ACO, GTI) was added around volcano Parinacota at a longer distance.

Previous MT studies on this volcanoes could not resolve a good conductor, such as

a magma chamber in the subsurface. New fully automatic inversion and numerical concepts are used in this study to retrieve information about the subsurface of both volcanoes. The following chapter is a reinterpretation with new promising possibilities to solve such general problems.

6.1 Previous work

In 2001, the idea to interpret volcanoes in a 3-D approach, based on MT data, was born by Spichak (2001). His basic idea was to test the components of the electromagnetic field and their transformation in comparison to their sensitivity towards the 3-D electrical conductivity in and below volcanoes. He developed a software (FDM3D) to model symmetric volcanoes based on a marine shield volcano. This approach suffered under the coastal effects however (Spichak, 2001).

In 2004, a new 3-D study with the idea of 3-D modeling with topography was published by Müller and Haak (2004) on volcano Merapi in Indonesia. They used 1-D inversion approaches wherever it was possible and added them to a 3-D model. This lead to a Pseudo-1D-character, which was used to adjust the induction arrows. They concluded a three dimensional conductivity anomaly beneath the volcanoes, which they interpreted as saline fluids.

Later in 2007 Franke et al. (2007) used a first real 2-D and 3-D finite element method to model the structure of volcano Stromobli in Italy. The results were satisfying. Heise et al. (2008) performed a 3-D forward calculation and a 3-D inversion with the impedance on the Taupo Volcanic Zone in New Zealand. Their results contained a poor resolution of the underground in a depth of 2.5 km. The authors explained that a strong 3-D environment can not be resolved at this time by conventional MT methods, however they saw potential for the method in the future. Based on these experiences and ideas, a former FU student, Dirk Brändlein, performed a MT study in his diploma thesis about the volcanoes Taapaca and Parinacota. His thesis contained a forward study on magma chambers in the Central Volcanic Zone. As a first analysis the dimensionality (Brändlein, 2009) of the data was screened by the skew after Swift (Simpson and Bahr, 2005). An image of the calculation is added to the Appendix B.1. At 0.1 to 10s an increase of the Swift's skew is observable, meaning the longer the periods, the more 3-D are the data. Whereas, after Bahr the same station shows a similar behavior at earlier periods already. It loses its maximum and decreases. Dirk Brändlein concluded that 3-D dimensional analysis would be necessary at a period range larger than 1 s. With Equation 3.17, he estimated a depth of about 16 km for a 3-D anomaly such as a magma chamber.

In Figure 6.2, the phase ellipses of both volcano sites are displayed. Taapaca, the western one, does show earlier an increase of the angle β compared to Parinacota.
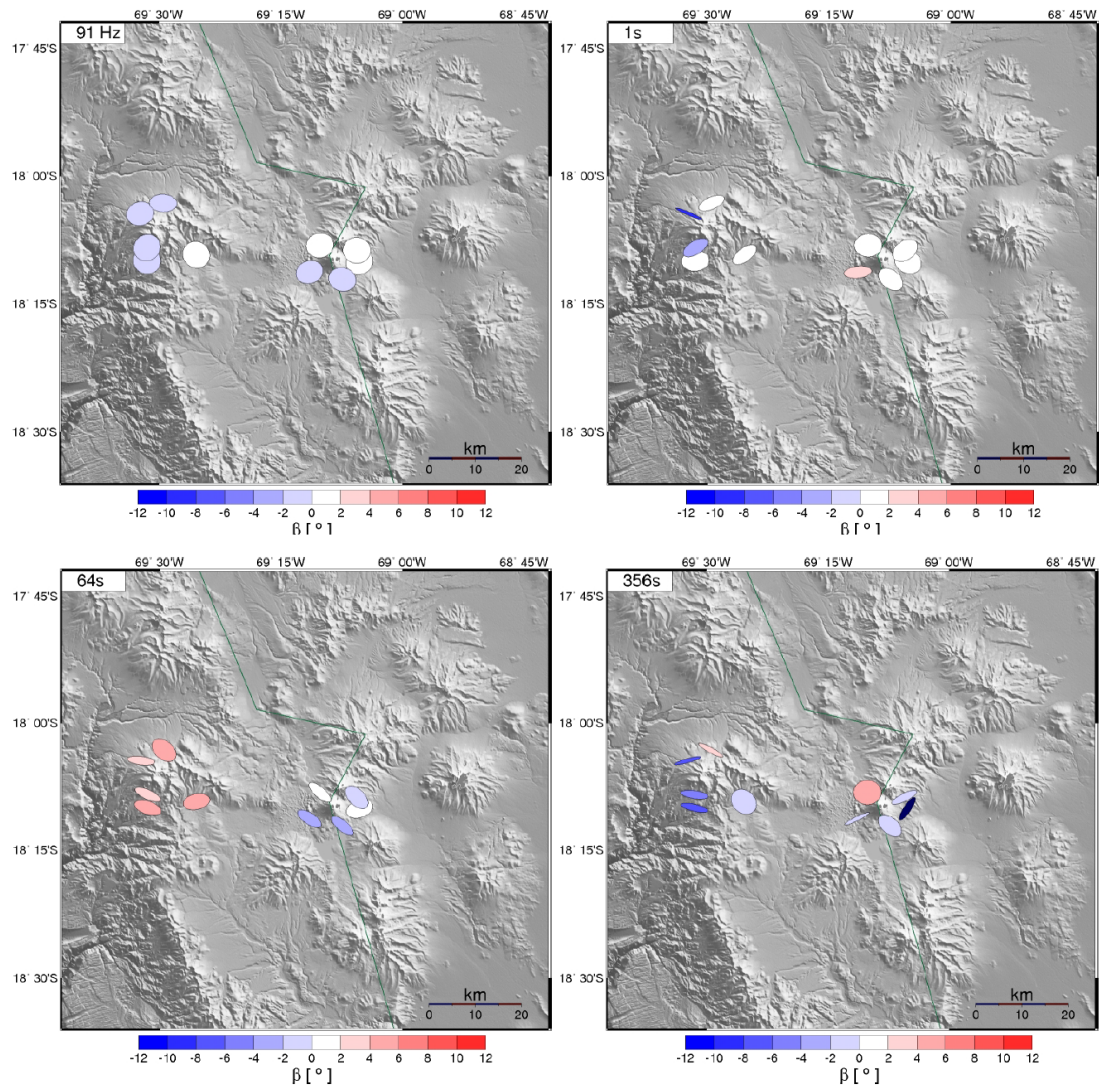
FIGURE 6.2: **Phaseellipseplot around Taapaca and Parinacota.** Period ranges from top left: 91 Hz, 1s, 64s, 356s. The skew angle *beta* ranges from -12 to 12. Note the length of the axis at Taapaca site at long periods.

At a periods of approximately 1s and larger, one can observe a change of dimensionality on both volcanoes. The axes are parallel orientated in a E-W direction. This analysis of the dimensionality is consistent with Swift's analysis. As a final approach the method of plotting induction vectors was used to verify the orientation of the conductive feature. In Figure 6.3, one can observe that the arrows point away from the volcanoes. The induction vectors have been plotted after the Wiese convention (Wiese, 1962). At Mt. Taapaca, the long periods show a typical topographic effect as they start to wave. Owing their structure, both volcanoes have a large volume and surface. This results in a lot of space for the electrical strikes in the subsurface which influences the flow of the streams and therefore the data. In MT, it is observable in the data since mountains seem to be more conductive compared to their resistive valleys (Eydam, 2008). This effect is not observable at Parinacota volcano, as the real induction vectors do not show such a behavior. Here, the induction vectors might be influenced by a good conductor in the upper mantle in the backarc. Another hint for this assumption is the behavior of even longer periods, as the far away conductor becomes more and more important at the data. Site P01 seems to be influenced by superimposed conductive features as the arrows point southward. Induction vectors of LMT data carry on the behavior of the AMT stations as they become very long and turn into W-S-W. An image of the LMT induction vectors has been added to the Appendix B.2.

Brändlein used for his study on the influence of topography the MT3FWD-Code of Mackie et al. (1994) as part of the WinGLink software package. His work included topography studies and conductive features and their dimensionality. However he was limited in his work as the computer power, numerical algorithms and inversion programs did not allow 3-D inversions, so he was forced to use a forward modeling only. He assumed several layers in the volcano with different resistivity but could not confirm a good conductor, such as a possible magma chamber.

6.2 Data acquisition and processing

The AMT measurements were made with two data logger ADU-06 (Analog Digital Unit), with the sensor being directly connected to the logger, of the FU Berlin and TU Berlin. On the AMT sites, 34 periods were measured between a frequency range between 250 Hz and 350 s. As mentioned previously every second period was removed to achieve 4 periods per decade ending up with 17 periods. This step was necessary to find a balance between calculation time and inversion result. The reader is referred to Brändlein (2008) if he is interested in more detail.

A study on the phase tensor ellipses has been done as well as on the induction vector.
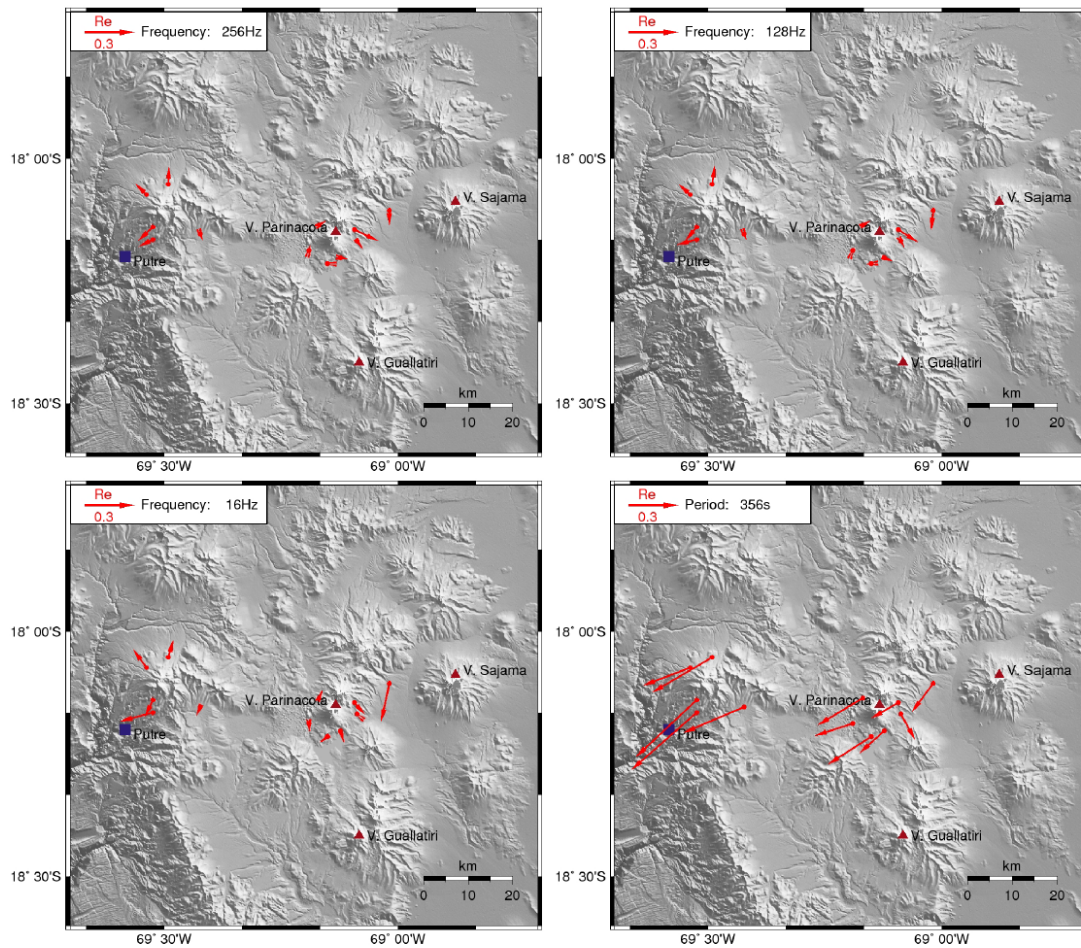
FIGURE 6.3: **Induction vectors around the stratovolcanoes Taapaca and Parinacota for AMT sites.** Period ranges from top left: 91 Hz, 1s, 64s, 356s. Induction vectors (Wiese, 1962) are pointing away from the volcanoes at lower period ranges up to 356 s. At large periods they coherently point towards S-W direction.

Since both studies are accord with the work of Brändlein only a exemplary Figure 6.4 at 18 Hz is shown and the rest has been added to the Appendix B.3. The induction vectors start to grow and point away from Taapaca. As one can see, the ellipses are also starting to get more ellipsoid (compare 6.2). One can agree of a certain conductive feature beneath those volcanoes. The remaining question is if this study is able to find something that could be a possible magma chamber?

One of the main problems of the study was the poor data quality of some LMT sites. They contained a lot of scattered data, especially at longer periods. All induction vectors start to run parallel into S-W direction at long periods. This might influence the inversion of data for shallow depths, such as a magma chamber. First inversion attempts in this thesis could not find a good fit for long-period data and so it was decided to remove LMT sites from this study.
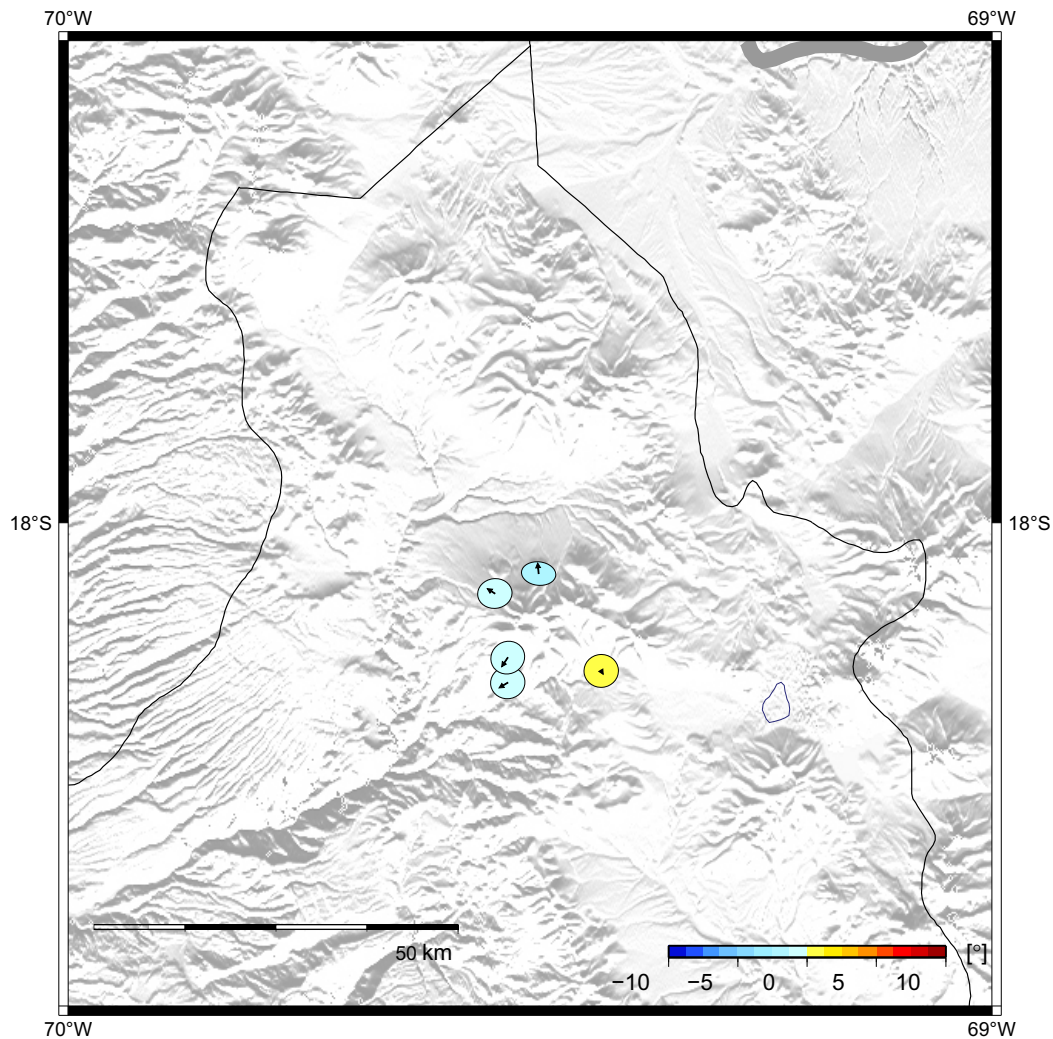
FIGURE 6.4: **Phase tensor ellipses of volcano Taapaca.** Period: 18 Hz. Phase ellipses are almost circles. However their axes start to become longer so they become ellipsoid. The induction vectors are rather short and point away from the volcano. This could be due to a topographic effect or a conductive feature in the underground.

- **1)** The induction vectors hinted an influence of a conductor in the backarc (Chapter 5) at long periods. It was also observed in early modeling results, as strange conductive features appeared as boundary effects or artifacts. When removing the questionable sites, those effects started to become less important or disappeared.

- **2)** Some stations had poor data sets, such as non-physical explainable phases or scattered data in general. It was necessary to remove so much data from certain stations, that the remaining frequencies would not have been trustworthy enough to show a reasonable impact. Finally, 5 sites were used for the AMT study.

- **3)** Since the long and short period data had two different data ranges it would have been required to interpolate. This attempt did corrupt the data in a bad way and it was difficult to find a way to interpolate and run trustworthy inversions with the data as the inversion stopped randomly.

Unfortunately, quality of long-period data around the two-volcanoes was insufficient. I, thus concentrate on analysis of shorter period data (until T = 100 s), which proved to be sufficient for the resolution of upper-crustal conductive features beneath the volcano edifices. The method AMT covers the period range for such a study perfectly.

6.3   Taapaca Volcano

In South America in Chile, close to the city Putre (NE about 10 km) the mountain complex Nevados de Putre is located. The volcano complex is named Taapaca with a very high altitude of 5,860 meters at 18°S and 69°W (Clavero et al., 2004).

6.3.1   3-D Model

Volcano Taapaca holds a lot of problems in the first place. The foremost model included no topography, no ocean and every AMT but no LMT station. They were not required since the distance was so huge that even for LMT station their influence would be negligible. In Figure 6.5 the first and the final starting model are illustrated. The first model comprises a total length of 800 km in x-direction, 800 km in y-direction and about 900 km in z-direction. It was a simple cuboid model with a homogeneous half-space of 100 Ωm as background resistivity. A first trustworthy inverse model had a rather poor RMS of 3.08 after 129 iteration. Every new initial model included new added features. Then Topography was added from SRTM data observed as the first model results showed problems in the fit at typical periods for topographic effects. The ocean was not included since AMT data do not have the range to get affected by the Pacific Ocean. As the computational costs depend critically on grid size, the model was reduced to the following parameter: x = 700 km, y = 700 km and z = 500 km. This proved to be sufficient for not producing artifacts due to boundary effects.

The first promising inverse models included impedance and tipper with an RMS of 2.52 after 66 iterations. It was decided to begin again, but with a more fine discretized model. The cells were edited, so a very fine mesh was created with sizes of a cell that only demonstrate a few tens of kilometers. In another approach, the function 'center stations' was tested and lead to an RMS of 2.10 after 74 iterations. That option moves a station into the middle of a cell, in the hope to solve the adjustment problems at long periods for the AMT sites. However, this did not fix the problem and was discarded since it corrupted the files. The final initial model contained Nx = 62, Ny = 71, Nz = 41 cells, with an error floor set at 10% and the main diagonal elements being removed from the calculation as they had mostly scattered data. After 109 iteration an RMS of
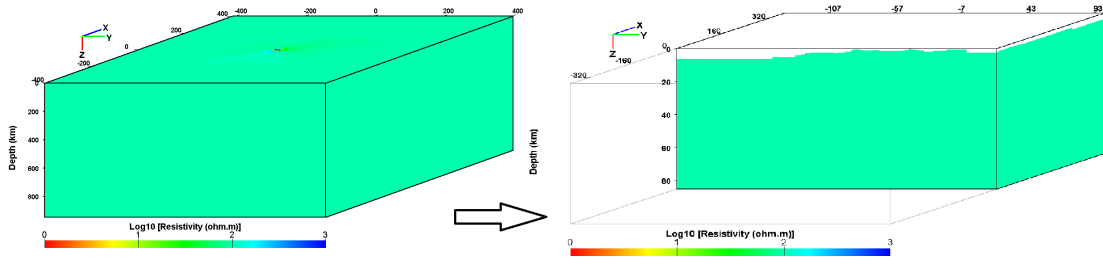
FIGURE 6.5: **First and final initial model containing impedance and tipper to show the effect of topography added.** The starting model has a x,y,z-length $800 \cdot 800 \cdot 900$. There is no ocean included. On the right side, the final initial model with topography included and a homogeneous half-space of $100 \, \Omega m$. This is a cut into the profile.

1.049 was achieved with a rather promising model (Figure 6.6). The whole model shows a conductive layer beneath the Taapaca edifice. Furthermore a second good conductor is displayed next to the mountain. The illustrated view is a cut into the earth showing the side extract of the volcano Taapaca from a certain point of view. The peak of the Taapaca complex is only assumable since the profile view starts about 5 km in front of the volcano. Air cells are dark blue. On top of the profile one can see the stations location.

- **A)** Feature A is a prominent and important feature of this study. In a depth of approximately six to seven km beneath the peak of volcano Taapaca the conductive feature appears almost like a layer.

- **B) + C)** Both features are of high resistivity about $1000 \, \Omega m$ and more. It is questionable, if that feature does really exist, since it could also be explained by the andecitic or dacitic structures.

- **D)** Feature D is a large low resistive feature in the west of Taapaca. It may belong to the Larancagua volcano.
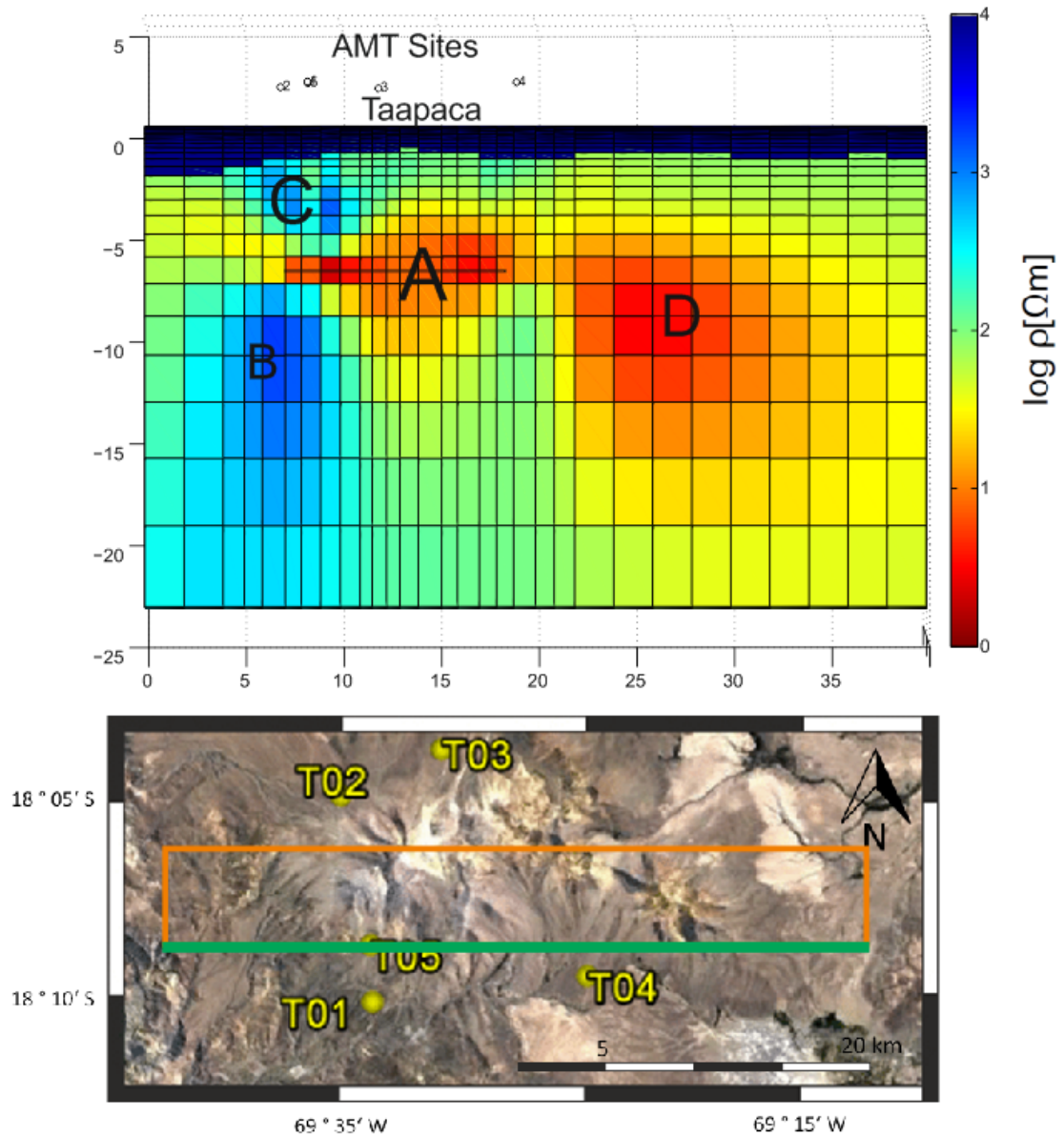
FIGURE 6.6: **Final inversion model of volcano Taapaca.** Important feature (A) may indicate the magma chamber of volcano Taapaca in a depth of 6-8 kilometer, as a possible good conductor is found. The topography of the area is observable, as the air is illustrated in dark blue cells and separates from the conductive features of the subsurface. Two resistive feature are resolved at (B) and (C). Feature (D) remains uncertain and requires a sensitivity test to confirm its existence. Satellite image taken from Google Earth shows the area of the profile with stations. The orange line illustrates the array of the inversion model cut. It is a result of the cell size of the initial model. Green line illustrates the profile shown.

The apparent resistivity and phase curves show a small trend in resistivity changes. At period length $10^0 - 10^1$ the fit becomes worse. It was observable at every site at Taapaca and seemed to be a problem caused by topography. At longer periods the data quality became worse and had to be removed eventually. A previous assumption was that the cells had not been correctly discretized and the inversion became corrupted. However, a better cell distribution did not lead to a better result. The misfit of data is especially observable in the T_{zy} and T_{zy} data in Figure 6.7.
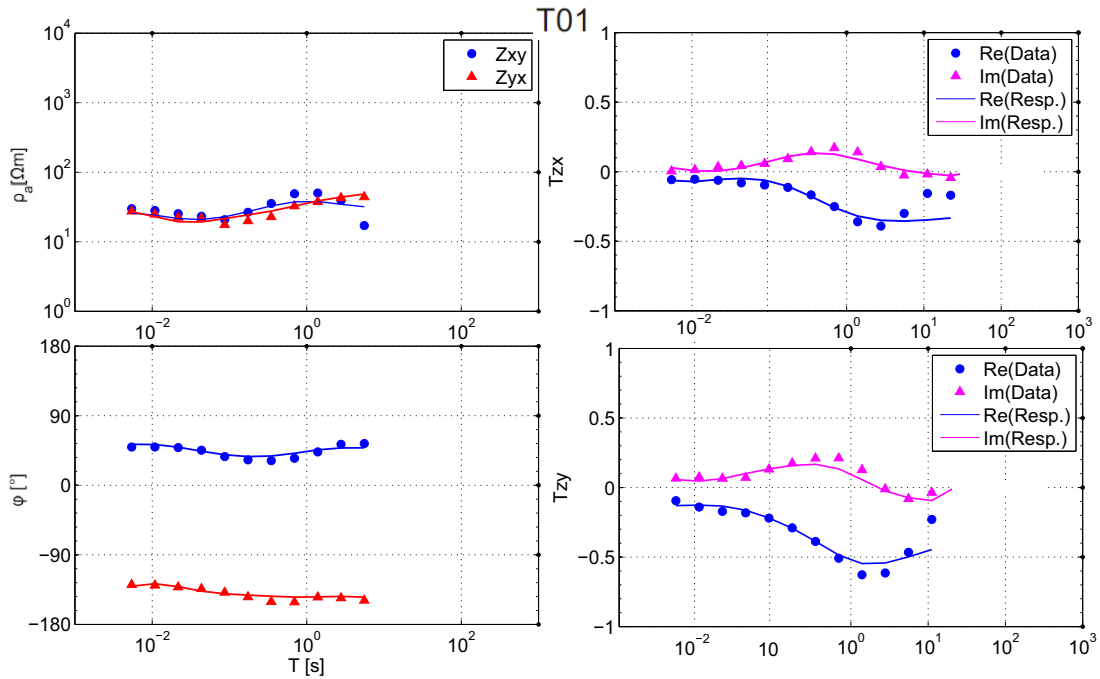
FIGURE 6.7: **Apparent resistivity and phase curves for off-diagonal impedances at site T01 and tipper function.** The AMT site shows fitting problems at 'longer' periods. Compare the green boxes. Apparent resistivity and vertical transfer function have been calculated really well, beside some small non-fits.

6.3.2 Sensitivity Studies

The conductive feature D in Figure 6.6 remains a problem that should be solved. The homogeneous half-space of the model at a depth of six km was set back completely to $100 \ \Omega m$ and recalculated. The goal is to see if those features appear again or disappear and to observe the behavior of the model response.

The main features (C), (B) and (D) appeared almost exactly again as they did in the regular inversion. The new inversion had an RMS of 1.4, which is a bit higher than it was before. The conductive feature (A), to be assumed as the magma chamber beneath volcano Taapaca, is occurring again. Yet, it does not remain as prominent as it was before, the sensitivity study can confirm the existence of such a structure in the underground. On the eastern part of (A) there is a small extension of the conductive feature to the surface. This may be an artifact of the inversion result, as the second conductive feature (D) is rather close. Figure 6.8 shows the sensitivity model. A cuboid with the background resistivity of $100 \ \Omega m$ as in the initial model was placed in a depth of 6 - 15 km to verify the existence of the estimated magmatic chamber beneath Taapaca.
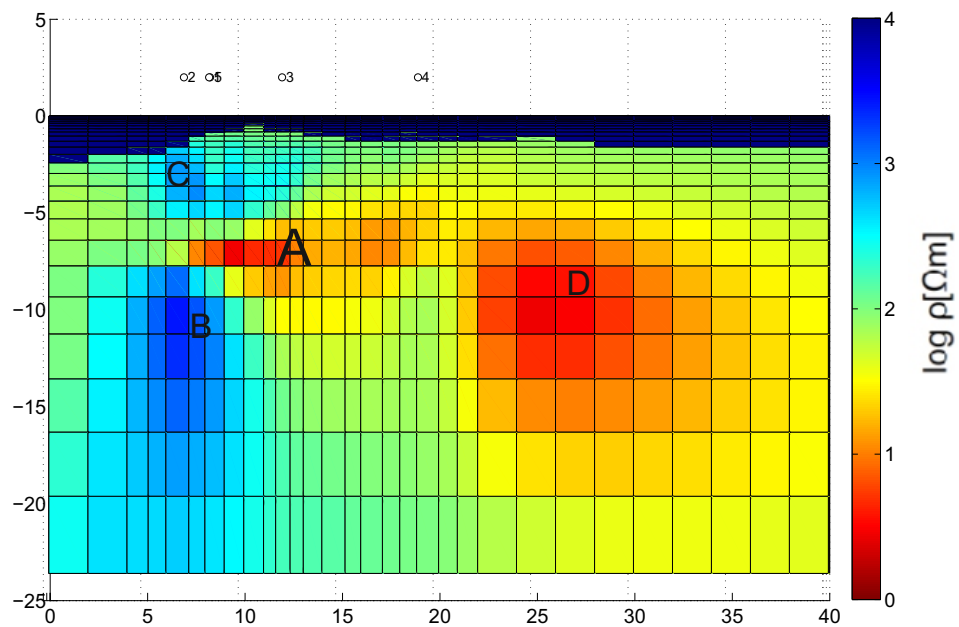
FIGURE 6.8: **Slice view on Taapaca. The slice coordinates are the same as in Figure 6.6.** This profile is located approximately 5 km south from the volcano peak. Features are to be found again, but they are not as significant as they were before.
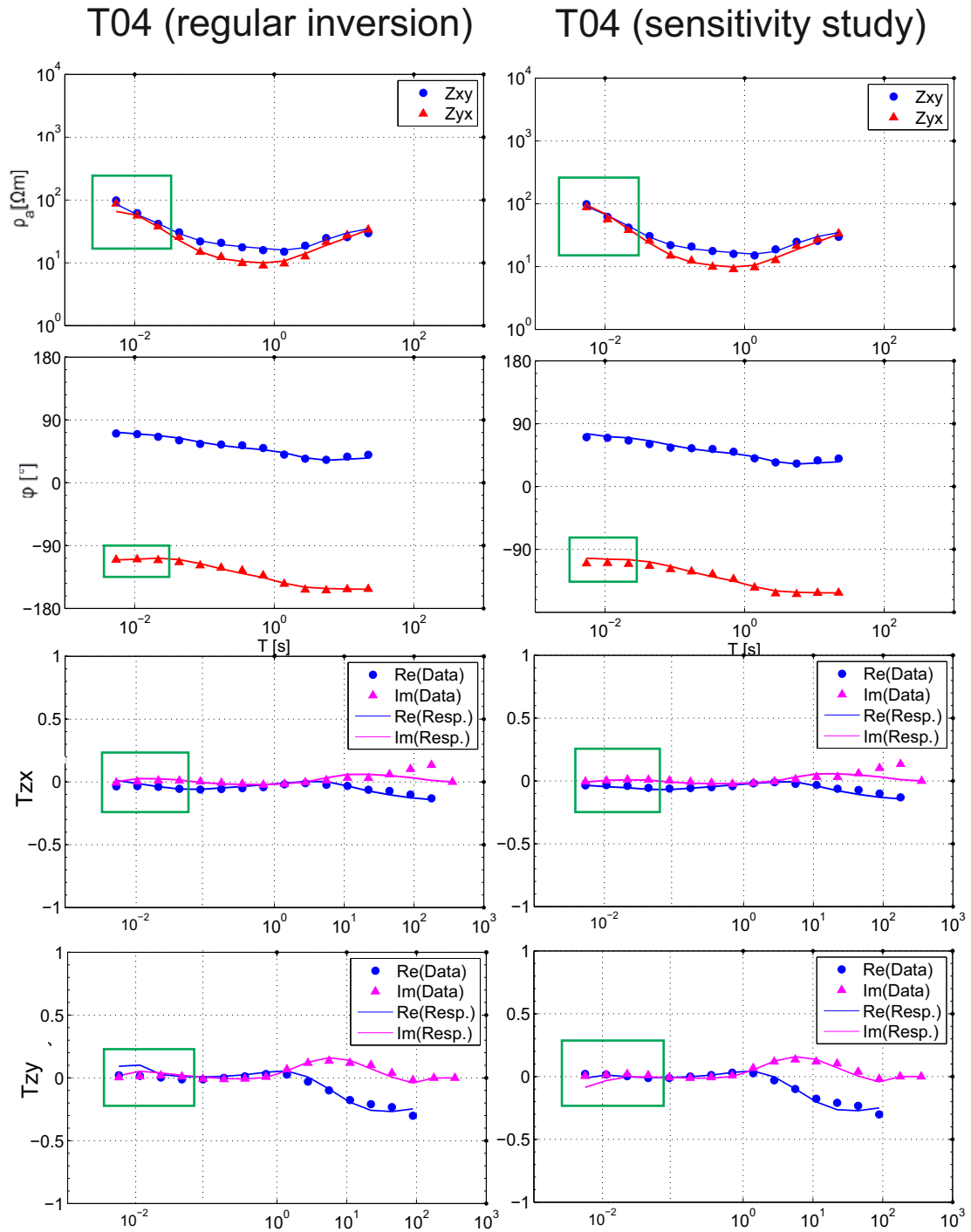
FIGURE 6.9: **Apparent resistivity, phase curves and tipper (T_{zx} and T_{zy}) are shown. The left side is the regular inversion, right side the sensitivity study.** Observable better fit at very short periods at 10^{-2} when performing a sensitivity study by resetting the model resistivity back to 100 Ωm. At longer periods (10^2) the tipper curves have a poor fit. This might be caused by a topographic effect.

The comparison of the transfer functions is emphasized in Figure 6.9, where the responses of site T04 are checked. In general, the fit for short periods at a period range around 10^{-2} improved. It is observable in the apparent resistivity, phase curves and tipper. In T_{zy} the fit of the imaginary curve is worse than it was in the regular inversion model. Although, the tipper had problems to find a solution for measured and calculated data at long periods (10^2) the whole inversion can be seen as successful. There are two possible explanations, connected with each other, for the poor fit. A topographic effect doesn't allow a good fit at long periods and gets influenced by a conductive feature located somewhere in the area around Taapaca. This may be caused by the anomaly D of the eastern Larancagua volcano.

6.4 Parinacota Volcano

The Parinacota volcano with its summit located directly on the Chile/Bolivia border - is the southern peak of the Nevados Payachata (Aymara for twin mountains), where the older Pomerape constitutes its northern neighbor. The stratovolcano has about 6,348 m height and a way more complex history than Taapaca.

6.4.1 3-D Model

The study of volcano Parinacota benefited from first experience in 3-D inversion models of Taapaca. However, the first approaches started in the same manner to cross-check if the approach used for Taapaca was correct. Thus, in the beginning, no topography, no ocean and every AMT and LMT station was added. The initial inversion was based on a grid with 800 km x-direction, 800 km y-direction and 800 km z-direction. Additional long-period sites GEI and PAR were used in this study, as they contained a bit different measurement, it was required to change the period range. 17 frequencies with 4 per decade were used. After removing poor data they were masked down to 12 frequencies. In the final model they got removed completely as they calculated another good conductive probably unrealistic feature about 20 km offset from the volcano cone. The first inversion model had an RMS of 1.72 with full impedance (main and off-diagonal) and the vertical transfer function included (there was no topography included which is a rather unrealistic initial model). Both were calculated with an error floor of 5 %. The Pacific Ocean, with its low resistive salt water was not taken into account since the period ranges used were too short to be influenced and show some effect on the inversion models. Therefore no ocean was added to the initial model. An observable poor fit at long-periods indicated a problem of the missing topography, so the first step was to add the topography. Now that the model had become more realistic compared to the

real world, the RMS increased severely with observable misfit in the data. By removing long-period data ($> 10^1$s) the model achieved an insufficient RMS of 2.74 after 51 iterations. The model has been added to the Appendix B.4. Using the experience gained from the inverse model of Taapaca in Chapter 6.3.2, the grid structure was improved significantly. Every inversion model was recalculated with the new mesh and feature (C) did not appear as strong as in the rough grid. The final model is illustrated in Figure 6.10.

This model had a total x,y,z-length of 800 $km \cdot$ 800 $km \cdot$ 900 km. The inversion run with full impedance and tipper and their error floor (5 %) was not changed, as the sites did not include too much scattered data after masking questionable periods.

In comparison to Model B.4, there is not too much of a change of the conductive resolution of the subsurface. The most prominent feature (A) in Figure 6.11 shows a conductive layer of about 1 Ωm at a depth of seven to ten km beneath the peak. It could be a possible magma chamber of the Parinacota/Pomerape complex. As the profile is located more south from the cone of Parinacota it may belong to it. The feature (C) remains uncertain but becomes less important, probably not even existing. However, the next chapter will perform a sensitivity study on this. Feature (B) is a more resistive feature above the good conductor with an estimated resistivity of 1000 Ωm. The inversion model 6.10 stopped after 143 iterations with an RMS = 1.43.

A remarkable difference in the RMS is observable when the cells of a grid mesh are optimized. It was not required to remove data to improve the fit of data in the calculation, as the mesh was constructed more subtle in the initial model. A fine grid led to a well fit at longer periods as it is illustrated in 6.11. The vertical transfer functions show the same behavior at longer periods approximately at 10^2s which could be the influence of another conductor or a topographic effect.
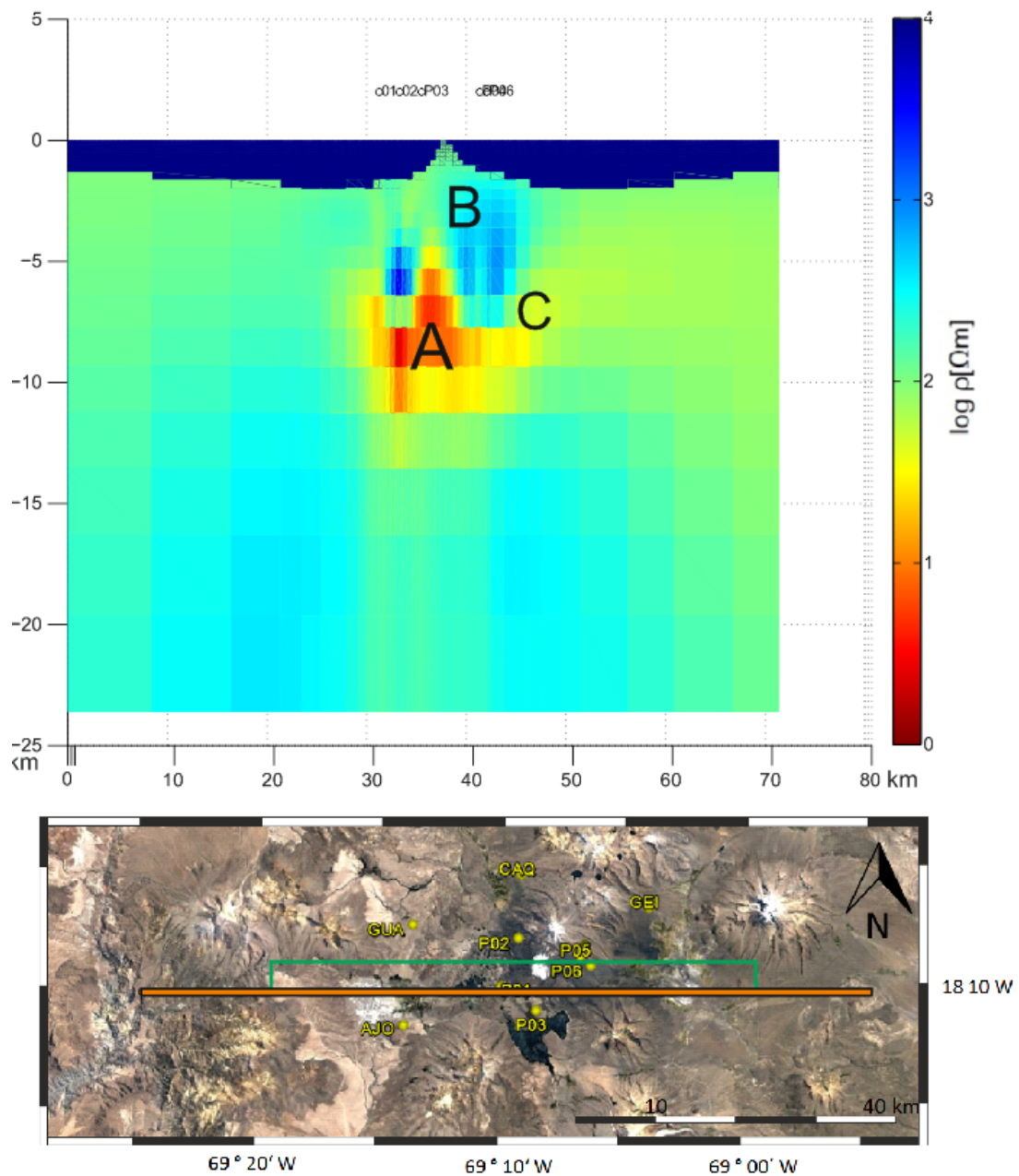
FIGURE 6.10: **Cross section of the profile at** $18°\ 10'S$ **of mountain Parinacota.** Well conductive feature (A) with an apparent resistivity of $1\ \Omega m$ beneath volcano Parinacota. There is another conductive feature (C) eastward of Parinacota. Higher resistivity structure (B) in the subsurface around the volcano complex. The orange line shows the cut of the profile displayed in the Appendix. The green array delimits the profile which illustrates in the image above.
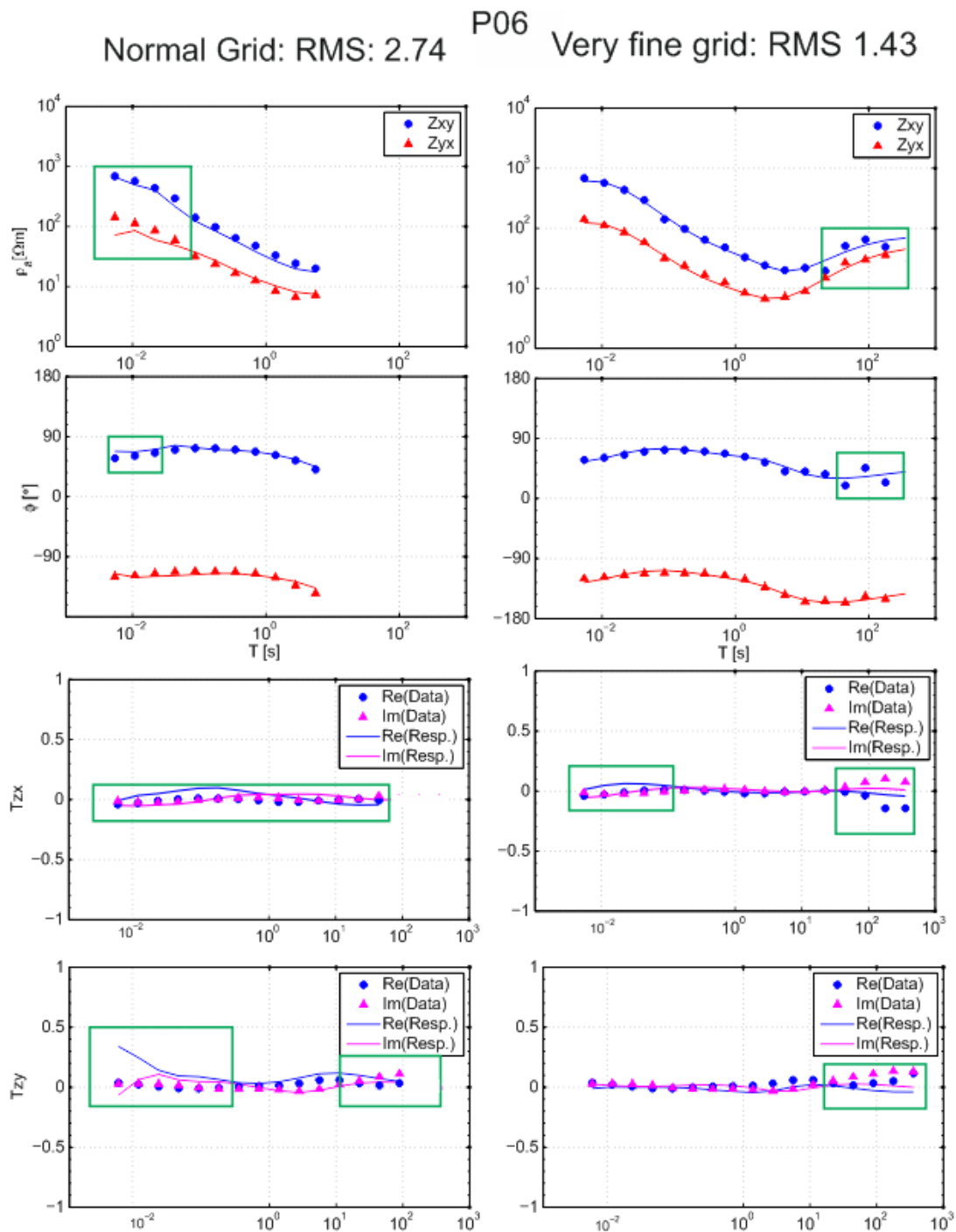
FIGURE 6.11: **Transfer functions of the normal model and the extra fine grid model on exemplary site P06.** There is a generally poor adjustment at short periods in the vertical transfer function. Apparent resistivity and phase are sufficient. The very fine gridded model shows an in general very good fit. Even in the apparent resistivity, where data points become more difficult and probably non-physical the fit is good, as it follows a trend. The transfer function shows again the behavior that indicates topographic influence. The difference in the long periods comes from interpolation, processing and masking.

6.4.2 Sensitivity Studies

In the sensitivity study, the very fine grid model has been used to verify the existence of the calculated features in the subsurface of Parinacota. The model parameter have not changed, but in a depth of six km a cuboid was added with a background resistivity of 100 Ωm, same as the homogeneous half-space of the initial model. After a few inversion iterations the feature (A) with an apparent resistivity of 1 Ωm appeared again. It confirms the conductive feature beneath volcano Parinacota in a depth of seven to nine km beneath the peak. In Figure 6.12, the result of the model after 66 iterations with an RMS = 1.34 is illustrated.

The area beneath the very good conductive layer in a depth of 12 km was high resistive in the regular inversion models. This formation disappeared almost completely now as it has not been calculated in the model result.
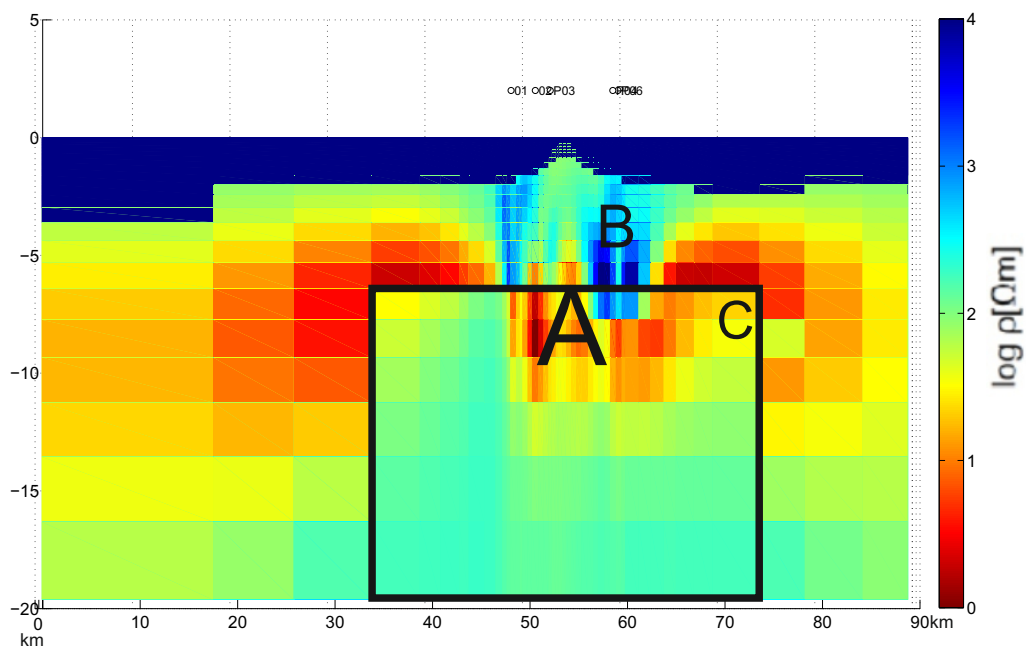
FIGURE 6.12: **Sensitivity study by full inversion on mountain Parinacota.** The black box indicates the area that was given a background area of 100 Ωm. The very conductive layer (A) that is supposed to be a magma chamber appears again. Highly resistive feature (B) above the feature (A). Feature (C) is visible again. The effects outside of the box are discarded as they are interpreted as artifacts.

The off-diagonal of the impedance and the tipper have been included in the sensitivity study. The fit of the measured and calculated frequencies is almost the same. At long periods in Figure 6.13, where the topographic affect is influencing the vertical transfer

function, an improvement of the fit is visible. The green boxes emphasize the problematic fitting.
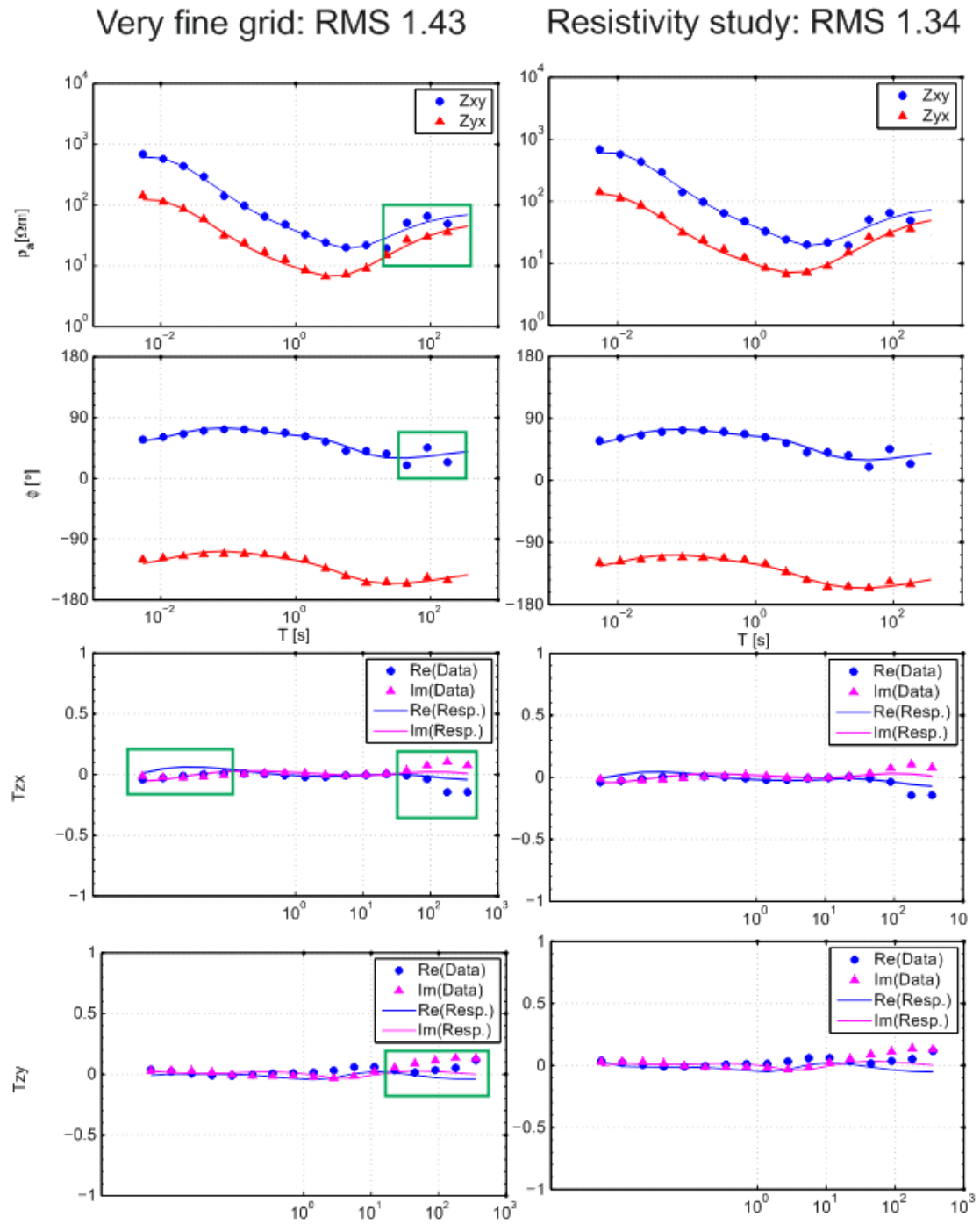
FIGURE 6.13: **Apparent resistivity and phase curve of station P04 for final the inversion model and the sensitivity study.** There is still a non-fixable misfit at long periods. The fitting is similar on both inversion models.

6.5 A geochemical perspective

As mentioned in a previous chapter, this study was a venture of the FU Berlin together with other universities. There have been other geological methods used on both volcanoes that will be discussed in this chapter to compare the MT results with other studies. The AMT measurements could confirm very low conductive layers of approximately 1 Ωm or less beneath both volcanoes. They are assumed to be magmatic chambers of their respective complex. The results will be compared to the geochemical approaches, which are based on the PhD thesis of Banaszak in Göttingen (2014) and personal communication with the working group.

The study was mainly based on the magmatic differentiation processes that comprise magma generation, intracrustal ascent and storage. A lot of surveys of statistical, geochemical and petrological kind were carried out in cooperation with the FR Petrology of the University of Hannover lead by François Holtz. An important fact of the work was the use of the geothermo-oxy-barometry (GTOB), which was used on a rock samples of dacitic composition from volcano Taapaca and a basaltic andesite from Parinacota. Experimental amphibole compositions should allow an application of appropriate GTOB methods.

A thin section of the probe gets analysed by an electrobeam-microprobe. They measure the ratio of oxids and the number of cations to calculate their position in the crystal structure of the amphibole. On volcano Taapaca certain trace elements have been found that are also present at volcano Parinacota as single flank eruptions. They are recognized as parental magmas recorded in plagioclase zoning found in Parinacota lavas. The overlying rocks of both volcanoes have a similar composition of amphibole and plagioclase chemistry (Wörner et al., 2007). Since a PVA (Polytopic Vector Analysis) study would be required to perform a reliable study on the fractionation of the lava, Banaszak focused only on the olivine from the most mafic lavas of Parinacota and compared them to the end-member of the olivine Taapaca-rocks.

The PVA is a multivariate statistical technique developed to analyze mixed species in geological systems. It is based on Q-mode factor analysis and PCA (Principal Component Anaylsis). This methods are used in geochemistry and petrology to understand the comprehensive whole rock into a model where every sample is viewed as a mixture of a possibly small number of potential end-members. The algorithms are based on numerous modules and can be read in Klovan & Imbrie (1971) if the reader is interested in more detail.

Based on the results of the RDEM end-member study of Taapaca dacites, the rhyodacite reservoir is estimated in the shallow crust in a depth of 7-10 km. The GTOB study however used a high crystallization pressure of 250-300 MPa for the rhyodacit reservoir and assumed that the pressure corresponds to a 9.4 to 11.3 km depth. The maximal depth

is probably presenting the lower limit of the silicic magma reservoir here (see Appendix B.5).

Parinacota was analysed the same way and hinted a depth of four to eleven km on the pressure results obtained from Mg-Hbl (1-3kbar). As well as volcano Taapaca, the mafic magma underplates the silicic reservoir and crystallizes compelled to this depth. The mafic magmas are not captured by the silicic magmas, so they can crystallize continuously until they reach shallower depths. A cartoon of the estimated system from Banaszak is illustrated in Figure 6.14.
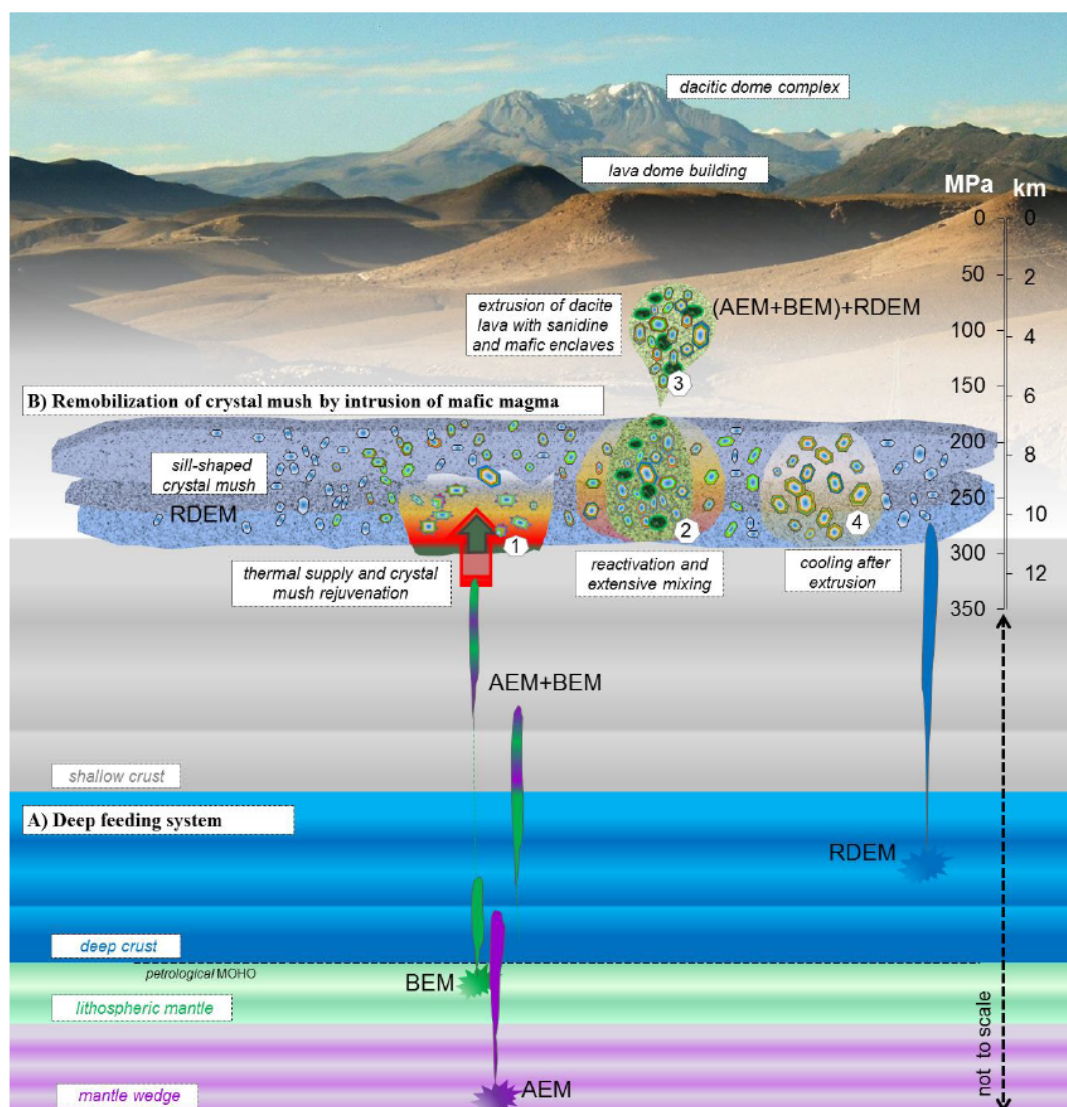
FIGURE 6.14: **Cartoon of the Taapaca plumbing system taken from Banaszak (2014). A** shows a deep feeding system. **B** is a shallow stagnation level of the rhyodacitic crustal magmas in form of sillcomplexes and stages of the remobilization of the rhyodacite crystal mush

6.6 A final discussion on magma chambers

The modeling of volcanoes and their actual geological components is in general a problem in magnetotelluric surveys. The steep topography of stratovolcanoes influences the transfer functions at higher frequencies and make inversion models rather difficult. It was a general problem in previous studies, such as Brändlein (2009) who could not confirm the magma chambers assumed by other geological approaches. A result of his approach with forward modeling and early algorithms had no success. Only recently, new alghorithms became available which may be used for 3-D inversion at an acceptable computational cost.

The AMT study of this thesis confirmed a magmatic structure, respectively one for each volcano. The Taapaca Volcano Complex showed a conductive layer, that is assumed to be the magma chamber, in a depth of five to seven km below the peak. It was located more southward and its existence by location got discussed in personal communication with Wörner. The assumption, that volcanoes such as Taapaca have a trending side for their magma chambers based on their torispherical structure made this finding reasonable. Sensitivity studies confirmed the recurring character of the magma chamber, so the inversion result seems to be correct. Geochemical researches of the working group estimated a depth between five to eleven km. Earlier forward models of Brändlein (2009) had the magma chamber set in a wrong depth so there was no chance to find such a conductive layer in the underground by forward calculation.

The inversion approach on volcano Parinacota achieved a similar result as for Taapaca. However the depth of the conductive feature (supposed to be the magma chamber) did appear in a depth of eight to ten km. A positive recurring sensitivity study confirmed the existence of the feature. Compared to the geochemical approach of the working group the result is consistent. The MT results concerning depth of the magmatic reservoir is consistent with geochemical investigations.

Appendix A

Appendix A
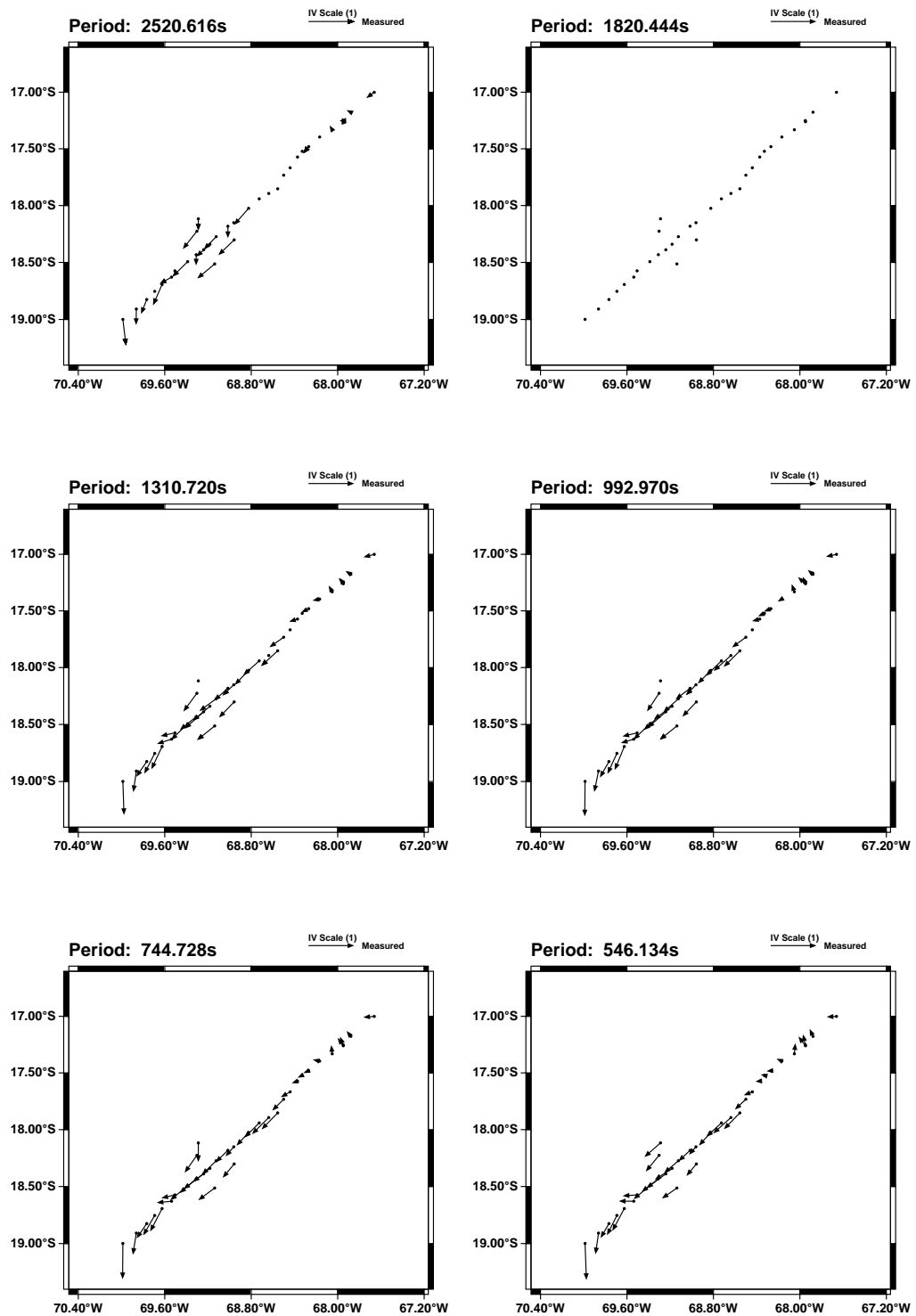
FIGURE A.1: **Induction Vectors after Wiese extracted from Grid3D** No data for period 1820s
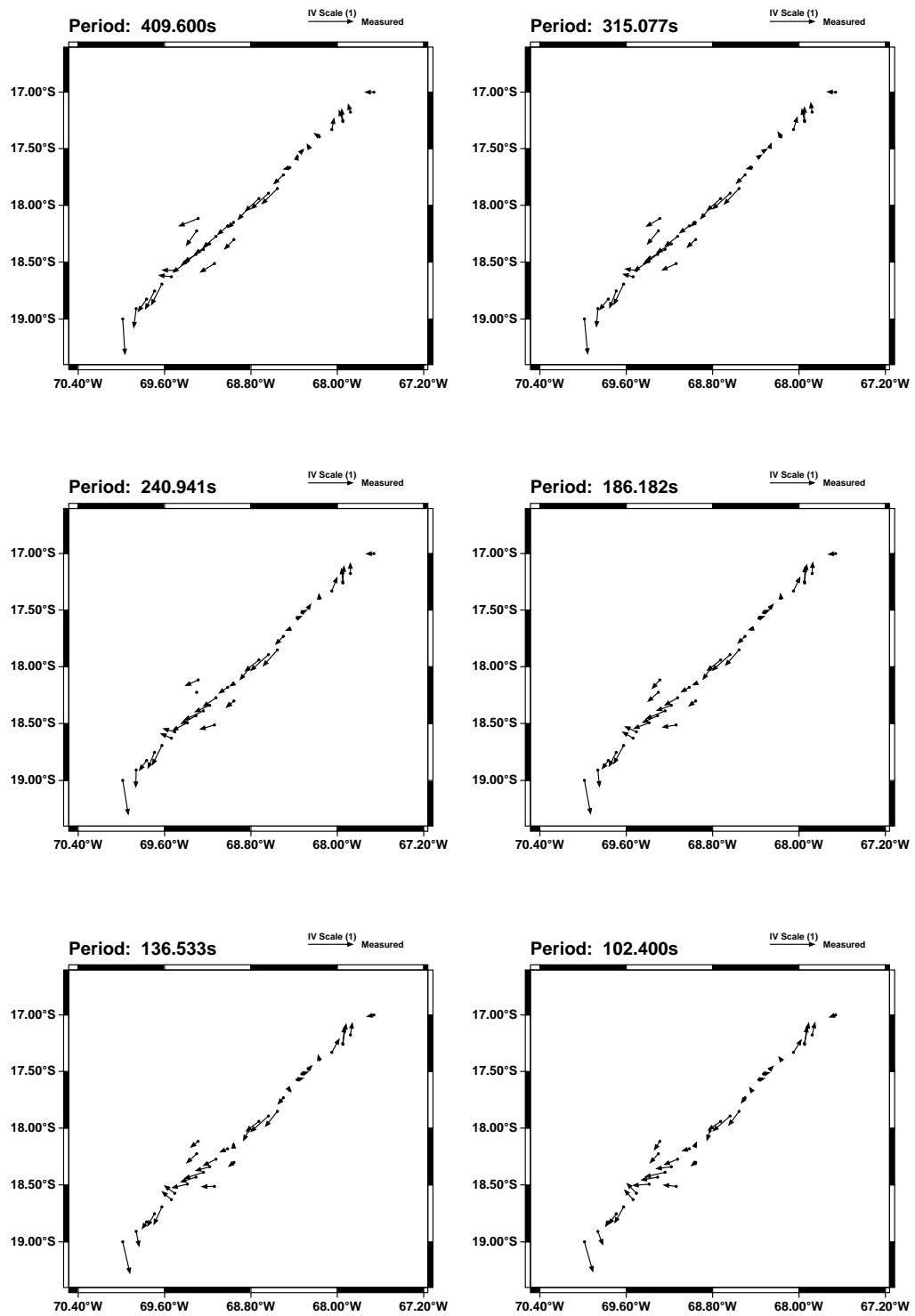
FIGURE A.2: **Induction Vectors after Wiese extracted from Grid3D** No data
for period 1820s
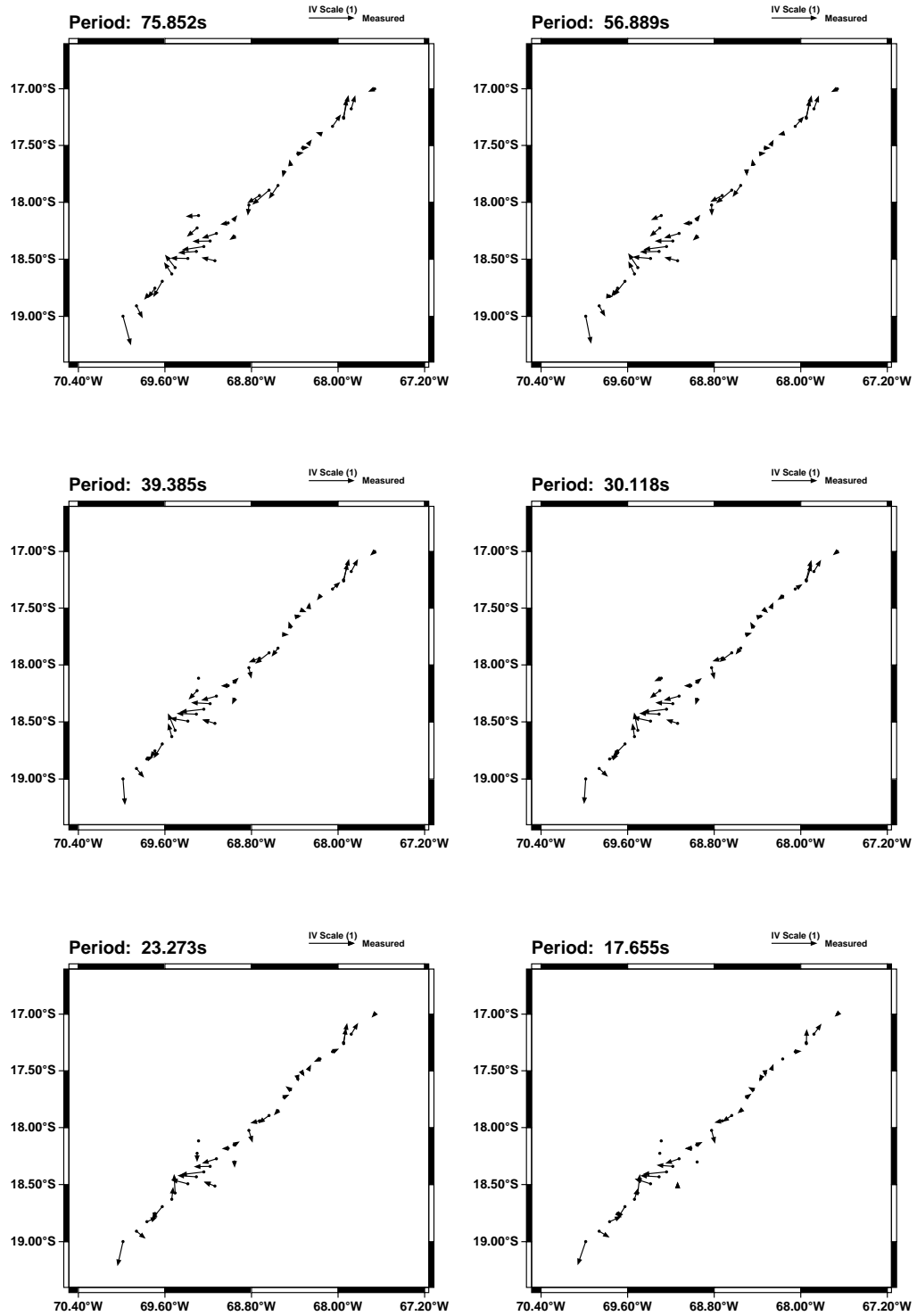
FIGURE A.3: **Induction Vectors after Wiese extracted from Grid3D** No data
for period 1820s
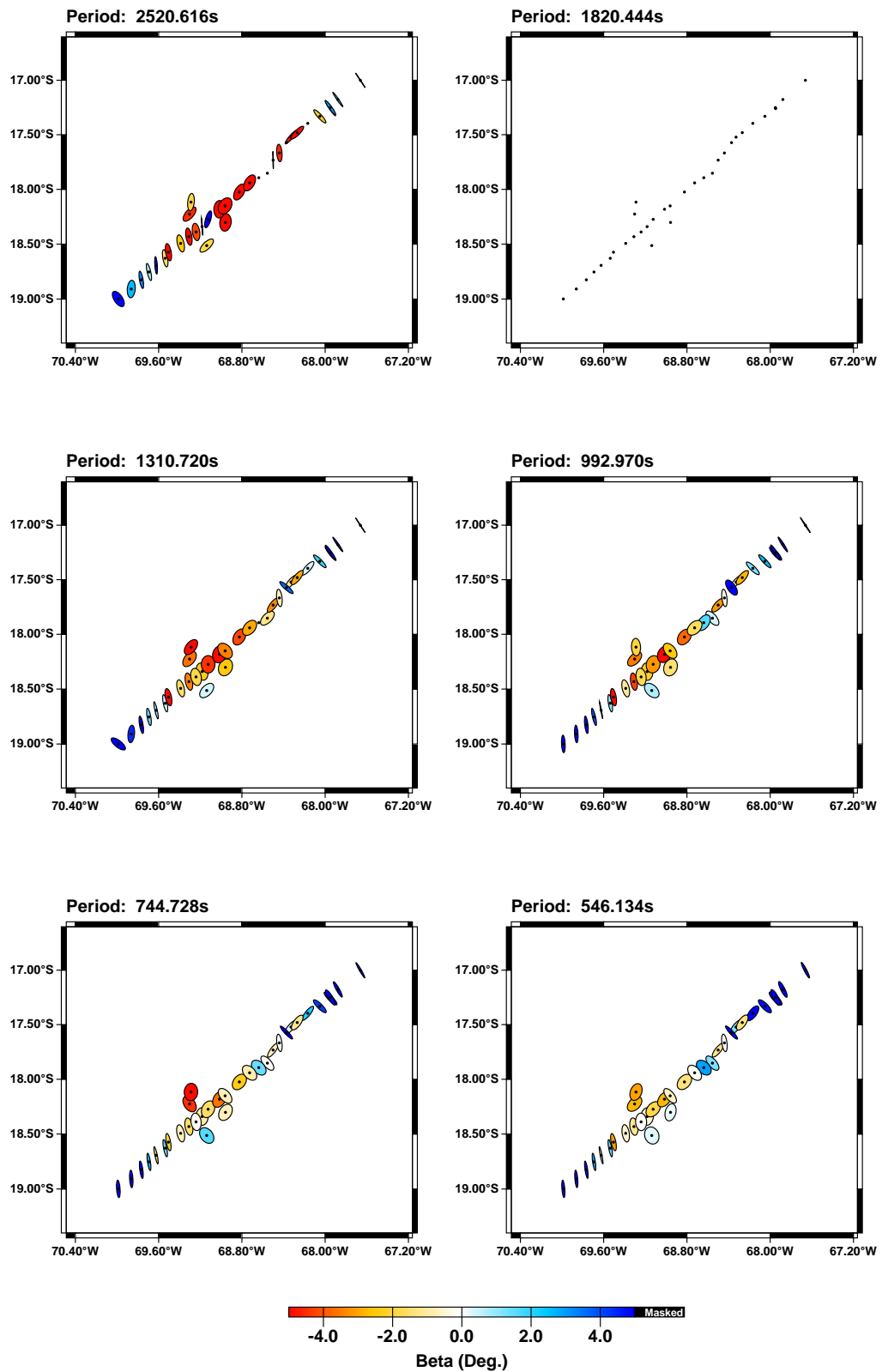
FIGURE A.4: **Phase tensor ellipses with information for the period range 10s - 10,000s** No data for period 1820s
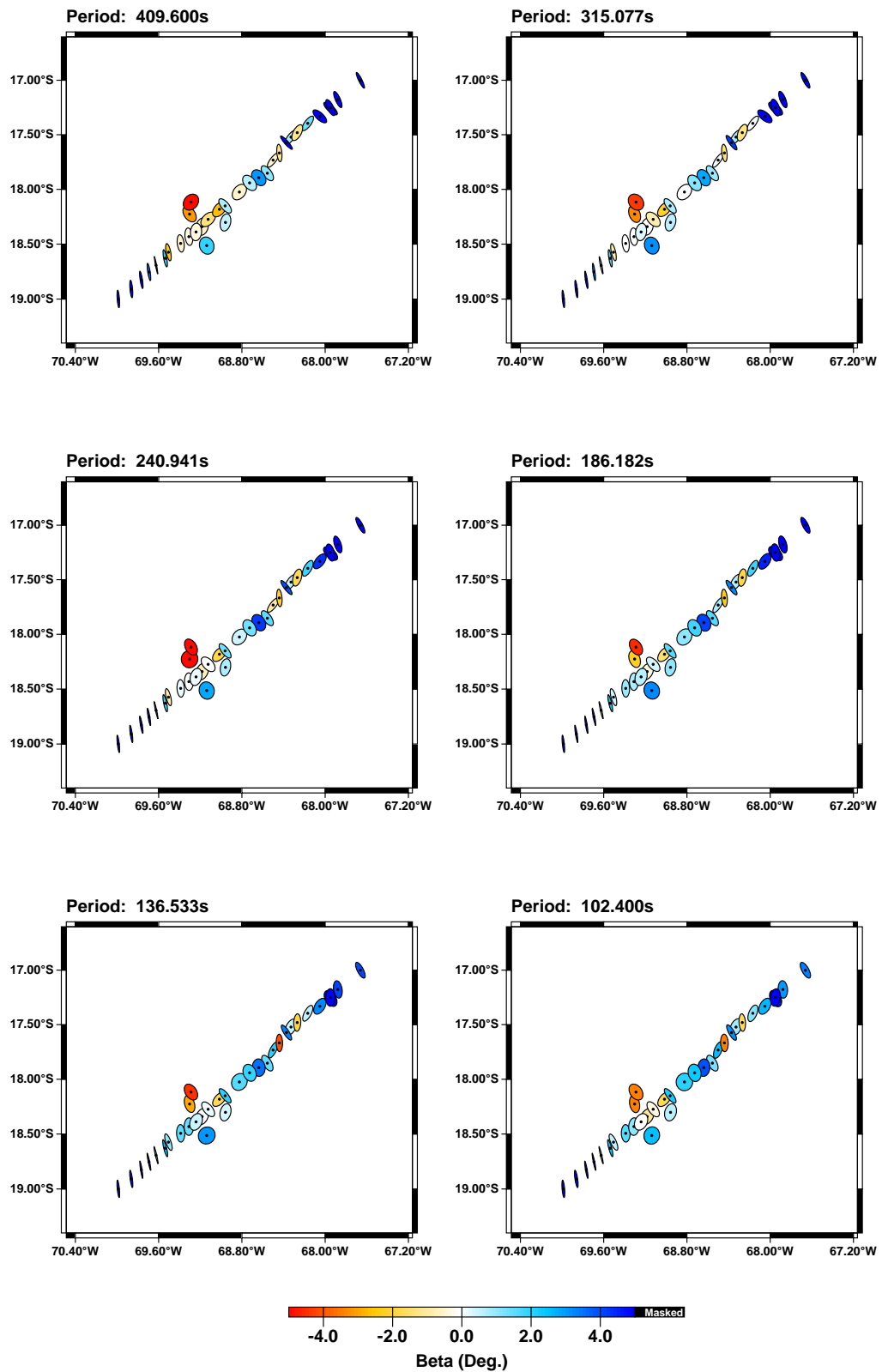
FIGURE A.5: **Phase tensor ellipses with information for the period range 10s – 10,000s** No data for period 1820s
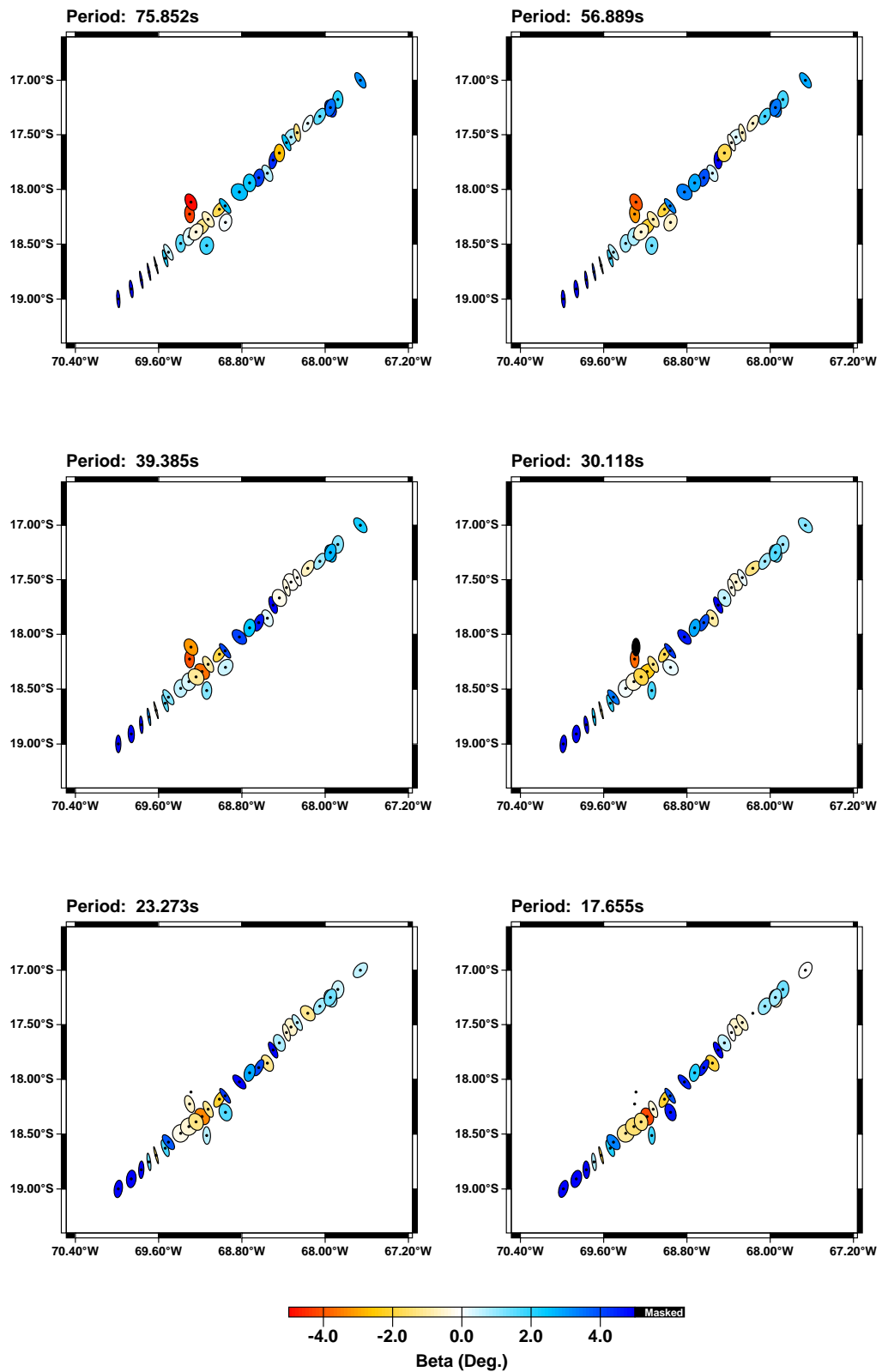
FIGURE A.6: **Phase tensor ellipses with information for the period range 10s - 10,000s** No data for period 1820s
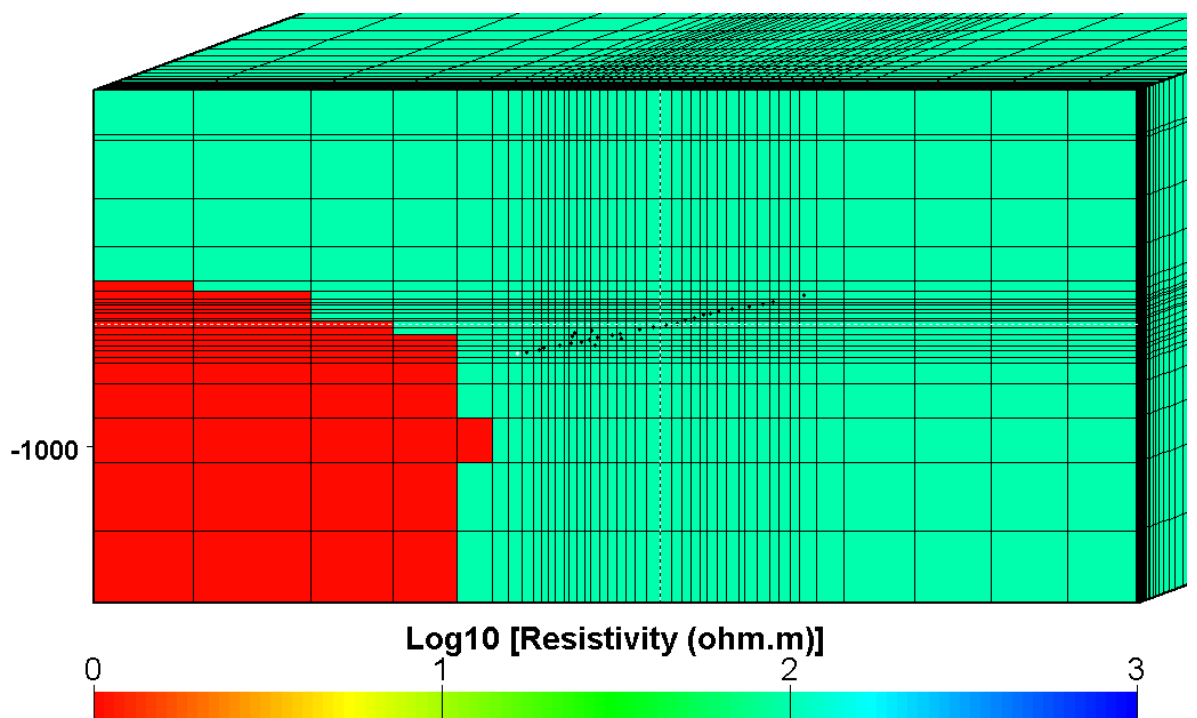
FIGURE A.7: **Cells around a study area with Pacific Ocean in the West** This is a top view of the transect.
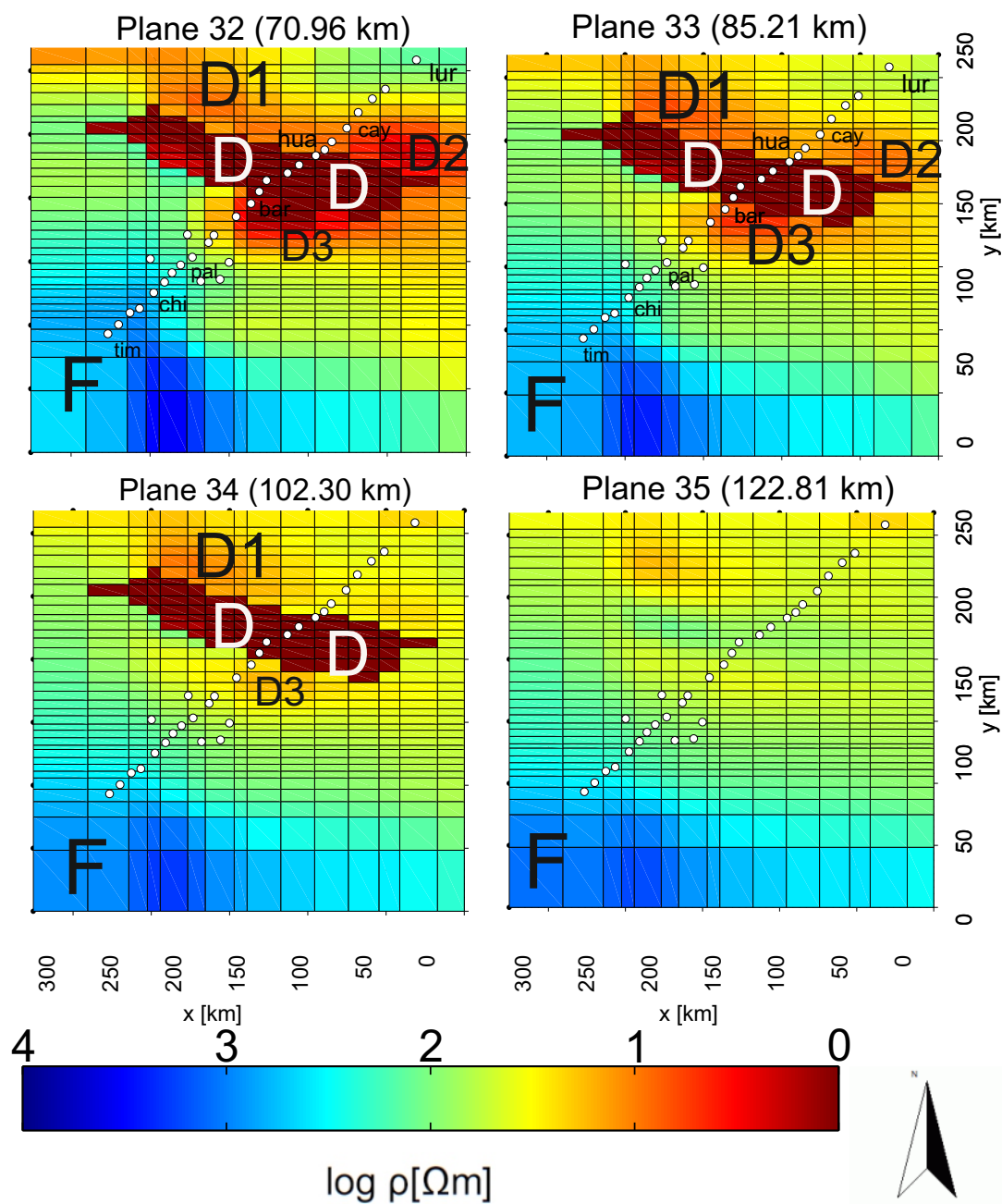
FIGURE A.8: **Plan view of the inverse model after 200 iterations with a conductive feature in a depth range of 70 km - 120 km** RMS= 2.54 with a background resistivity for the homogeneous half-space of 100 Ωm and the sea water 0.3 Ωm. The conductive complex was given a resistivity of 1 Ωm.
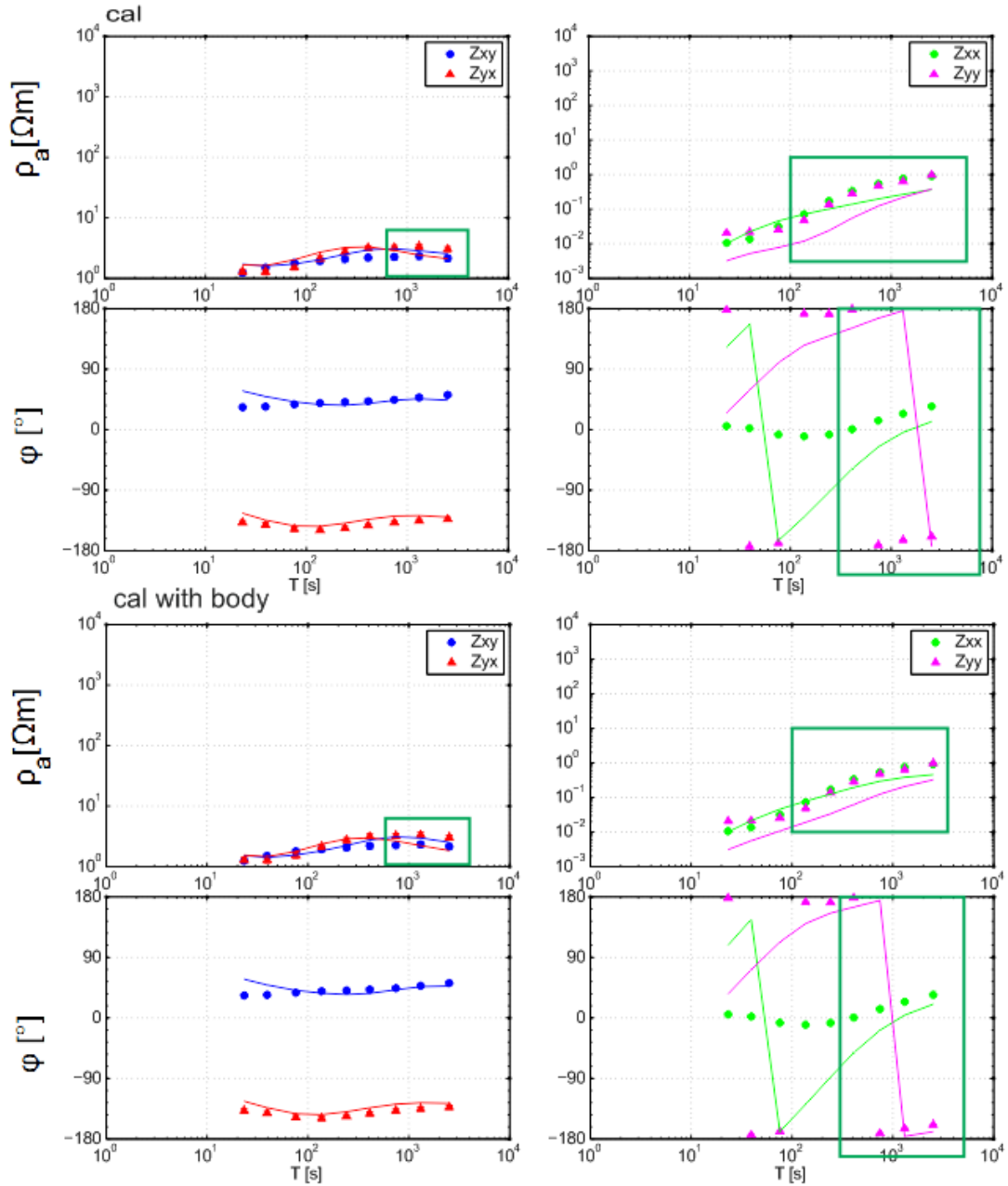
FIGURE A.9: **Comparison of apparent resistivity and phase curves for off-diagonal(red/blue) and main-diagonal(pink/green)** Site CAL without and with a conductive feature beneath the Altiplano in 70 km depth ranging 120 km into the mantle wedge.

Appendix B

Appendix B
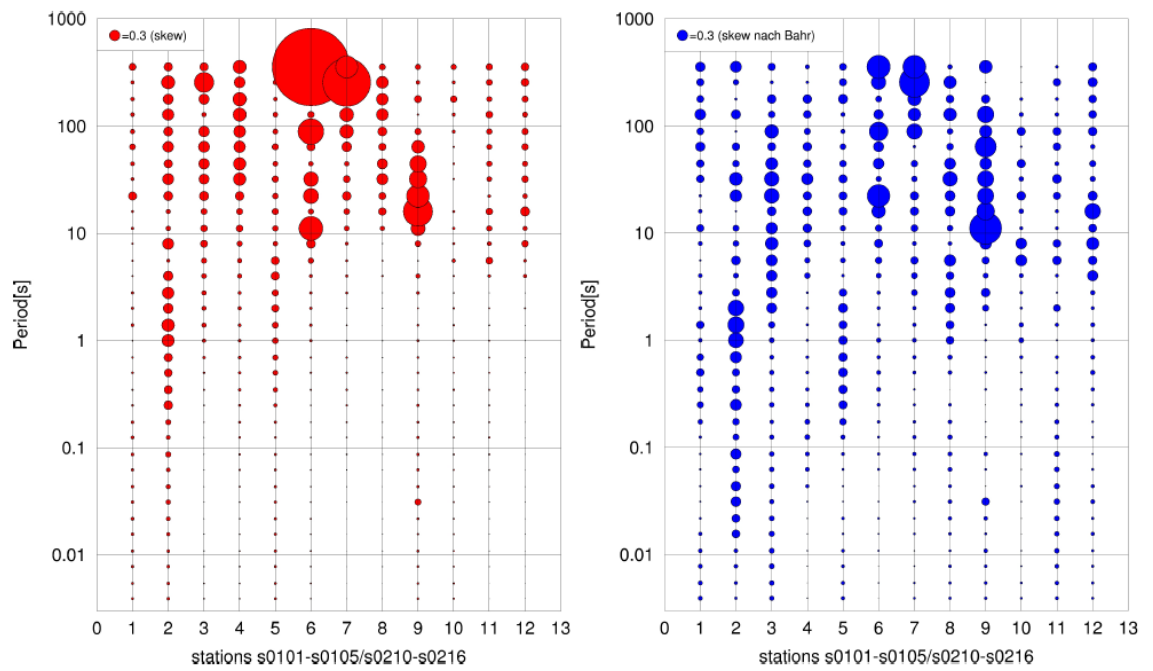
FIGURE B.1: **Skew after Swift (red circles) and Bahr (blue ones)** Diameter of the circle indicates the term of the Skew depending on its frequency and station. Station 1-5 are for Taapaca, Station 6-12 for Parinacota.
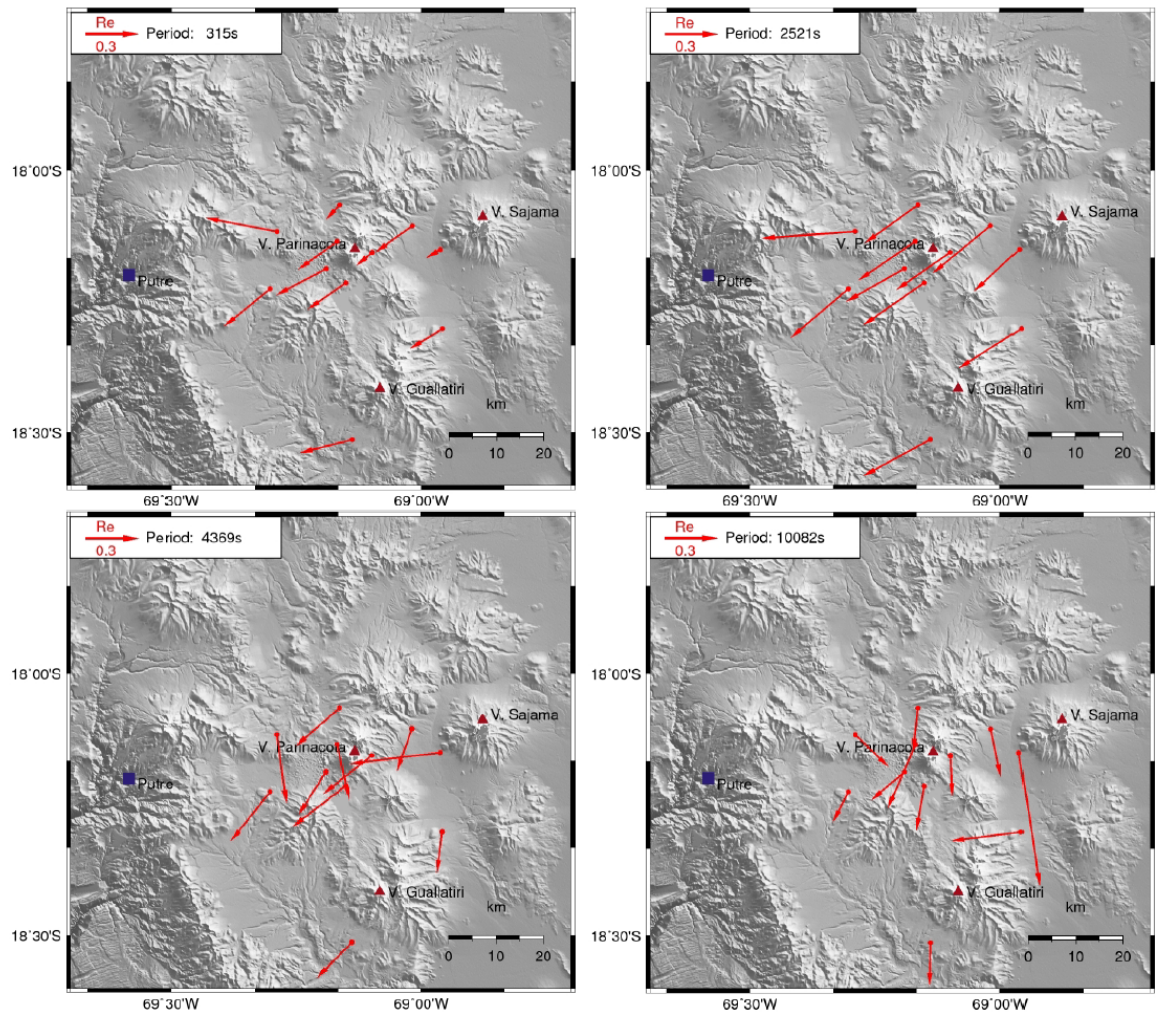
FIGURE B.2: **Induction vectors around the stratovolcanoes Taapaca and Parinacota for LMT sites** Period ranges from top left: 315s, 2521s, 4369s, 10082s. Induction vectors (Wiese, 1962) are pointing parallel into W-S-W direction.
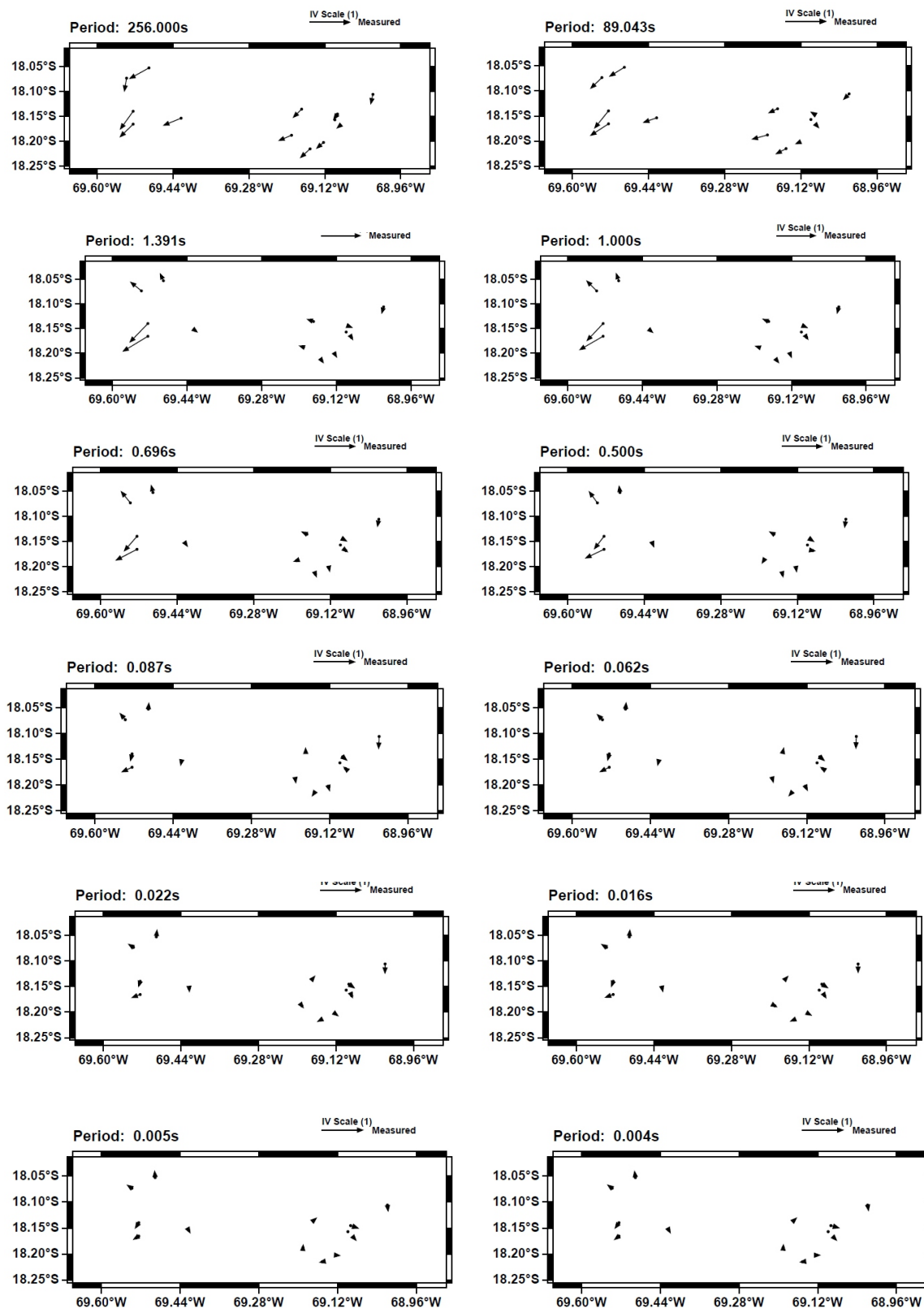
FIGURE B.3: **Induction vectors around the stratovolcanoes Taapaca and Parinacota for AMT sites** Created with Grid3D for exemplary sites that show same behavior as Brändlein's did.
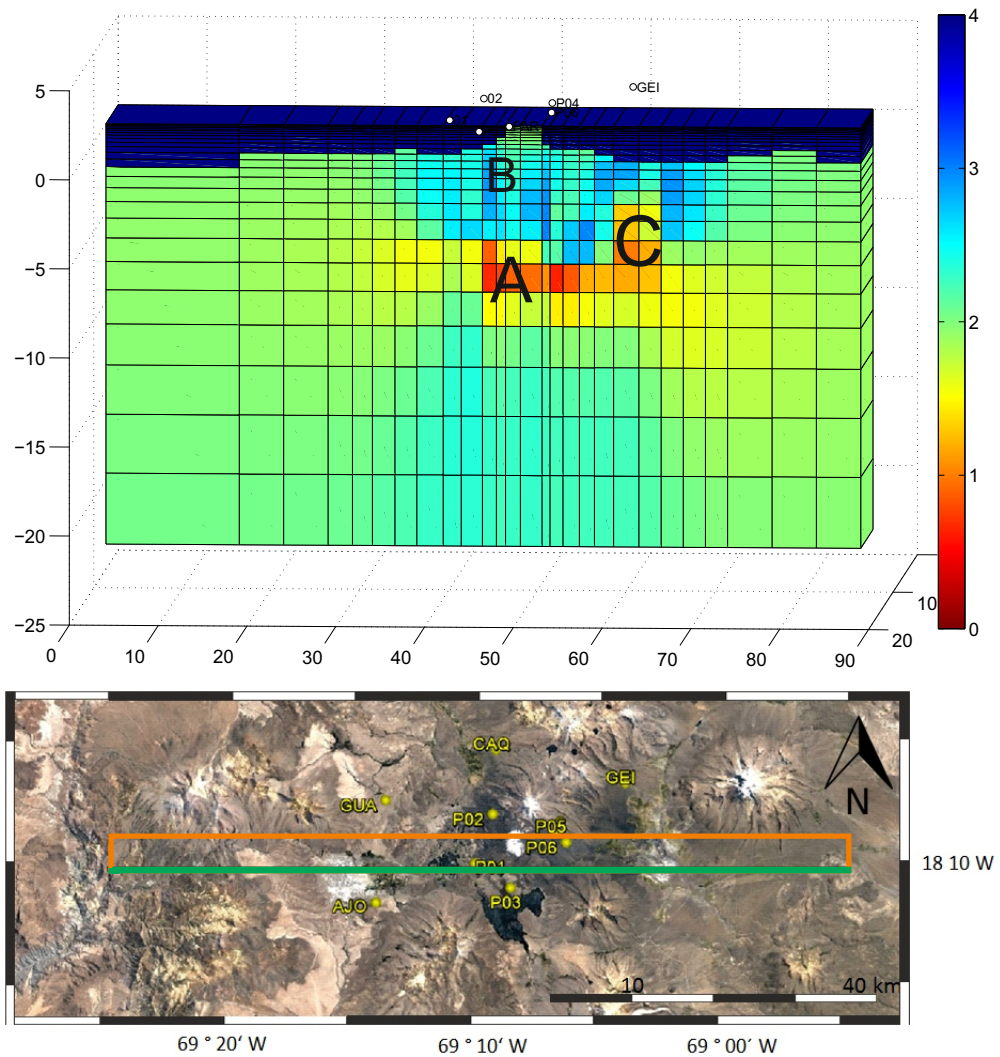
FIGURE B.4: **Cross section of the profile at** $18°\ 10'S$ **of mountain Parinacota.**
Well conductive feature (A) with an apparent resistivity of 1 Ωm beneath volcano Pari-
nacota. There is another well conductive feature (C) eastward of Parinacota. Higher
resistivity structure (B) in the subsurface around the volcano complex. The green line
shows the point of view from the profile.
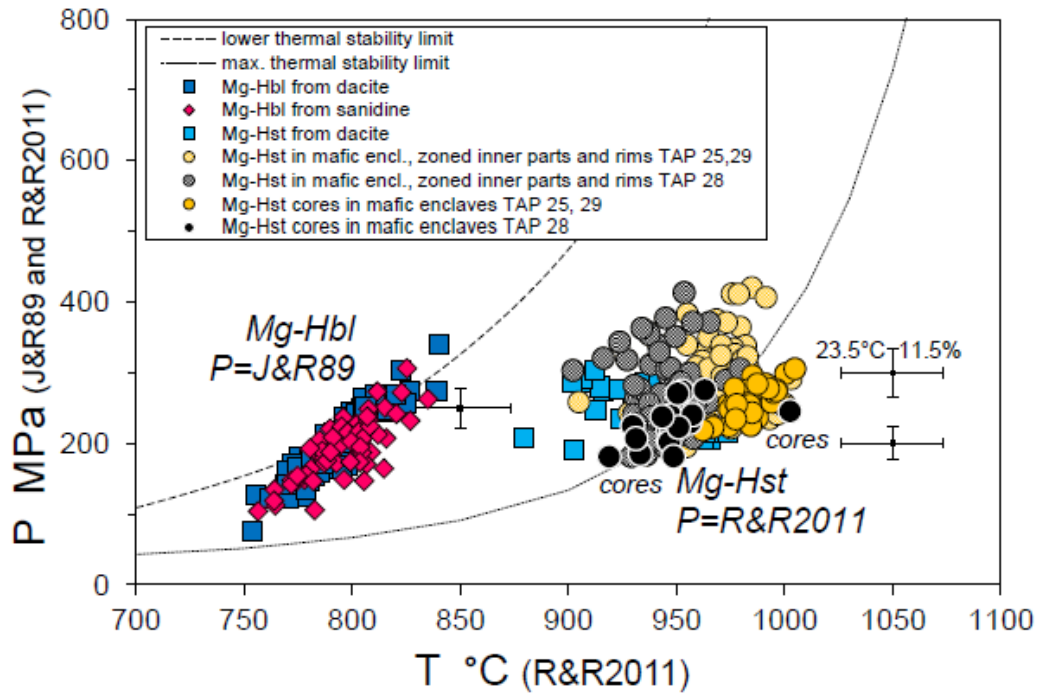
FIGURE B.5: **P-T crystallization conditions of Taapaca amphiboles.** Pressure values of low-Al-Ti Mg-Hbl are calculated using Al^{TOT}-in Hbl formulation of Johnson & Rutherford (1989) due to the best consistency of calibration conditions with Taapaca natural Mg-Hbl. Pressure values of high-Al-Ti Mg-Hst are obtained from an Equation presented by Ridolfi & Renzulli (2011) due to the best fit of experimental Mg-Hst. Crystallization temperatures of both amphibole populations presented in this diagram results from R&R2011 calculated with appropriate pressures used in the T-formula. Dashed lines show lower and maximal stability limits of amphibole defined by Ridolfi et al. (2010). The error bars represent values for model uncertainties specified by R&R2011. Image taken from Banaszak (2014).

Bibliography

Allmendinger, R. W., Jordan, T. E., Kay, S. M. and Isacks, B. L.(1997). The evolution of the Altiplano-Puna Plateau of the Central Andes. Annual Review of Earth and Planetary Sciences, 25, 139–174.

Allmendinger, R., W., Gonzalez, G., Yu J., Hoke, G., Isacks B. (2005): Trench-parallel shortening in the Northern Chilean Forearc: Tectonic and climatic implications GSA Bulletin 117, 1-2, 89- 104, doi : 10:1130=B25505:1.

Aster, R., C., Borchers, B., Thurber, C., H. (2005): Parameter Estimation and Inverse Problems, Int. Geophys. Ser., 90. Elsevier Academic Press.

Banaszak M.; (now Blum-Oeste M.), (2014):Differentiation regimes in the Central Andean magma systems: case studies of Taapaca and Parinacota volcanoes, Northern Chile, PhD thesis, Georg-August University School of Science (GAUSS)

Bahlburg H., Breitkreuz Ch. , Giese P. (1988): The Southern Central Andes, Contributions of Structure and Evolution of an Active Continental Margin, Berlin Heidelberg New York London Paris Toyko Springer

Bahr, K. 1988. Interpretation of the magnetotelluric impedance tensor: regional induction and local telluric distorsion. Journal of Geophysics, 62, 119–127.

Baumjohann W. and Nakamura R. (2007): Magnetospheric Contributions to the Terrestrial Magnetic Field, Volume 5 Treatise on Geophysics, Geomagnetism

Berdichevsky, M. N., Dmitriev, I. V., (2008): Models and Methods of Magnetotellurics, Berlin: Springer

Booker, J. R., Narod, B., (2002): Extracting Dead Band Magnetotelluric Responses From Long Period Array Data. 2002AGUFMGP51A0989B American Geophysical Union, Fall Meeting 2002, abstract GP51A-0989

Booker, J., (2013): The magnetotelluric phase tensor: a critical review, Surv. Geophys., 35(1), 7–40.

Adrian A. Borsa, Helen A. Fricker, Bruce G. Bills, Jean-Bernard Minster, Claudia C. Carabajal and Katherine J. Quinn: Topography of the salar de Uyuni, Bolivia from kinematic GPS: Geophys. J. Int. 172 (1): 31-40. doi: 10.1111/j.1365-246X.2007.03604.x

Brasse, H., Y. Li, G. Kapinos, D. Eydam, and L. Mütschard (2006), Uniform deflection of induction vectors at the South Chilean Continental Margin: A hint at electrical anisotropy in the crust, in Kolloquium Elektromagnetische Tiefenforschung, edited by O. Ritter and H. Brasse, pp. 281– 287, Haus Wohldenberg, Holle, Germany

H. Brasse, D. Eydam (2008): Electrical conductivity beneath the Bolivian Orocline and its relation to subduction processes at the South American continental margin, JOURNAL OF GEOPHYSICAL RESEARCH, VOL. 113, B07109, doi:10.1029/2007JB005142, 2008

Brasse H., (2011): Electromagnetic Methods in the Geophysics, Version 2011, Inst. für Geologische Wissenschaften, Freie Universität Berlin, 212.

Brändlein, 2009: Studien zur Auflösbarkeit von Magmenkammern unter Stratovulkanen am Beispiel von Parinacota und Taapaca, diploma thesis Chile/Bolivien.

Caldwell, T. G., Bibby, H. M. and Brown, C. (2004): The magnetotelluric phase tensor. Geophys. J. Int., 158: 457–469.

Cahill, T., & Isacks, B.L. (1992): Seismicity and shape of the subducted Nazca Plate. Journal of Geophysical Research, 97, 17503–17529.

Cantwell, T. and Madden, T., R. (1960): Preliminary report on crustal magnetotelluric measurements. Journal of Geophysical Research, 65(12), 4202-4205.

Clark, A.H., Farrar, E., Kontak, D.J., Langridge, R.J., Arenas, M.J., France, L.J., McBride, S.L., Wasteneys, H.A., Sandeman, H.A., and Archibald, D.A., 1990 - Geologic and geochronologic constraints on the metallogenic evolution of the Andes of southwestern Peru: Economic Geology, V 85, p 1520-1583.

Clavero J E, Sparks R S J, Pringle M S, Polanco E, Gardeweg M C, 2004. Evolution and volcanic hazards of Taapaca Volcanic Complex, Central Andes of Northern Chile. J Geol Soc London, 161: 603-618. http://dx.doi.org/10.1144/0016-764902-065

Constable, C.G. and S.C. Constable, (2004=: Satellite magnetic field measurements: Applications in studying the deep Earth. In "The State of the Planet: Frontiers and Challenges in Geophysics, Geophys. Mono. 150", ed. R.S.J. Sparks and C.T. Hawkesworth, Am. Geophys. Un., pp. 147–159.

Constable, C., S. (2007): Geomagnetism, Treatise on Geophysics, Geomagnetism, 5

Damm, K.-W. & Pichowiak, S. (1986): Geochemie, Petrologie und Geochronologie der Plutonite und des metamorphen Grundgebirges in Nordchile.- Berliner geowissenschaftliche Abhandlungen., (A) 66, I, 73-146, Berlin

Dorbath, C., & Granet, M. 1996. Local earthquake tomography of the Altiplano and the Eastern Cordillera of northern Bolivia. Tectonophysics, 259, 117–136.

Dunn, J.F., Hartshorn, K.G., and Hartshorn, P.W. (1995): Structural styles and hydrocarbon potential of the Subandean thrust belt of Southern Bolivia. In: Tankhard, A.J., Suárez-Soruco, R., and Welsink, H.J. (Editor), Petroleum basins of South America. American Association of Petroleum Geologists Memoir, v. 62, p. 523-543.

Egbert, G. D. (1997), Robust multiple-station magnetotelluric data processing, Geophys. J. Int., 130, 475– 496.

Egbert, G. D., Kelbert, A., 2012: Computational recipes for electromagnetic inverse problems. Geophysical Journal International 189 (1), 251-267

Engdahl, E. R., and A. Villasen~or (2002), Global seismicity: 1900– 1999, in Int. Handbook of Earthquake and Engineering Seismology, Part A, edited by W. H. K. Lee et al., pp. 665–690, Academic Press, San Diego, Calif.

Eydam, D. (2008), Magnetotellurisches Abbild von Fluid- und Schmelzprozessen in Kruste und Mantel der zentralen Anden, diploma thesis, Fachrichtung Geophys., Freie Univ. Berlin, Berlin.

Francis, P.W., & Wells G.L., 1988 Landsat Thematic Mapper Observations of débris avalanche deposits in the Central Andes. Bull Volcanol. 50:258-278.

Franke A., S. Kütter, R.-U. Börner, and K. Spitzer. Numerical simulation of magnetotelluric fields at Stromboli. In Proceedings 4th International Symposium on Three-Dimensional Electromagnetics, Freiberg, 27. - 30.9.2007, pages 138 - 141, 2007.

Anisotropic Modelling of Magnetotelluric Data in North Chile (2010), bachelor thesis, Fachrichtung Geophys., Freie Univ. Berlin, Berlin.

Giese, P.; Scheuber, E.; Schilling, F.; Schmitz, M.; Wigger, P. (1999). Crustal thickening processes in the Central Andes and the different natures of the Moho-discontinuity. Journal of South American Earth Sciences, Volume 12, Issue 2, p. 201-220.

Gutscher, M.-A., Spakman, W., Bijwaard, H., & Engdahl, E. R. (2000). Geodynamics of flat subduction: Seismicity and tomographic constraints from the Andean margin. Tectonics, 19 (5), 814–833.

Gephart, J. W. (1994). Topography and subduction geometry in the Central Andes: Clues to the mechanics of a non-collisional orogen. Journal of Geophysical Research, 99 (B6), doi:10.1029/94JB00129.

Hammerschmidt, K., R. Dobel, and H. Friedrichsen (1992), Implication of Ar-40/Ar-39 Dating of Early Tertiary Volcanic-Rocks from the North-Chilean Precordillera, Tectonophysics, 202, 55-81.

Heise W., T. G. Caldwell, H. M. Bibby, and S. C. Bannister. Three-dimensional modelling of magnetotelluric data from the Rotokawa geothermal Field, Taupo Volcanic Zone, New Zealand. Geophys. J. Int., doi:10.1111/j.1365-246X.2008.03737.x, 2008.

Isacks, B. L.(1988). Uplift of the Central Andean plateau and bending of the Bolivian Orocline. Journal of Geophysical Research, 93(B4), 3,211–3,231.

James, D.E., & Sacks, I.S. (1999). Cenozoic formation of the Central Andes: A geophysical perspective. Society of Economic Geology, Special Publication, 7, 1–26.

Johnson, M. C. & Rutherford, M. J. (1989). Experimental calibration of the aluminum-in-hornblende geobarometer with application to Long Valley caldera (California). Geology 17, 837-841.

Kennan, L., Lamb, S.H., Rundle, C., 1995. K–Ar dates from the Altiplano and Cordillera Oriental of Bolivia: implications for Cenozoic stratigraphy and tectonics. J. S. Am. Earth Sci. 8, 163 – 186

Kelbert, A., Meqbel, N., Egbert, G.D., Tandon, K., (2014): ModEM: a modular system for inversion of electromagnetic geophysical data Computers & Geosciences 66, 40-53

Kley, J. (1996): Transition from basement-involved to thin-skinned thrusting in the Cordillera Oriental of southern Bolivia. Tectonics, v. 15, n. 4, p. 763-775.

Klotz, J., Abolghasem, A., Khazaradze, G., Heinze, B., Viektor, T., Hackney, R., Bataille, K., Maturana, R., Viramonte, J. and Perdomo, R. (2006)?, Long-Term Signals in the Present-Day Deformation Field of the Central and Southern Andes and Constraints on the Viscosity of the Earths Upper Mantle. In: O. Oncken et al. (Editors), The Andes: Active Subduction Orogeny Frontiers in Earth Sciences, Springer, Berlin, 65 - 89.

Klovan, J. E. & Imbrie, J. (1971). An algorithm and FORTRAN-IV program for large-scale Q-mode factor analysis and calculation of factor scores. Journal of the International Association for Mathematical Geology 3, 61-77.

R.L. Mackie, J.T. Smith, and T. Madden. Three-dimensional electromagnetic modeling using Inite difference equations: The magnetotelluric example. Radio Science, 29: 923-936, 1994.

Moores E.; Twiss R.J. 1995.Tectonics W.H. Freeman and Co., ISBN 0-7167-2437-5

Müller, R.D., Roest, W.R., Royer, J.-Y., Gahagan, L.M., & Sclater, J.G. (1997) Digital isochrons of the world's ocean floor. Journal of Geophysical Research, 102 (B2), 3211–3214.

Müller A. and Haak V. (2004): 3-D modeling of the deep electrical conductivity of Merapi volcano (Central Java) : integrating magnetotellurics, induction vectors and the effects of steep topography. J. Volc. Geotherm. Res., 138:205-222, 2004.

Parkinson, W. (1959): Directions of rapid geomagnetic variations, Geophysics J.R. Astr. Soc. 2:1-14.

Ridolfi, F. & Renzulli, A. (2011 online). Calcic amphiboles in calc-alkaline and alkaline magmas: thermobarometric and chemometric empirical equations valid up to 1,130C and 2.2 GPa. Contributions to Mineralogy and Petrology 163, 877-895.

Ritter, O. (2016): Angewandte Elektromagnetik, lecture notes, Version 2016, Ins. für Geologische Wissenschaften, Freie Universität 212

Ritz, M., Bondoux, F., Hérail, G. and Sempere, T. (1991): A magnetotelluric survey in the northern Bolivian Altiplano, Geophys. Res. Lett., 18, 475-478.

Rodi, W., and R. L. Mackie (2001), Nonlinear conjugate gradients algorithm for 2-D magnetotelluric inversions, Geophysics, 66, 174– 187.

Ward, Ryan Porter, Susan L. Beck, George Zandt, Lara Wagner, Estela Minaya, and Hernando Tavera (2011): Preliminary Results From the CAUGHT Experiment: Investigation of the North Central Andes Subsurface Using Receiver Functions and Ambient Noise Tomography; Jamie Ryan, Kevin M., AGU Fall Meeting

Sandeman, H.A., Clark, A.H., Farrar, E., (1995). An integrated tectono-magmatic model for the evolution of the southern Peruvian Andes (13–208 S) since 55 Ma. Int. Geol. Rev. 37, 1039 – 1073.

Sempere, T., G. Hérail, J. Oller, and M. G. Bonhomme (1990), Late Oligocene – early Miocene major tectonic crisis and related basins in Bolivia, Geology, 18, 946–949.

Scheuber, E., Bogdanic, T., Jensen, A. and Reutter, K.-J.(1994). Tectonic development of the North Chilean Andes in relation to plate convergence and magmatism since the Jurassic. K.-J. Reutter, E. Scheuber, and P. J. Wigger, Tectonics of the Southern Central Andes, 121 – 139. Springer Verlag, Berlin, Heidelberg, New York.

Schmucker, U., Forbush, S.E., Hartmann, O., Giesecke, A.A., Casaverde, M., Castillo, J., Salgueiro, R., del Pozo, S. 1966. Electrical conductivity anomaly under the Andes. Carnegie Inst. Wash. Yearb., 11–28.

Schmucker, U.(1970). Anomalies of geomagnetic variations in the Southwestern United States. Bull. Scripps. Inst. Oceanogr., Univ. of California, 13.

Schmucker, U. (1973): Regional induction studies. Phys. Earth Planet. Inter., 7:365NAK378,

Schön, J., 1997; Physical Properties of Rocks: Fundamentals and Principles of Petrophysics

Tom Simkin, Lee Siebert, Lindsay McClelland, David Bridge, Christopher Newhall, John H Latter (1981): Volcanoes of the world: a regional directory, gazetteer, and chronology of volcanism during the last 10,000 years, US Hutchinson Ross Publishing

Simpson, F. and Bahr, K. (2005): Practical Magnetotellurics, Cambridge University Press, Cambridge.

Snoke, J.A., James, D., 1997. Lithospheric structure of the Chaco and Parana basins of South America from surface-wave inversion. J. Geophys. Res. 102, 2939 – 2952.

Spichak V. (2001): Three-dimensional interpretation of MT data in volcanic environments (computer simulation). Annali di Geophysica, 44:273-286, 2001.

Springer, M. (1997): Interpretation of heat-flow density in the Central Andes, 29th General Assembly of the International Association of Seismology and Physics of the Earth's Interior (IASPEI) (Thessaloniki Greece 1997).

Springer, M., and A. Förster (1998), Heat-flow density across the centralAndean subduction zone, Tectonophysics, 291, 123– 139.

de Silva, S.L., 1989a. The Altiplano-Puna Volcanic Complex of the Central Andes. Geology , v17, p1102-1106.

de Silva S L, Francis P W, 1991. Volcanoes of the Central Andes. Berlin: Springer-Verlag

Swift, C.M (1986) reprint: A magnetotelluric investigation of an electrical conductivity anomaly in the South Western United States. In Magnetotelluric Methods, ed. K. Vozoff. Tulsa: Society of Exploration Geophysicists, pp. 156–166.

Tarantola, A. (1978). Inverse Problem Theory, Elsevier, Amsterdam.

Tikhonov, A. N.; V. Y. Arsenin (1977). Solution of Ill-posed Problems. Washington: Winston Sons

Pb isotopic constraints on reconstructions of eastern North America and western South America (1981): [abs.] New Orleans, Geological Society of America Abstracts with Programs, p. A-398

Weidelt, P., and A.D. Chave, Chapter 4 (2012): The magnetotelluric response function, in Chave, A.D., and A.G. Jones (eds.), The Magnetotelluric Method: Theory and Practice, Cambridge University Press, pp. 122-164, 2012

Zeil W., Südamerika., Stuttgart (1986): Enke, Ferdinand Enke Verlag, Page 65 - 79

Wiese, H. (1962): Geomagnetische Tiefentellurik Teil II: die Streichrichtung der Untergrundstrukturen des elektrischen Widerstandes, erschlossen aus geomagnetischen Variationen. Pure App. Geophys. 52, 83-103.

Wörner, G., Hammerschmidt, K., Henjes-Kunst, F., Lezaun, J., Wilke, H. (2000). Geochronology (40Ar/39Ar, K-Ar and He-exposure ages) of Cenozoic magmatic rocks from Northern Chile (18-22°S): Implications for magmatism and tectonic evolution of the Central Andes. Revista Geologica de Chile, 27, 205–240.

Wörner, G., Harmon, R. S., Davidson, J., Moorbath, S., Turner, D. L., McMillan, N., Nye, C., Lopez-Escobar, L. & Moreno, H. (1988). The Nevados de Payachata volcanic region (18°S/69°W, N. Chile) I. Geological, geochemical, and isotopic observations. Bulletin of Volcanology 50, 287-303.

Vozoff K. (1987): The magnetotelluric method. In: Electromagnetic Methods in Applied Geophysics, 2, Application Parts A and B.M.N Nabighian SEG. 641-711, Tulsa

Yuan, X., Sobolev, S., V., Kind, R., Oncken, O., Bock, G., Asch, G., Schurr, B., Graber, F., Rudloff, A., Hanka, W., Wylegalla, K., Tibi, R., Haberland, C., Rietbrock, A., Giese, P., Wigger, P., Roewer, P., Zandt, G., Beck, S., Wallace, T., Pardo, M., Comte, D. (2000): Subduction and collision processes in the Central Andes constrained by converted seismic phases, Nature, 408:958961.

List of Figures

Erklärung des Autors

Hiermit versichere ich, dass ich die vorliegende Arbeit selbständig und nur unter Verwendung der angegebenen Quellen und Hilfsmittel angefertigt habe.

Unterschrift:

Datum:

Acknowledgments